Coordination Chemistry Reviews 255 (2011) 2622–2652

Contents lists available at ScienceDirect

Coordination Chemistry Reviews

journal homepage: www.elsevier.com/locate/ccr

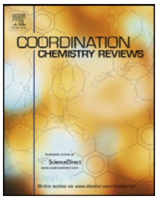

Review

The triplet state of organo-transition metal compounds. Triplet harvesting and singlet harvesting for efficient OLEDs

Hartmut Yersin*, Andreas F. Rausch, Rafał Czerwieniec, Thomas Hofbeck, Tobias Fischer

Institut für Physikalische und Theoretische Chemie, Universität Regensburg, D-93040 Regensburg, Germany

Contents

1. Introduction 2623
2. Triplet harvesting, singlet harvesting, and OLED efficiency 2623
3. HOMO–LUMO excitations and energy states 2626
4. Spin–orbit coupling in organo-transition metal compounds 2627
    4.1. Orbitals and states 2627
    4.2. Direct spin–orbit coupling between MLCT states 2627
    4.3. Indirect spin–orbit coupling to LC states 2628
    4.4. Treatments in realistic systems 2629
    4.5. Spin–orbit coupling and coordination geometry 2630
5. Nonradiative processes 2631
    5.1. Intermolecular quenching 2631
    5.2. Intramolecular quenching 2632
        5.2.1. Thermal population of metal-centered states 2632
        5.2.2. Quenching of the excited state by vibrational coupling to the ground state 2632
6. Emission decay times, radiative rates, and zero-field splitting – A systematic approach 2633
7. Case study Ir(dm-2-piq)$_2$(acac) – Red light emitter 2640
    7.1. Spectroscopic introduction 2640
    7.2. Temperature dependence of the emission 2640
    7.3. Emission decay times of the individual triplet substates and energy level diagram 2641
8. Case study Ir(ppy)$_3$ – Green light emitter 2642
    8.1. Spectroscopic introduction 2642
    8.2. Highly resolved spectra and energy level diagram for the triplet state of Ir(ppy)$_3$ in CH_2Cl_2 2642
    8.3. Broad band emission 2643
    8.4. Emission decay times of the individual triplet substates 2643
    8.5. Studies of Ir(ppy)$_3$ doped into PMMA 2643
    8.6. Radiative and nonradiative decay rates and emission quantum yields of the individual triplet substates 2644
    8.7. Concluding remarks 2645
9. Case study Cu(POP)(pz$_2$BH$_2$) – A blue/white-blue emitter for singlet harvesting 2645
    9.1. Spectroscopic introduction 2646
    9.2. Triplet emission and thermally activated singlet emission 2646
    9.3. Singlet harvesting with Cu(I) complexes 2648
10. Conclusion 2648
Acknowledgements 2649
References 2649

ARTICLE INFO

Article history:
Received 27 November 2010
Accepted 24 January 2011
Available online 31 January 2011

ABSTRACT

Based on a very comprehensive set of experimental data and on theoretical models, an understanding of the triplet state properties of organo-transition metal compounds is worked out. Important trends and guidelines for controlling photophysical properties are revealed. In this respect, we focus on spin–orbit coupling (SOC) and its importance for radiative as well as for nonradiative transitions between the lowest

---

* Corresponding author.
E-mail address: hartmut.yersin@chemie.uni-regensburg.de (H. Yersin).

doi:10.1016/j.ccr.2011.01.042

Keywords:
Singlet harvesting
Triplet harvesting
Triplet emitters
OLED emitters
Spin-orbit coupling
Organo-transition metal compounds
Triplet state
Triplet substates
Radiative decay
Nonradiative decay
Nonradiative decay and spin-orbit coupling
Spin-orbit coupling and geometry
Emission quantum yields

triplet state and the electronic ground state. Moreover, as is discussed on the basis of an extensive data set, summarized for the first time, the efficiency of SOC also depends on the geometry of a complex. The investigations are exemplified and supported by instructive case studies, such as efficient blue and very efficient green and red emitters. Additionally, trends being important for applications of these compounds as emitters in OLEDs are worked out. In particular, the properties of the emitters are discussed with respect to the harvesting of singlet and triplet excitons that are generated in the course of the electroluminescence process. The well-known triplet harvesting effect is compared to the recently discovered singlet harvesting effect. This latter mechanism is illustrated by use of a blue light emitting Cu(I) complex, which represents an efficient fluorescent emitter at ambient temperature. By this mechanism, 100% of the generated singlet and triplet excitons can, at least in principle, be harvested by the emitting singlet state. Potentially, this new mechanism can successfully be applied in future OLED lighting with a distinctly reduced roll-off of the efficiency.

1. Introduction

During the past decade, the scientific interests in understanding the lowest triplet state T_1 of organo-transition metal complexes increased strongly. This was stimulated by the wide range of applications. In particular, these materials are used as emitters in highly efficient OLEDs (organic light-emitting diodes) [1–8] and LEECs (light-emitting electro-chemical cells) [9–12], light absorbers in dye-sensitized solar cells [13–16], chemo- and biosensors [17–21], lumophores for cell imaging [21–24], chemical photo-catalysts [25–28], etc. In spite of all these applications, in which the lowest triplet state is involved, an understanding of its properties is much less common or even less developed than for pure organic materials [29,30]. Thus, it seems to be justified to focus on the triplet states' properties of these metal complexes. Moreover, since the authors' interests are strongly related to material development for OLED applications, the discussion will also focus on demands that are imposed by the use of these materials for efficient light generation in electro-luminescent devices.

In this contribution, we introduce in Section 2 important effects, such as triplet harvesting and singlet harvesting which both, at least in principle, allow for a complete gathering of all excitons formed by electron–hole recombination and their conversion into light. This is in contrast to the situation as found for purely organic emitters, which allow only to use up to 25% of the total number of excitons.

Moreover, in many discussions, electronic transitions are described by excitations from the highest occupied molecular orbitals (HOMOs) to the lowest unoccupied molecular orbitals (LUMOs). These HOMO–LUMO considerations are frequently indicative, since in suitable cases they can provide information on some properties of the lowest excited states. However, the HOMO–LUMO concept does not contain energy states, such as singlets or triplets. Therefore, in Section 3 relations between the two descriptions, i.e. MO model versus state model, will be discussed. In particular, the emission behavior is crucially determined by effects of spin–orbit coupling (SOC) between the lowest triplet state (T_1) and higher lying singlet and triplet states. These effects are difficult to handle quantitatively, but simple guidelines resulting from theoretical considerations can be worked out (Section 4). Additionally, guidelines and assessments based on experiments are given that use the systematics of zero-field splitting (ZFS) of the triplet into substates (Section 6). For example, SOC determines these splittings as well as the radiative decay times of the transitions from the T_1 substates to the singlet ground state. In particular, these decay times should be as short as possible for OLED emitters, but have to be long for many sensor applications. In this respect, the mentioned systematics is highly successful.

For most compounds, apart from only a few exceptions, the phosphorescence quantum yield is significantly lower than 100% and mostly exhibits a distinct temperature dependence. In Section 5, we will present some insight into nonradiative deactivation processes on an introductory level. Interestingly, also these effects depend strongly on SOC. Further, the emission properties of the compounds are controlled not only by purely electronic transitions, but also by the involvement of vibrational modes. These determine the spectral forms, color purities, photoluminescence quantum yields, etc. The corresponding features will be addressed by presenting several case studies (Sections 7–9). We will also present a series of emission data and trends to develop an understanding, in particular, of how to vary photophysical properties by chemical means. Several basic results or characterizations reveal themselves only at cryogenic temperatures. At ambient temperature, at which the materials are usually used, much information is lost simply because of smearing-out effects, such as homogeneous and/or inhomogeneous spectral broadenings. Therefore, low-temperature investigations, application of methods of high-resolution laser spectroscopy, and time-resolved measurements are required for the development of a deeper understanding of the materials' properties. This will be demonstrated by examples and case studies. In particular, the case study focusing on a Cu(I) complex (Section 9) allows us to demonstrate the high potential of the singlet harvesting effect. A short conclusion ends this introductory contribution.

2. Triplet harvesting, singlet harvesting, and OLED efficiency

In an electro-luminescence process, the population of excited states occurs via a recombination of negatively charged electrons and positively charged holes. They attract each other by Coulomb interaction (Fig. 1a) and form excitons in the emission layer of an OLED. Since both, hole and electron, have spins, four different spin combinations are possible. According to quantum mechanics (compare for example [29–31]), *one* combination of antiparallel spins, giving a singlet, and *three* combinations of parallel spins, giving a triplet, occur. (Fig. 1b) Thus, in a statistical limit, 25% of the excitons represent singlets and 75% triplets.

In suitable situations, a single charge carrier is trapped first on the emitter complex, oxidizing or reducing it. For example, for several OLEDs employing Ir(III) complexes, the hole is trapped first [32]. Subsequently, the electron is attracted and the exciton is formed. The processes of population of an excited state of the emitter complex can be described to proceed via singlet (^{1}CT) and triplet (^{3}CT) charge transfer states, as proposed by Yersin [33,34]. These involve the emitter complex and the immediate environment, which usually consists of organic host (matrix) molecules (Fig. 1c). Because of the small SOC constants of the host molecules and the very small energy splitting between the ^{1}CT and ^{3}CT states, it is expected that the intersystem crossing (ISC) time between these two states is significantly longer than relaxation times to lower lying states with the same multiplicity (internal conversion, IC). These latter processes take place in about 10^{-12} s [30]. Therefore,

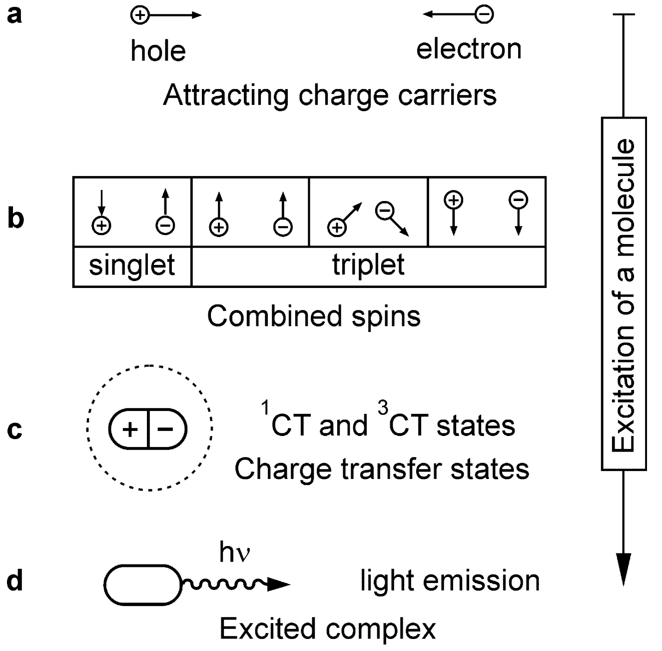

Fig. 1. Schematic description of (a) electron–hole recombination, (b) spin combinations, giving one singlet state and one triplet state. (c) The process of population of the lowest excited states proceeds via singlet and triplet charge transfer (CT) states which involve the emitter and surrounding host molecules. (d) From these CT states relaxations populate the lowest excited states of the emitter [33,34].

fast and separate relaxations without spin flips are expected to populate the lowest excited singlet state S_1 (one path) and the triplet state T_1 (three paths) of the emitter complex, respectively. (Fig. 1d) Subsequently, ISC from the S_1 to the T_1 state can occur.

Based on these model considerations, we can now explain the distinct differences between organic and organo-transition metal emitters for OLED applications. The corresponding processes are schematically displayed in Fig. 2. After the exciton is formed and the relaxations by one singlet and three triplet paths have occurred, the lowest excited singlet and triplet states are populated. This is valid for organic as well as for organo-transition-metal emitter materials. The corresponding processes are schematically displayed in Fig. 2b. The organic molecule can exhibit an efficient and fast decaying singlet emission ($S_1 \rightarrow S_0$) with lifetimes τ of the order of one ns with a fluorescence quantum yield of almost 100% [35–37], if the $S_1 \rightarrow T_1$ intersystem crossing rate is small compared to the fluorescence rate. For organic molecules with $^{1,3}\pi\pi^*$ states, for example, ISC times can be as long as 0.1 to 1 μs [30]. On the other hand, since the probability for the radiative $T_1 \rightarrow S_0$ transition is also very small, the deactivation of the T_1 state occurs normally non-radiatively at ambient temperature. Therefore, 75% of the excitons, namely the triplet excitons, are lost for the emission. Their energy is transferred into heat (Fig. 2a). The conditions are more favorable for organo-transition metal complexes, in which the central metal ion induces significant spin–orbit coupling (Fig. 2c). For these complexes, ISC to the T_1 state is usually very efficient and thus, at an energy separation between the S_1 and T_1 states of several 10^3 cm^{-1}, a singlet S_1 emission is not observable. Moreover, the radiative $T_1 \rightarrow S_0$ rate can become relatively large for compounds with central metal ions with large SOC constants so that efficient phosphorescence with a quantum yield of almost 100% can occur even at ambient temperature [38–40]. (For a more detailed discussion see Section 8.) Consequently, all four possible spin orientations of the excitons can be harvested and populate the lowest T_1 state. By this process of *triplet harvesting* one can, in principle, obtain a four times higher electro-luminescence efficiency with phosphorescent triplet emitters than with fluorescent singlet emitters.

For several compounds, in particular for a number of Ir(III) complexes, the average radiative decay rate k^r_{av} of all three triplet substates is relatively large. For example, for Ir(ppy)$_3$ (chemical structure (**52**), compare Fig. 9) doped into PMMA, a value of $k^r_{av} \approx 6.9 \times 10^5$ s^{-1} ($\tau^r_{av} = 1.4$ μs) has been found at ambient temperature (see also Section 8) [40]. Such high values are well suited for OLED applications by taking advantage of the triplet harvesting effect.

However, many other organo-transition metal compounds exhibit much lower average radiative rates for the $T_1 \rightarrow S_0$ transition. In this situation, the emission decay times are relatively long, if non-radiative processes do not lead to quenching. In this case, saturation and/or triplet–triplet annihilation effects make these materials disadvantageous for OLED applications, as will further be discussed below. Interestingly, a new electro-luminescence mechanism, as recently proposed by Yersin et al. [41–46], can overcome these problems in suitable situations. For these cases specific emitter materials are required. In particular, they should exhibit small energy separations $\Delta E(S_1 - T_1)$ between the lowest excited singlet state S_1 and the triplet state T_1 (small exchange interaction integral) and should show an efficient thermally activated delayed fluorescence, an effect which has already been well known for a long time [30,47–51]. Fig. 2d displays this situation. After exciton formation in an emission layer of an OLED, one singlet path and three triplet paths populate both the S_1 and the T_1 state, respectively, similarly as described above. Again, induced by SOC, the ISC processes downwards from S_1 to T_1 are fast. However, due to the small energy separation $\Delta E(S_1 - T_1)$, also upward processes from T_1 to S_1 are effective at ambient temperature. Thus, emission of both states can occur. As a result, the emission is governed by a Boltzmann distribution according to Eq. (1):

$$\frac{Int(S_1 \rightarrow S_0)}{Int(T_1 \rightarrow S_0)} = \frac{k^r(S_1 \rightarrow S_0)}{k^r(T_1 \rightarrow S_0)} \cdot \exp\left(-\frac{\Delta E(S_1 - T_1)}{k_B T}\right) \qquad (1)$$

Herein $Int(S_1 \rightarrow S_0)$ and $Int(T_1 \rightarrow S_0)$, $k^r(S_1 \rightarrow S_0)$ and $k^r(T_1 \rightarrow S_0)$ represent the fluorescence and phosphorescence intensities and the corresponding radiative rates, respectively. k_B is the Boltzmann constant and T the absolute temperature.

A numerical example may illustrate the advantage of this mechanism. Cu(I) complexes typically exhibit triplet emission decay times $\tau(T_1 \rightarrow S_0)$ of the order of 100 μs up to a few ms [52–54]. An emitter with such a long decay time, e.g. of 1 ms, would not be suited for OLED applications. However, at an energy separation of, for example, $\Delta E(S_1 - T_1) = 500$ cm^{-1} and a ratio of radiative rate constants of $k^r(S_1 \rightarrow S_0)/k^r(T_1 \rightarrow S_0) = 10^4$, the intensity of the $S_1 \rightarrow S_0$ fluorescence at ambient temperature is by a factor of the order of 10^3 stronger than the intensity of the $T_1 \rightarrow S_0$ phosphorescence, according to Eq. (1). Under the same conditions, the measured emission decay time, i.e. the averaged decay time of the two states S_1 and T_1, is reduced from 1 ms to about 1 μs (see Eq. (24)). This decay time is attractively short and is similar to the value as found for Ir(ppy)$_3$.

In conclusion, singlet emitters in OLEDs that take advantage of the *singlet harvesting effect* by gathering both the triplet excitations (induced by three triplet paths) *and* the singlet excitation (effected by one singlet path) *and* by emitting a thermally activated fluorescence, might be similarly well suited for OLED applications as the already well established triplet emitter materials. In Section 9, we will discuss a promising material in some detail.

Obviously, the photophysical properties of the emitter materials are of crucial importance for the OLED performance. Here, we want to discuss some factors that determine the electro-luminescence efficiency. In particular, we want to focus on the impact of the emission decay time. Eq. (2) summarizes the dominating factors that determine the external quantum efficiency η_{ext} of an OLED given in

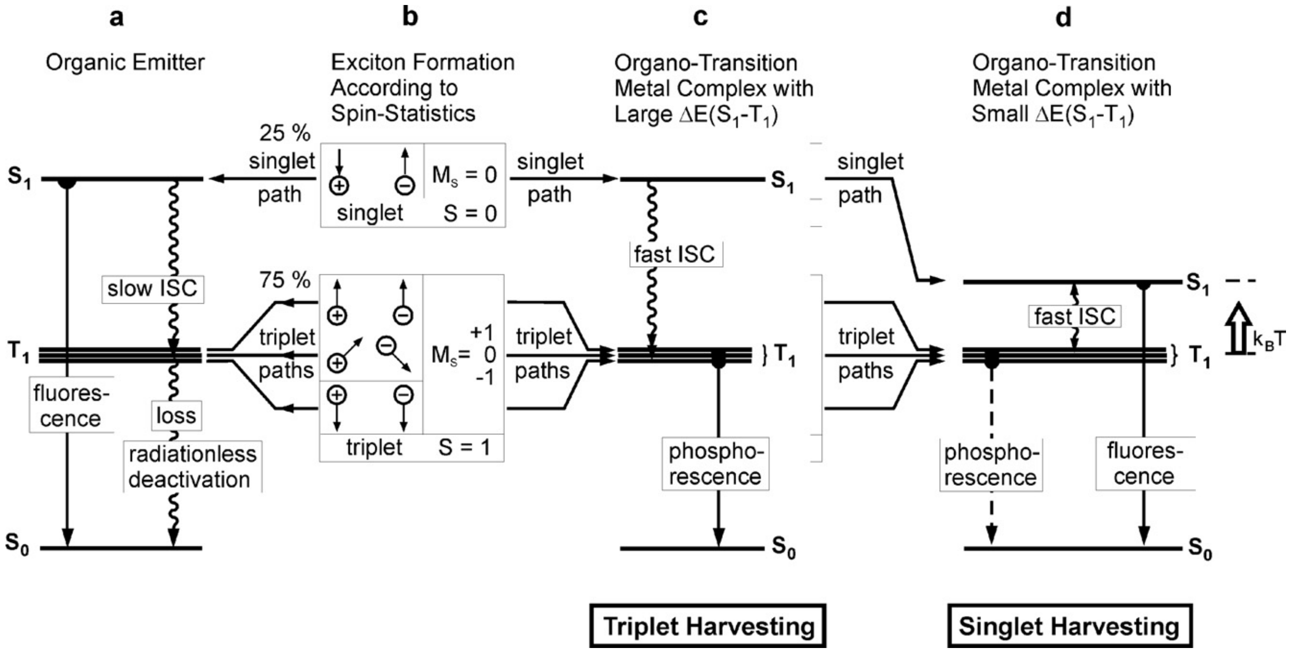

Fig. 2. The diagram displays electro-luminescence excitation processes for organic and organo-transition metal emitters, respectively, and explains the effects of triplet harvesting and singlet harvesting. (b) Due to spin-statistics, electron–hole recombination leads to 25% singlet and 75% triplet state population. (a) In organic molecules, only singlets emit light (fluorescence), while the triplet excitation energy is transferred into heat. (c) Organometallic compounds with transition metal centers show a fast intersystem crossing (ISC) from the singlet state S_1 to the lowest triplet state T_1. Thus, this triplet state *harvests* singlet and triplet excitation energy and can efficiently emit [33,34]. (d) For complexes with small energy separations $\Delta E(S_1 - T_1)$ fast up and down ISC processes can occur, which can lead to an efficient thermally activated fluorescence (compare Section 9). Also in this case, all singlet and triplet excitons are harvested, but the emission represents a short-lived, thermally activated $S_1 \rightarrow S_0$ fluorescence [41–46].

[%] (compare also [55–57]).

$$\eta_{ext} = \chi_{out}\beta\gamma\phi_{PL} \tag{2}$$

The factors involved in Eq. (2) have the following meanings:

- χ_{out} represents the optical outcoupling factor. OLEDs fabricated on simple, planar glass substrates usually loose about 75–80% of the generated light, mainly because of total reflections and waveguiding, surface plasmon losses at the metallic electrodes, etc. These effects prevent the light to leave the OLED device, giving $\chi_{out} \approx 0.2$ [57–61].
- β is a factor that describes the ratio of excitons that lead to a population of luminescent states of the emitter molecule relative to the total number of excitons formed by electron–hole recombination [33,34,62]. For *triplet harvesting* and *singlet harvesting* materials, a value of $\beta = 1$ can be attained, while for purely organic fluorescent emitters, only a value of $\beta = 0.25$ is achievable.
- γ is the charge balance factor [63,64]. It represents the fraction of recombining charge carriers relative to the total number of injected carriers. For OLEDs with well designed layers, a value of almost $\gamma = 1$ can be reached [65]. However, the charge balance can depend strongly on the current density. In particular, for high brightness lighting applications at high current densities, when, among other reasons [66], all emitter complexes are excited and the emission layer is almost saturated, current leakages are crucial and a value of $\gamma \ll 1$ can result [67,68]. Consequently, a long luminescence decay time of the emitter is very disadvantageous, because saturation is obtained at a relatively low brightness and low current density, respectively. Therefore, the use of compounds with short emission decay times is crucial to reduce the roll-off of efficiency with increasing brightness [68,69].
- ϕ_{PL} describes the photo-luminescence quantum yield, which is, under the assumption of fast and quantitative intersystem crossing, given according to Eq. (3)

$$\phi_{PL} = \frac{k^r}{k^r + k^{nr}} = \tau k^r \tag{3}$$

where k^r and k^{nr} are the radiative and nonradiative rate constants and τ is the emission decay time. For OLED applications, ϕ_{PL} should be as high as possible and values higher than at least $\phi_{PL} \approx 40\%$ are targeted. This is not unreasonably high, since, for example, a ϕ_{PL} value of almost 100% is found for Ir(ppy)$_3$ [38–40].

This simple equation already shows that for small k^r values, k^{nr} can easily dominate and this results in a drop of the quantum yield. Consequently, the (radiative) emission decay rate should be as high as possible. For example, the relatively high value of $k^r_{av} \approx 6.9 \times 10^5\ \mathrm{s}^{-1}$, as found for the three triplet substates of Ir(ppy)$_3$ (**52**) (in PMMA at 300 K) [40], is one of the reasons for a successful application of this compound as OLED emitter (see also Section 8).

Obviously, consideration of the nonradiative rate is also crucial for an optimization of an emitter material (compare Section 5). In the scope of the present section, concerning the OLED performance at higher brightness applications, k^{nr} should be replaced by

$$k^{nr} = k^{nr}_{emitter} + k^{nr}(bimol)[j, c] \tag{4}$$

The first term describes the usual nonradiative rate of an emitter in its environment at a specific temperature, while the second term is added to take into account, for example, bimolecular quenching due to triplet–triplet annihilation [67,68,70]. This type of quenching usually becomes more important with increasing current density j [71]. Also other quenching effects should not be ignored, such as exciton–polaron quenching [66,67,72,73]. In most cases, the quenching depends also on the concentration c of the doped emitter complexes. For example, at high concentrations triplet–triplet annihilation and self-quenching [74,75] become more important. Most of these quenching processes have less importance for compounds with short (radiative) emission decay times.

Frequently, the OLED efficiency is measured in different, but related quantities. The luminous efficiency η_{lum} [lm/W] takes into

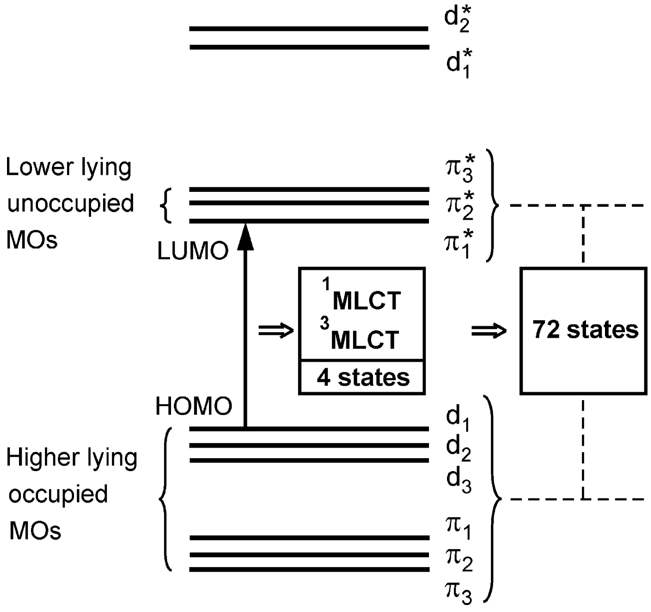

Fig. 3. Schematic diagram of selected molecular orbitals (MOs) for a (pseudo)octahedral complex with low lying MLCT transitions. The HOMO–LUMO excitation leads to four energy states, one ^{1}MLCT and three substates of ^{3}MLCT. Inclusion of the other excitations in the approximate energy range gives already 72 energy states. Here, the three substates of a triplet term are counted as three states.

account the wavelength dependent sensitivity of the human eye (photopic response). Thus, an additional factor $S(\lambda)$ has to be introduced in Eq. (2) [7,56]. The photopic response peaks at a wavelength of 555 nm, reaching a value of $S(555\,\mathrm{nm}) = 683$ lm/W [56]. Another important quantity is the current efficiency η_{curr} [cd/A], which is given by the ratio of the luminous density [cd/m^2] of an OLED to the applied current density [A/m^2] [64]. It is stressed that the performances of OLEDs that emit different colors cannot be compared directly in terms of luminous efficiency or current efficiency, since these parameters depend on the wavelength of the emitted light. For that purpose, the external quantum efficiency, as given by Eq. (2), is better suited.

In summary, the external quantum efficiency η_{ext} without specific improvements of outcoupling can be as high as 20–25% [69,76,77]. Moreover, the above discussions show that emitters with high radiative decay rates (i.e. short radiative decay times) represent preferred emitter materials for OLED applications. In the subsequent sections, we will come back to these requirements from a photo-physical as well as from a chemical structure point of view. It is not excluded that in future singlet emitters, taking advantage of the singlet harvesting effect, might more easily meet the requirements for bright OLED lighting.

3. HOMO–LUMO excitations and energy states

Frequently, it seems to be suitable to discuss electronic properties of organo-transition metal complexes on the basis of HOMO–LUMO excitations. However, this can be misleading. For example, such a simple model does not comprise singlet or triplet states or, if these states are deduced just from the HOMO–LUMO excitation, it might occur that the resulting triplet does not represent the one of lowest energy. In the scope of this section, we want to present some useful considerations on a schematic basis to help to develop a better understanding of excitations between molecular orbitals (MOs) and how these relate to energy states.

Fig. 3 displays a small number of frontier orbitals, which are often expected to be mainly responsible for a qualitative description of the lower lying energy states. The diagram represents orbitals for a quasi-octahedral organo-transition metal complex, such as Ir(ppy)$_3$ (**52**), with three chelating ligands that have π and π^* orbitals in the relevant energy range. Under assumption of a symmetry of the complex lower than C_3, one obtains three π and three π^* molecular orbitals. Moreover, three d-orbitals, representing the split t_{2g} set, are also shown. The designation, particularly in the range of the higher lying occupied MOs, gives only the leading contribution of these MOs. For example, a d-orbital can also contain π-admixtures, or a π orbital can be mixed with d-character. For the discussions in this section, it is further assumed that the d* orbitals have a very large energy separation from the π^* MOs and therefore do not interfere. However, for blue-light emitters, these orbitals become important, since they may become involved in thermally activated emission quenching (compare Section 5).

For the molecules being of interest here, each occupied orbital contains two electrons with opposite spins. Thus, the configuration $\pi_3{}^2\pi_2{}^2\pi_1{}^2d_3{}^2d_2{}^2d_1{}^2$ gives the electronic singlet ground state S_0. For example, a HOMO–LUMO excitation, representing an MLCT (metal-to-ligand charge-transfer) transition, leads to the excited state configuration $\pi_3{}^2\pi_2{}^2\pi_1{}^2d_3{}^2d_2{}^2d_1{}^1\pi_1{}^{*1}$. For simplicity, let us designate this excitation as $d_1\pi_1{}^*$ or MLCT$_1$ excitation. (According to extensive mixtures between the orbitals, as mentioned above, the overall amount of charge transfer from the metal to the ligands may be rather small even in the case of a formal MLCT excitation.) Taking the spins and spin flips into account, one obtains one singlet state ($^1d_1\pi_1{}^*$ or ^{1}MLCT$_1$) and one triplet state ($^3d_1\pi_1{}^*$ or ^{3}MLCT$_1$). Similarly as described in Section 2 and Fig. 1, the triplet term (=state) consists of three substates. Considering additionally electron–electron interaction (exchange interaction) between the electrons in the two orbitals (d_1 and $\pi_1{}^*$), the singlet and triplet states usually split significantly, for example by several thousand cm^{-1} [78,79]. It is remarked that the amount of splitting between the lowest singlet and triplet state strongly depends on the states' orbital parentage. For states of MLCT character, for example, $\Delta E(S_1 - T_1)$ is significantly smaller (several 10^3 cm^{-1} [78]) than for states which are mainly localized at the ligands, i.e. ligand centered (LC) $\pi\pi^*$ states (order of 10^4 cm^{-1} [30,78]). This is a consequence of the fact that in the former case, the interactions between the unpaired electrons are smaller due to the larger spatial separation of the involved orbitals. Further, if SOC is taken into account, the triplet state splits into three substates. The corresponding zero-field splittings (ZFS) lie in the range of less than 1 cm^{-1} up to more than 200 cm^{-1}, depending on the strength of SOC according to the position of the central metal in the periodic table and on the extent of spin–orbit coupling of this triplet state with higher lying ^{1,3}MLCT states of different configurations (see Section 4). It is mentioned that spin–spin interactions can be ignored in the scope of the discussion of this contribution, since they only lead to splittings of the order of 0.1 cm^{-1} (compare Refs. [29,30,80–82]).

In summary, an excitation from an occupied orbital to an unoccupied orbital leads to four energy states. Consequently, excitations involving all MOs shown in Fig. 3 (18 excitations without including the d* orbitals) give 72 energy states. A quantitative description taking configuration interaction (CI) and spin–orbit coupling (SOC) into account will lead to significant energy shifts and modifications of the electronic states. Thus, it becomes clear that a simple HOMO–LUMO consideration can be very misleading.

For completeness, it is remarked that according to a quantum mechanical investigation of Ir(ppy)$_3$ by Nozaki [83], even the 72 states of our model would not be sufficient to approach the experimental situation. Only an inclusion of about 200 states, meaning 32 additional excitations between MOs, might result in a somewhat more realistic description. Interestingly, about 70 states lie within an energy range of about 8000 cm^{-1} ($\approx$1 eV) above the emitting state [83], exemplifying the high density of energy states and the complexity of a reliable calculation (compare also Refs. [84,85]).

Nevertheless, relatively simple guidelines for the evaluation of the dominating SOC routes (Section 4 and [79,86,87]) and an experimentally based systematics (Section 6) allow us to develop a deeper understanding of how spin-orbit coupling, zero-field splitting, and emission decay times are related.

4. Spin–orbit coupling in organo-transition metal compounds

In this section, we want to take a closer look at spin–orbit coupling and its impact on the properties of the emitting triplet state. It is not intended to provide detailed theoretical formalisms, but we want to present some general schemes and useful trends which are understandable also for non-specialists. Thus, no numerical data will be given and descriptions based on quantum mechanical relations will be restricted to some basic considerations.

4.1. Orbitals and states

An introduction to the frontier orbitals of organo-transition metal compounds and the resulting singlet and triplet states is already given in Section 3. However, in the scope of discussions of spin–orbit coupling, we will restrict our model to a simple 4-orbital-model that involves two occupied d-orbitals d_1 and d_2 centered at the metal ion and one occupied and one unoccupied π- and π^*-orbital, respectively, which are centered at a ligand.

In this model, the four orbitals are occupied by six electrons. Thus, the ground state is given by a closed-shell $d_1{}^2 d_2{}^2 \pi^2$ electron configuration and represents a singlet. Promotion of a single electron with or without a spin-flip can lead to six different states (terms), which are depicted in Fig. 4. The upper left index corresponds to the spin multiplicity (2S+1) which is three for a triplet with a total spin quantum number of $S = 1$ and one for a singlet with $S = 0$. The spins of the unpaired electrons add up to the magnetic spin quantum number M_S. In the case of single excitations, two unpaired electrons result and the possible values of M_S are +1, 0, and -1. The values of $M_S = \pm 1$ correspond to two substates of a triplet. The third triplet substate is given by a positive linear combination of the two possible configurations with $M_S = 0$. On the other hand, the respective negative linear combination describes the corresponding singlet state. For clarity, we drop the index $M_S = 0$ for singlet states from now on.

As already mentioned in Section 3, the simple schemes depicted in Figs. 3 and 4 do not include the exchange interaction, which can – depending on the orbital nature of the respective states – lead to an energy splitting of several thousand cm^{-1} between the singlet and the corresponding triplet state. Further, note that all visualized states in Fig. 4 are pure states with respect to their spin and their orbital nature, i.e. no mixing between states of different and also of the same spin multiplicity is yet taken into account.

4.2. Direct spin–orbit coupling between MLCT states

At first, we assume that the ^{3}MLCT state $^3(d_1\pi^*)$ represents the triplet state of lowest energy. Formally, the substates of this triplet can undergo spin–orbit coupling with all other (sub)states depicted in Fig. 4. However, since the spin–orbit coupling Hamiltonian is a sum of one-particle operators, only (sub)states can be coupled by SOC which differ in just one spin–orbital[1] and which obey the selection rule $\Delta M_S = 0, \pm 1$, according to the Slater–Condon rules for matrix elements of such operators [88]. Further, even if these conditions are fulfilled, many of the possible coupling routes contribute only little with respect to a few dominating routes and thus can be neglected [79,86,87].

Let us, for example, focus on the $M_S = +1$ substate of the $^3(d_1\pi^*)$ state, i.e. the $^3(d_1\pi^*)_{+1}$ substate.[2] Spin–orbit coupling between this substate and the singlet and triplet $\pi\pi^*$-states (^{1,3}LC states) depicted in Fig. 4 is weak, since the d_1- and the π- or π^*-orbitals are located at different atomic centers. According to quantum mechanics, the resulting matrix elements can be described as two- or three-center integrals, which are – due to the exponential decay of each orbital with increasing distance from its center – vanishingly small and thus can be neglected. Moreover, the $^3(d_1\pi^*)_{+1}$ substate can formally also couple with the singlet MLCT state resulting from the same d-orbital, i.e. with $^1(d_1\pi^*)$. In this case, a one-center integral on the metal, which has a large coupling constant, would result. However, the SOC operator cannot couple the d_1-orbital with itself (for details, see e.g. Refs. [87,88]). As a consequence, SOC between a ^{3}MLCT$_1$ substate and the ^{1}MLCT$_1$ state stemming from the *same* d-orbital can be neglected [79,83,86,87,89,90]. On the other hand, strong spin–orbit interaction can result by the coupling of $^3(d_1\pi^*)_{+1}$ with the singlet and triplet MLCT$_2$ (sub)states involving the *different* orbital d_2, namely with $^1(d_2\pi^*)$, $^3(d_2\pi^*)_0$ and $^3(d_2\pi^*)_{+1}$.[3] In these cases, two different central metal d-orbitals are coupled by the SOC operator at the central metal ion, thus only one-center integrals at the metal center with a large SOC constant result.

The impact of these effective spin–orbit coupling paths on the photophysical properties of the $^3(d_1\pi^*)_{+1}$ substate can be illustrated by using perturbation theory. For the sake of simplicity, we will constrain the present consideration on SOC of $^3(d_1\pi^*)_{+1}$ with the $^1(d_2\pi^*)$ state. The couplings with the $M_S = 0$, +1 substates of $^3(d_2\pi^*)$ can be treated equivalently. The SOC perturbed substate $^3(d_1\pi*)^{SOC}_{+1}$ can (in first order) be written as [29,30,87]

$$^3(d_1\pi^*)^{SOC}_{+1} = {}^3(d_1\pi^*)_{+1} + a \cdot {}^1(d_2\pi^*) \tag{5}$$

with the mixing coefficient a given by

$$a = \frac{\left\langle {}^1(d_2\pi^*) \right| H_{SO} \left| {}^3(d_1\pi^*) + 1 \right\rangle}{E\left[{}^3(d_1\pi^*)\right] - E\left[{}^1(d_2\pi^*)\right]} \tag{6}$$

$E[^3(d_1\pi^*)]$ and $E[^1(d_2\pi^*)]$ are the energies of the unperturbed states. Since all three substates of $^3(d_1\pi^*)$ have the same unperturbed energy, the index $M_S = +1$ can be dropped in the energy denominator in Eq. (6). Thereby, the singlet–triplet splitting, as induced by exchange interaction (Section 3) is considered as being already taken into account.

The effects of SOC on the energy stabilization of the $^3(d_1\pi^*)_{+1}$ substate can also be described by perturbation theory. The corrected (perturbed) energy of $^3(d_1\pi^*)_{+1}$ is given by [87].

$$E[^3(d_1\pi^*)^{SOC}_{+1}] = E[^3(d_1\pi^*)] + \frac{\left| \left\langle {}^1(d_2\pi^*) \right| H_{SO} \left| {}^3(d_1\pi^*)+1 \right\rangle \right|^2}{E\left[{}^3(d_1\pi^*)\right] - E\left[{}^1(d_2\pi^*)\right]} \tag{7}$$

Eq. (7) describes the SOC induced energy stabilization of one substate of the $^3(d_1\pi^*)$ term by interaction with the $^1(d_2\pi^*)$ state. The other two substates of the same triplet term can also couple via SOC with this singlet state, if no other symmetry restrictions exist. The corresponding SOC matrix elements are usually of different magnitude, and thus, different energy stabilizations result.

---

[1] A spin–orbital can be written as a product of a spatial orbital times a spin part, frequently used in the notation α or β.

[2] The other substates can be treated equivalently.

[3] Coupling with the $M_S = -1$ substate is not possible, since the selection rule $\Delta M_S = 0, \pm 1$ is not fulfilled.

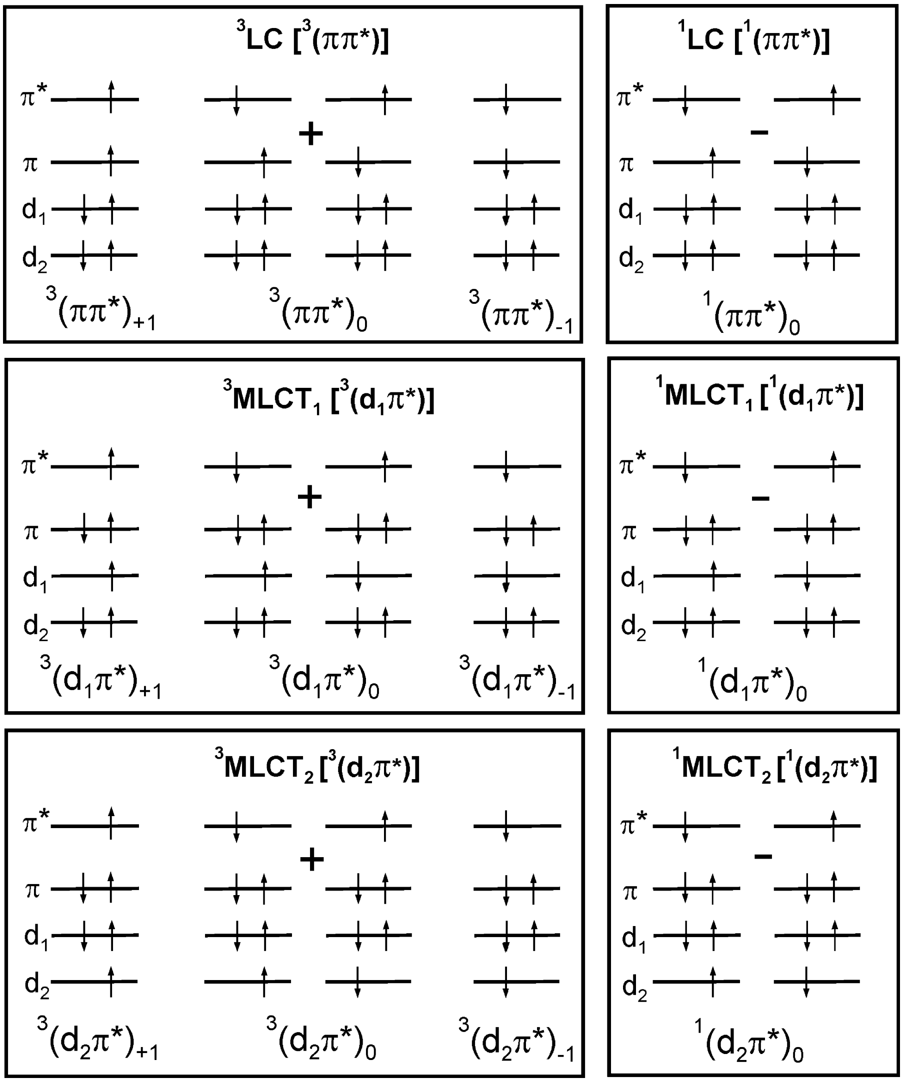

Fig. 4. Orbital occupations and electronic states in a system consisting of four orbitals. Only single excitations are taken into account, thus singlet and triplet states result (compare [86,87]).

As a consequence, a SOC induced zero-field splitting is obtained already by interaction with only one singlet state. Moreover, taking the coupling with the $M_S = 0, +1$ substates of $^3(d_2\pi^*)$ into account as mentioned above, further terms have to be added on the right hand side of Eq. (5), involving other mixing coefficients of the type of Eq. (6). Accordingly, additional contributions to the energy stabilization become effective and a different ZFS results (see, for example, Eq. (12)).

Without SOC interaction, $^3(d_1\pi^*)_{+1}$ is a pure triplet substate and the corresponding radiative transition to the singlet ground state is strictly spin-forbidden. However, with SOC a distinct allowedness of this transition can result. For the case of coupling with only the $^1(d_2\pi^*)$ state, as mentioned above, the radiative rate constant k^r for the perturbed substate may be expressed as [29,87].

$$k^r(^3(d_1\pi^*)^{\mathrm{SOC}}_{+1}) = \frac{64\pi^4\bar{\nu}^3}{3hc^3}\cdot\left|\frac{\left\langle ^1(d_2\pi^*)\right| H_{\mathrm{SO}}\left|^3(d_1\pi^*)+1\right\rangle}{E\left[^3(d_1\pi^*)\right]-E\left[^1(d_2\pi^*)\right]}\cdot\left\langle S_0\right| er\left|^1(d_2\pi^*)\right\rangle\right|^2 \quad (8)$$

with $\bar{\nu}$ and er representing the electronic transition energy in cm^{-1} and the electric dipole operator, respectively. The matrix element $\langle S_0| er |^1(d_2\pi^*)\rangle$ represents the transition dipole moment between the electronic singlet ground state S_0 and the $^1(d_2\pi^*)$ state. Thus, the radiative rate depends on the allowedness of this singlet–singlet transition, i.e. on its oscillator strength. It is stressed again that the other substates of the $^3(d_1\pi^*)$ state experience different admixtures due to different mixing coefficients in analogy to Eq. (6) and thus, will show different radiative rates.

4.3. Indirect spin–orbit coupling to LC states

Now we assume that the lowest triplet state is the ligand centered state $^3(\pi\pi^*)$ and we will illustrate coupling routes for its $M_S = +1$ substate. When considering spin–orbit coupling of this substate with any other electronic (sub)state depicted in Fig. 4, it can be derived that only matrix elements representing two- or three-center integrals occur [86,87]. Thus, direct SOC between the $^3(\pi\pi^*)_{+1}$ substate and higher lying states is negligible. However, even for transition metal compounds with ligand centered T_1 states, larger zero-field splittings and much higher radiative rates than typically found for organic molecules are frequently observed. Similarly as argued above, Azumi, Miki, Crosby, and co-workers [91] have shown that these observations cannot be rationalized by direct SOC between the ^{3}LC substates and higher lying ^{1}MLCT

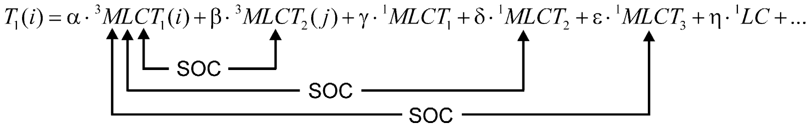

$$T_1(i) = \alpha \cdot {}^3MLCT_1(i) + \beta \cdot {}^3MLCT_2(j) + \gamma \cdot {}^1MLCT_1 + \delta \cdot {}^1MLCT_2 + \varepsilon \cdot {}^1MLCT_3 + \eta \cdot {}^1LC + \ldots$$

Fig. 5. Schematic illustration of leading admixtures to substate *i* of the ^{3}MLCT$_1$ state by direct spin–orbit coupling (SOC). *j* denotes a specific substate. MLCT$_1$, MLCT$_2$, and MLCT$_3$ denote the states which involve the orbitals d$_1$, d$_2$ and d$_3$, respectively.

states.[4] Instead, a two-step mechanism was suggested. It consists of configurational mixing (configuration interaction, CI) of the ^{3}LC substates with ^{3}MLCT substates and subsequent direct SOC of the latter ones with ^{1}MLCT states[5] [82,91,92]. A similar approach published by Giesbergen and Glasbeek makes use of molecular orbital theory, assuming significant mixing of metal d-orbitals with ligand π-orbitals [93].

In the following description, we consider again a very simplified 3-state model, involving the purely ligand centered T$_1$ substate $^3(\pi\pi^*)_{+1}$, the triplet MLCT$_1$ substate $^3(d_1\pi^*)_{+1}$, and the singlet MLCT$_2$ state $^1(d_2\pi^*)$. $^3(\pi\pi^*)_{+1}$ can mix via configuration interaction with the $^3(d_1\pi^*)_{+1}$ substate, since the CI selection rules $\Delta S = 0$ and $\Delta M_S = 0$ are fulfilled. Treating CI as the only perturbation, the ^{3}LC substate can be expressed as [81,82,91]

$$^3(\pi\pi^*)^{\mathrm{CI}}_{+1} = {}^3(\pi\pi^*)_{+1} + b \cdot {}^3(d_1\pi^*)_{+1} \tag{9}$$

with the CI mixing coefficient *b* given by

$$b = \frac{\left\langle {}^3(d_1\pi^*)_{+1} \middle| H_{CI} \middle| {}^3(\pi\pi^*)_{+1} \right\rangle}{E\left[{}^3(\pi\pi^*)\right] - E\left[{}^3(d_1\pi^*)\right]} \tag{10}$$

H_{CI} is the configuration interaction Hamiltonian. A large mixing coefficient *b* leads to a significant ^{3}MLCT perturbation of the ^{3}LC substate. It is stressed that CI acts equally also for the two other triplet substates. This means that CI as the only perturbation does not lead to *different* energy stabilizations of the substates and thus, no zero-field splitting occurs. However, the admixed $^3(d_1\pi^*)_{+1}$ substate can in turn, as expressed by Eq. (5), contain admixtures of the $^1(d_2\pi^*)$ state via SOC, as discussed in Section 4.2. Thus, one has to deal with a combination of both configuration interaction and spin–orbit coupling as perturbation. This leads to an expression for the doubly perturbed ^{3}LC substate

$$^3(\pi\pi^*)^{\mathrm{CI/SOC}}_{+1} = {}^3(\pi\pi^*)_{+1} + b \cdot {}^3(d_1\pi^*)_{+1} + c \cdot {}^1(d_2\pi^*) \tag{11}$$

with the mixing coefficient *b* as given in Eq. (10), while *c* represents a coefficient that can be expressed by different matrix elements and energy denominators (compare [87]). Even for this relatively simple model, a perturbational approach for the description of the energy stabilization of the $^3(\pi\pi^*)_{+1}$ substate and the radiative rate with respect to its transition to the singlet ground state becomes rather complicated. However, even without giving explicit equations, it should become obvious that, due to the involvement of different matrix elements, i.e. for CI and for SOC, and different energy denominators, this indirect SOC path to the substates of a ^{3}LC state has less influence on the ZFS and the radiative decay rates than direct SOC to the substates of a ^{3}MLCT.

4.4. Treatments in realistic systems

The simple model dealing just with states created from four frontier orbitals, as presented above, does not hold for a more realistic treatment of spin–orbit coupling in organo-transition metal compounds, since there is a large number of higher lying singlet and triplet states which also have to be taken into account (see Section 3). Many of these states can significantly contribute to the emitting triplet substates via direct or indirect SOC, if the selection rules for SOC are fulfilled, if the resulting matrix elements correspond to one-center integrals at the central metal ion, and if no symmetry restrictions are effective. For the leading admixtures to substate *i* of a T$_1$ state of MLCT character, this is schematically depicted in Fig. 5. The parameters α, β, γ, etc. represent the respective mixing coefficients. As described above, the mixing of ^{3}MLCT$_1$(i) with the singlet MLCT$_1$ state stemming from the *same* d-orbital can be neglected. Moreover, any mixing with singlet or triplet LC states is also negligible.

In such a somewhat more realistic treatment of SOC, the energies and radiative rates can, at least in principle, be expressed by Eqs. (12) and (13), as given below. Here, we apply the nomenclature which is also used for the case studies presented later in this contribution. This means that the lowest triplet term consists of the substates I, II, and III. If only direct SOC is considered, the energy $E(i)$ of the ^{3}MLCT substate i (with i = I, II, III) is given by [29,87,94]

$$E(i) = E_{\mathrm{T}_1} + \sum_{n,j} \frac{\left|\left\langle \mathrm{T}_n(j) \middle| H_{\mathrm{SO}} \middle| \mathrm{T}_1(i) \right\rangle\right|^2}{E[\mathrm{T}_1] - E[\mathrm{T}_n]} + \sum_m \frac{\left|\left\langle \mathrm{S}_m \middle| H_{\mathrm{SO}} \middle| \mathrm{T}_1(i) \right\rangle\right|^2}{E[\mathrm{T}_1] - E[\mathrm{S}_m]} \tag{12}$$

while the radiative rate $k^r(i)$ can be expressed by [29,87,89]

$$k^r(i) = \frac{64\pi^4 \bar{\nu}^3}{3hc^3} \cdot \left| \sum_m \frac{\left\langle \mathrm{S}_m \middle| H_{\mathrm{SO}} \middle| \mathrm{T}_1(i) \right\rangle}{E[\mathrm{T}_1] - E[\mathrm{S}_m]} \cdot \left\langle \mathrm{S}_0 \middle| er \middle| \mathrm{S}_m \right\rangle \right|^2 \tag{13}$$

$E[\mathrm{S}_m]$ and $E[\mathrm{T}_n]$ are the unperturbed energies of higher lying (pure) singlet states S_m and (pure) triplet states T_n. $\mathrm{T}_n(j)$ characterizes a substate *j* of T_n. Eqs. (12) and (13) are the generalizations of Eqs. (7) and (8), respectively. SOC with the most proximate ^{3}MLCT state(s) of a different orbital nature presumably dominates the individual energy stabilizations of the T$_1$ substates and thus the amount of zero-field splitting. This is simply a consequence of the smaller energy denominators ($E[\mathrm{T}_1] - E[\mathrm{T}_n]$) as compared to ($E[\mathrm{T}_1] - E[\mathrm{S}_m]$). On the other hand, an admixture of triplets can be neglected for the determination of the radiative rates, since the corresponding dipole matrix elements vanish.

The situation is different, if the lowest triplet state represents a ^{3}LC state. As outlined in Section 4.3, SOC becomes effective indirectly via configuration interaction. Thus, Eqs. (12) and (13) have to be modified. This leads to complicated formulas, since a huge manifold of possible paths of CIs and SOCs to higher lying states/substates has to be considered. This situation is illustrated schematically in Fig. 6. The relevant coupling paths of a substate of ^{3}LC character to two singlet MLCT states and to substates of two triplet MLCT states are depicted. According to the considerations of the previous sections, even in this simplified scheme two coupling paths of CI and three paths of SOC are included. The parameters α, β, γ, δ, and ε in Fig. 6 represent mixing coefficients and display the contributions of the respective (sub)states in the emitting substate T$_1$(i).

---

[4] It is remarked that frequently direct SOC between ^{3}LC and ^{1}MLCT states is erroneously assumed.

[5] Configuration interaction (CI) is based on electron–electron interaction. Thus, CI induced mixing can only occur between states of equal spin multiplicity.

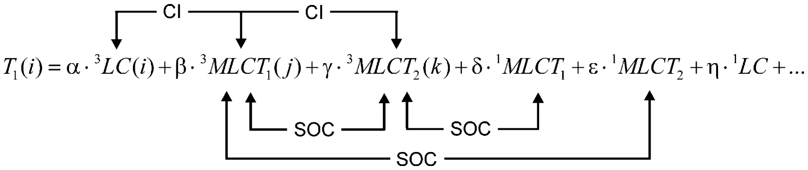

$$T_1(i) = \alpha \cdot {}^3LC(i) + \beta \cdot {}^3MLCT_1(j) + \gamma \cdot {}^3MLCT_2(k) + \delta \cdot {}^1MLCT_1 + \varepsilon \cdot {}^1MLCT_2 + \eta \cdot {}^1LC + \ldots$$

Fig. 6. Schematic illustration of leading admixtures to substate *i* of a T_1 state of ^{3}LC character by indirect spin–orbit coupling (SOC). CI represents configuration interaction, *j* and *k* are substate indices. $MLCT_1$ and $MLCT_2$ denote the states which involve the orbitals d_1 and d_2, respectively.
Adapted from Ref. [87].

4.5. Spin–orbit coupling and coordination geometry

The relations derived in the previous sections demonstrate that, for both direct and indirect coupling paths, large SOC matrix elements are necessary to obtain significant zero-field splitting and radiative rates. Moreover, it was shown that also energy denominators, i.e. the energy differences between the unperturbed substate and the perturbing states, play an important role. In particular, the larger the energy separation between two states, the smaller is their mixing via SOC or CI.

Already these simple considerations allow us to work out very useful guidelines for the effectiveness of SOCs and their impact on emission properties. This becomes clear, if one takes into account that these energy separations depend significantly on the geometry of a compound, the number of ligands coordinating to the central metal ion, and the ligand field splitting [95,96]. If, in a first order approximation, one assumes that for the different MLCT states, e.g. $d_1\pi^*$, $d_2\pi^*$, etc., the singlet–triplet splittings (given by exchange interactions) are similar, one can consider just the separations between the orbital energies. Frequently, this concept meets the chemical intuition [79,86,87].

Fig. 7 depicts the splitting of the central metal d-orbitals (a) for an octahedral (O_h) and a distorted octahedral compound and (b) for a square-planar (D_{4h}) and a distorted square-planar compound. For this model discussion, one π^*-orbital, representing the lowest unoccupied molecular orbital (LUMO), is also given. Other unoccupied π^*-orbitals and occupied π-orbitals are neglected here for clarity. Thus, all considered electronic states are MLCT states with a central-metal d-orbital as the highest occupied molecular orbital (HOMO).

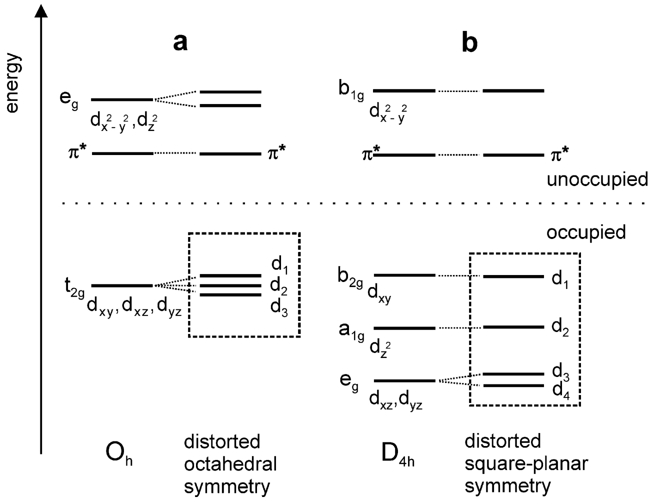

Fig. 7. Schematic splitting of the d-orbitals (a) in an octahedral and a distorted octahedral compound and (b) in a square-planar and a distorted square-planar compound. The frames display the different splitting of the occupied d-orbitals. In all cases a π^*-orbital, representing the LUMO, is displayed in addition. The unoccupied d-orbitals are only given for completeness.
Adapted from Ref. [87].

In the case of perfect octahedral symmetry (O_h symmetry), the d-orbitals split into sets of three t_{2g} and two e_g orbitals, separated by 10 Dq with Dq being the ligand field parameter [95,96]. For metal ions with a d^6 configuration, such as Ir(III), Os(II), and Ru(II), the t_{2g}-shell is fully occupied. For compounds of relevance for OLED applications, the unoccupied e_g-orbitals have to have energies high above the LUMO to prevent quenching by dd* states (compare Section 5.2.1). For most octahedrally coordinated complexes discussed in this contribution (see Fig. 9), the symmetry is lower than C_3. As a consequence, the orbitals of the t_{2g} manifold are no longer degenerate and split into the three orbitals d_1, d_2, and d_3, according to the respective geometrical distortion. However, they will still be rather proximate in energy. For $[Ru(bpy)_3]^{2+}$ (**38**), for example, a t_{2g} splitting of only a few hundred wavenumbers is reported [97–99]. According to the relations derived above, the substates of the lowest ^{3}MLCT state $^3(d_1\pi^*)$ can experience efficient SOC with the relatively close-lying singlet states $^1(d_2\pi^*)$ and $^1(d_3\pi^*)$ and the substates of the corresponding triplets $^3(d_2\pi^*)$ and $^3(d_3\pi^*)$, since the energy denominators are relatively small. As a consequence, large zero-field splittings and relatively high radiative rates can occur for the transitions between the $^3(d_1\pi^*)$ substates and the ground state.

For quasi-square-planar compounds a different situation is found. For central metal ions exhibiting a d^8 electron configuration, such as Ir(I), Pt(II), and Pd(II), the four lower lying d-orbitals are occupied. The ordering of these orbitals depends strongly on the nature and the bonding abilities of the coordinating ligands [95,96,100]. The depicted order, as shown in Fig. 7, is obtained from ligand field theory without considering additional (back)bonding effects. The splitting between the occupied orbitals is larger than for quasi-octahedrally coordinated compounds. Again, the unoccupied antibonding $d_{x^2-y^2}$ orbital is strongly destabilized and shifted to high energy for strong-field ligands. In analogy to the situation described above, the substates of the lowest ^{3}MLCT state $^3(d_1\pi^*)$ can exhibit SOC with the singlet states $^1(d_2\pi^*)$, $^1(d_3\pi^*)$ and $^1(d_4\pi^*)$, as well as with the substates of the corresponding triplets $^3(d_2\pi^*)$, $^3(d_3\pi^*)$, and $^3(d_4\pi^*)$. However, in this case, the energy differences between d_1 and the other occupied d-orbitals d_2, d_3, and d_4 are, for most compounds, distinctly larger than for quasi-octahedrally coordinated compounds (Fig. 7). For $[Pt(CN)_4]^{2-}$, for example, the energy difference between the highest occupied d-orbitals (HOMO and HOMO−1) is as high as about 4000 cm^{-1} (0.5 eV) [100]. Consequently, the energy denominators which govern the mixing between the MLCT states are significantly larger in this case than for quasi-octahedral coordination. Thus, for quasi-square-planar compounds the efficiency of SOC will not attain the one of quasi-octahedral compounds. (compare also [101]).

For the sake of clarity, the presented discussion was focused on emitting states of MLCT character, neglecting ^{3}LC states. However, the described influence of a compound's coordination geometry on its SOC induced photophysical properties is also valid for emitting states that are largely of ligand centered character. In this case, the ^{3}LC substates gain singlet character only via the proposed two-step mechanism. Accordingly, the relative energy differences of the lowest triplet LC state to higher lying triplets of MLCT character have to be taken into account, which, in first order, are governed

Table 1
Selected photophysical properties of several Ir(N^C)$_2$(acac) and Pt(N^C)(acac) compounds.

Compound[a]	λ_{em} (300 K) [nm]	ΔE(ZFS) [cm^{-1}]	k^r(300 K) [s^{-1}][b]	References
Ir(4,6-dFppy)$_2$(acac) (**47**)	484	109	64×10^4[c]	[87,102,103]
Pt(4,6-dFppy)(acac) (**15**)	467	8	8.0×10^4[c]	[87,104–106]
Ir(thpy)$_2$(acac) (**33**)	567	33	12×10^4[d]	[107]
Pt(thpy)(acac) (**12**)	558	4	2.6×10^4[d]	[108,109]
Ir(s1-thpy)$_2$(acac) (**20**)	586	16	9.8×10^4[d]	[107,109]
Pt(s1-thpy)(acac) (**6**)	577	<1	2.1×10^4[d]	[108,109]
Ir(pbt)$_2$(acac) (**46**)	557	100	14×10^4[e]	[110–112]
Pt(pbt)(acac) (**17**)	539	10	6.0×10^4[d]	[106,113]

[a] Additional data are given in Table 2.
[b] k^r(300 K) represents the averaged radiative decay rate, which involves the emission of all three T$_1$ substates (compare Section 6) It is calculated according to Eq. (3) from the emission quantum yield and the decay time measured at ambient temperature.
[c] Measured in CH_2Cl_2.
[d] Measured in PMMA.
[e] Measured in 2-Me-THF.

by the energy separations between the highest occupied π- and d-orbitals.

Of course, the presented model based on simple considerations of ligand field splittings can be regarded as being oversimplified for a quantitative description of realistic systems. However, a comparison of photophysical properties of quasi-square-planar with quasi-octahedral transition metal compounds with "similar" central metal ions and identical ligands reflects the trends and predictions given above. For instance, Table 1 lists four such pairs of Ir(III) and Pt(II) complexes. Both central metal ions have comparable spin–orbit coupling constants. Pt(II) complexes exhibit a d^8 electron configuration and form quasi-square-planar compounds, while Ir(III) compounds with a d^6 configuration are usually quasi-octahedrally coordinated.

Table 1 compares the total zero-field splittings ΔE(ZFS) and (averaged) radiative decay rates at ambient temperature for a series of Pt(N^C)(acac) and Ir(N^C)$_2$(acac) couples. (N^C is an anionic cyclometallating ligand and acac is acetylacetonate. Chemical structures are shown in Fig. 9.) The respective emission maximum at 300 K is also given.

It can clearly be seen that for all couples listed the total zero-field splitting of the emitting triplet state and the radiative rate are significantly larger for the Ir(III) than for the respective Pt(II) compounds. In Section 6, we will come back to this important trend which relates the amount of zero-field splitting to the character of the emitting state and to the spin–orbit coupling efficiency. The higher this splitting, the larger is the MLCT character of the T$_1$ state and the more efficient is SOC. This leads to higher radiative rates for the transitions from the T$_1$ substates to the ground state S$_0$. In summary, all listed quasi-octahedral Ir(N^C)$_2$(acac) compounds exhibit more efficient SOC than the related quasi-square-planar Pt(N^C)(acac) compounds. This observation is in agreement with the simple model presented above.

5. Nonradiative processes

In the previous section, it was derived that organo-transition metal compounds can exhibit relatively high radiative rates for the transitions from the T$_1$ substates to the singlet ground state. However, this is not sufficient to obtain high emission quantum yields. According to Eq. (3), it is of crucial importance to minimize also the rate constants of nonradiative deactivation processes of the T$_1$ state. The significance of quenching processes for the electroluminescence performance has already been mentioned in Section 2. In this section, we want to summarize processes which can induce nonradiative decay and thus can strongly reduce the photoluminescence quantum yield ϕ_{PL} of an organo-transition metal compound.

5.1. Intermolecular quenching

For intermolecular quenching of the emission, at least one other molecule of the same or of a different species is necessary. If molecules of the same species are involved, luminescence quenching preferably occurs at higher dopant concentrations via annihilation of excited emitters in close proximity (e.g. triplet–triplet-annihilation [67,68,70,114]) or via energy transfer according to the Förster and/or the Dexter mechanism [30] from excited to non-excited molecules. Another process of self-quenching is frequently found for Pt(II) compounds, since their square-planar coordination geometry facilitates axial intermolecular interactions [115–117]. Self-quenching and annihilation effects can usually be avoided by using low dopant concentrations or by effectively shielding the emitter molecules. This can, for example, be reached by using bulky [118,119] or dendrimeric ligands [120–122].

Energy transfer to impurities can also result in very efficient quenching. In the scope of this contribution, we only want to mention quenching induced by molecular oxygen. For photoluminescent materials with relatively long emission decay times, as compared to fluorescent emitters, this quenching process is frequently very effective. The corresponding mechanism is usually described as energy transfer from an excited emitter to triplet oxygen ($^3O_2$) with subsequent conversion to the excited singlet oxygen ($^1O_2$) [123–125]. However, also electron transfer processes are not negligible, as has been suggested for some Ir(III) compounds which exhibit extremely high oxygen quenching rates [126]. To avoid quenching by O_2, fluid solutions of the materials have to be carefully and quantitatively deaerated. It should be noted that molecular oxygen diffuses also through many polymeric matrices [127,128]. Thus, also films doped with triplet emitters should be handled in an inert atmosphere. The tendency to undergo oxygen quenching is usually, but not in all cases, correlated with a long emission decay time of an emitter. As a consequence, also in this respect short radiative emission decay times are favorable. For oxygen sensor applications, on the other hand, long emission decay times and high quenching constants are desired to obtain a high sensitivity [128–130].

In fluid solutions, the solvent can also efficiently quench the emission of an organo-transition metal compound by forming exciplexes of an excited emitter and a solvent molecule [131–133]. Exciplex quenching is especially efficient between electrophilic emitters and strongly nucleophilic solvents. Recently, an extremely electrophilic Pt(II) compound was reported, of which the emission is strongly quenched even by poor Lewis bases. In the non-polar cyclohexane, on the other hand, a high emission quantum yield was obtained [134].

5.2. Intramolecular quenching

In contrast to intermolecular quenching shortly addressed above, intramolecular emission quenching is an intrinsic property of a molecule in an inert matrix. For organo-transition metal compounds, intrinsic nonradiative decay is frequently ascribed to two mechanisms, which are shortly summarized below.

5.2.1. Thermal population of metal-centered states

A number of transition metal compounds shows a phosphorescence of high quantum yield at 77 K, but at ambient temperature this emission is strongly or even totally quenched. In many cases, this phenomenon can be ascribed to the thermal population of metal-centered states of dd* character, so-called ligand-field (LF) states [38,135–139]. These have strongly distorted excited state geometries with respect to the geometry of the ground state. This leads to high nonradiative decay rates [79,140]. Recent quantum mechanical calculations performed on Ir(III) compounds relate this distortion to significant elongations of metal–ligand bond lengths [141] or even to the breaking of bonds and the formation of a trigonal bipyramidal species [38,142]. This quenching is particularly restricting for the development of blue light emitting materials with ortho-metallating ligands. An example, given by the couple of Pt(ppy)(acac) (**18**) and Pt(4,6-dFppy)(acac) (**15**), will illustrate this problem. While the first compound is a green light emitter with $\phi_{\mathrm{PL}} = 20\%$ [143], the second one exhibits a sky-blue emission with a ϕ_{PL} value of only 2% [87,106], both measured in deaerated fluid solutions at ambient temperature. For both compounds, it may be assumed that the ligand field dd* states lie at approximately the same energy. However, the activation energy for the population of these states from the emitting triplet state is significantly smaller for the blue light emitter. Consequently, efficient emission quenching can occur via this mechanism. A corresponding behavior is also observed for the blue light emitting Ir(biqa)$_3$ complex (**41**), as is shortly addressed below (see Table 3).

Strategies to avoid the thermal population of the ligand-field states by "pushing" them to higher energies and making them thermally inaccessible at ambient temperature apply, for example, chromophoric ligands with very high ligand field strengths, such as carbenes [144–146]. Further, it has been reported that also in Pt(II) compounds with terdentate dipyridylbenzene N^C^N ligands, the dd* states are shifted to higher energies when compared to compounds with bidentate phenylpyridine-based N^C ligands. This is ascribed to the shorter Pt–C bond lengths in the terdentate complexes [147–149]. Another possibility to shift these quenching states out of reach at ambient temperature is given by the use of strong-field ancillary ligands such as CO and CN$^-$ [150–152]. With these strategies, however, the occupied d-orbitals are usually also stabilized. As a consequence, the emitting state can change its character from a ^{3}MLCT to a ^{3}LC type. This would be disadvantageous, since the SOC efficiency and thus the radiative decay rates would strongly decrease. (For further discussions of these implications see also Section 6.)

Interestingly, thermal population of the ligand-field dd* states can also be influenced by the host environment. In contrast to fluid solutions, geometrical distortions of a compound's geometry are often largely suppressed in rigid host matrices. As a consequence, quenching dd* states are shifted to higher energies and their population at ambient temperature is reduced. The very low emission quantum yield of Pt(4,6-dFppy)(acac) (**15**) of $\phi_{\mathrm{PL}} = 2\%$ in fluid solution, for example, increases strongly to $\phi_{\mathrm{PL}} = 50\%$ when the material is doped into a PMMA host [87]. Similarly, Ru(II) polypyridine complexes incorporated into rigid host media like zeolites [153], oxalate networks [154], glasses [155], and polymeric matrices [156] were reported to exhibit distinctly higher emission quantum yields than in fluid solutions.

For completeness, it is mentioned that these problems concerning the generation of blue light emission might presumably be avoided by using materials with fully occupied d-orbitals, e.g. Cu(I)-compounds (compare Section 9 and Refs. [43–46]).

5.2.2. Quenching of the excited state by vibrational coupling to the ground state

Radiationless processes from an electronically excited state to the singlet ground state S$_0$ can be effective via an involvement of vibrational modes of the ground state. This phenomenon is often termed vibrational quenching. For a theoretical description, detailed formalisms based on Fermi's golden rule have been derived already more than four decades ago [157–160]. In the low temperature limit of weak electronic coupling and large energy gaps between the involved electronic states, an expression can be derived that allows to describe the radiationless rate k^{nr} in dependence of an electronic coupling factor β, factors that are determined by the vibrational overlap of the involved wavefunctions, and solvent effects. In particular, the famous energy gap law, predicting an exponential increase of k^{nr} with decreasing energy gap between the excited state and the ground state, results from this theory. The validity of the energy gap law was experimentally verified for fluorescent organic molecules [161–163], polymers [164], and also for phosphorescent organo-transition metal compounds [165–169]. Quenching can occur, when the involved electronic states are coupled by promoting vibrational modes and when subsequent vibrational relaxation takes place via so-called accepting vibrational modes of the electronic ground state. Accordingly, the nonradiative rate for vibrational quenching k^{nr} can be expressed as [165,166,169,170]

$$\ln(k^{nr}) = \ln(\beta) - \frac{1}{2}\ln(a \cdot \hbar\omega_m E_0) - S_m - \frac{\gamma E_0}{\hbar\omega_m} + \left(\frac{\gamma+1}{\hbar\omega_m}\right)^2 \left[\frac{(\Delta\bar{\nu}_{1/2})^2}{16\ln 2}\right] \tag{14}$$

with

$$\gamma = \ln\left(\frac{E_0}{S_m\hbar\omega_m}\right) - 1 \tag{15}$$

The first term of Eq. (14) represents the electronic coupling between the involved electronic states (see below), while the other terms result from the vibrational overlap factor of the initial vibrational mode of the excited state with the vibrational accepting mode m of the ground state being in resonance. $\omega_m = 2\pi\nu_m$ is the angular frequency of the accepting mode m and S_m is the Huang–Rhys parameter. E_0 is the transition energy from the excited electronic (sub)state to the ground state. The Huang–Rhys parameter S_m describes the displacement of the potential energy surfaces of the involved electronic states along the vibrational normal coordinate of the accepting mode m. Within the described framework, the last term treats low-energy intramolecular vibrations and solvent effects classically by describing these interactions collectively by the half-width of the emission bands $\Delta\bar{\nu}_{1/2}$. a is a constant in units of (cm^{-1})$^{-2}$ [166,170]. To first order, Eq. (14) can be simplified, if compounds with similar electronic couplings (represented by β, see below) and similar interactions with the solvent (represented by $\Delta\bar{\nu}_{1/2}$) are compared. Thus, one obtains a more common form of the energy gap law, given by

$$k^{nr} \propto \mathrm{const} \cdot \exp\left(-\frac{\gamma E_0}{\hbar\omega_m}\right) \tag{16}$$

From Eq. (16) it can be seen that the nonradiative rate decreases with increasing electronic transition energy E_0, with decreasing angular frequency ω_m of the accepting vibrational mode, and with decreasing Huang–Rhys parameter S_m, since the latter essentially determines the parameter γ. Thus, especially red emitting compounds with emitting states that are geometrically distorted with respect to the ground state are very sensitive to emission quenching via this mechanism. For blue and green emitting compounds, vibrational quenching is usually weak, as was shown, for example, by an extrapolation of the nonradiative rate to the blue spectral range according to the energy gap law [38].

Further, strategies of enhancing the molecular rigidity to reduce the Huang–Rhys parameters corresponding to the accepting vibrational modes were also successful with regard to a decrease of the nonradiative rate. This can, for example, be done by using compounds with tridentate N^C^N- [147–149] or tetradentate C^N^N^C-coordinating ligands [171] instead of bidentate N^C-ligands. Examples of the latter approach are also given by Pt(ppy$_2$-tBua) (**21**), Pt(tBu$_2$-ppy$_2$-fluoren) (**30**), and Pt(ppy$_2$-fluoren) (**35**), respectively (compare Fig. 9 and Table 2).

The parameter β represents the vibronic coupling between the involved electronic states. In our case, we focus on an emitting triplet state, or more exactly on an individual substate of T$_1$, and on the electronic ground state S$_0$. According to Refs. [160,165], β is essentially determined by a small number of promoting vibrational modes. The contribution of one specific promoting mode k is determined by an expression of the form

$$\left|C_{\mathrm{S,T}}^{k}\right|^{2}\omega_{k}\sqrt{\frac{\pi}{2}} \tag{17}$$

where ω_k is the angular frequency of the promoting vibrational mode k. $C_{\mathrm{S,T}}^{k}$ is given by Eq. (18) and is basically determined by the vibronic coupling matrix element between the wavefunctions of the T$_1$ state, or more exactly of a substate, and the electronic ground state S$_0$.

$$C_{\mathrm{S,T}}^{k}=\frac{\hbar i}{\sqrt{M_k}}\left\langle \phi_{\mathrm{S}}\left|\frac{\partial}{\partial Q_k}\right|\phi_{\mathrm{T}}\right\rangle \tag{18}$$

where M_k is the reduced mass of the specific mode k. This vibrational mode promotes (induces) the coupling between the two states involved (see below). Q_k is the respective normal mode coordinate. ϕ_{S} and ϕ_{T} are the electronic wavefunctions of the ground state S$_0$ and of a substate of the excited triplet state T$_1$, respectively. Note that these wavefunctions depend parametrically on the nuclear geometry, i.e. on the normal coordinates Q_k. In this approach, ϕ_T represents a perturbed wavefunction of one triplet substate. That means the wavefunction is already modified by SOC and contains admixtures from higher lying singlet states. (The structure of corresponding functions is presented in Section 4 in Eqs. (5), (9), and (11)). Further, to a very good approximation, the unperturbed wavefunction of the singlet ground state may be applied for ϕ_{S}.

The message of Eq. (18) can be illustrated by referring to experimental results. For example, it is obvious, that the matrix element in Eq. (18) vanishes for a pure triplet state or becomes small for triplet states with only very small singlet admixtures. Indeed, the investigations carried out for Ir(ppy)$_3$ (**52**) show that the nonradiative rates are distinctly different for the three triplet substates (see Tables 3 and 5). Substate I exhibits only a very small singlet admixture, it represents an almost pure triplet state [40,79,83]. In fact, the nonradiative rate of the transition to the ground state amounts to only $\approx 8\times10^{2}\ \mathrm{s}^{-1}$. On the other hand, the substates II and III experience significant SOC and thus, the wavefunctions have distinct singlet admixtures [40,79,83]. Accordingly, the nonradiative rates of these substates are higher by one and more than two orders of magnitude, respectively (see Table 5). Although the leading promoting mode is not known, it is evident that SOC is important for the nonradiative decay, since all other terms in Eq. (14) are supposed not to vary for the three triplet substates of Ir(ppy)$_3$. For completeness, it is remarked that, with increasing singlet admixtures to the triplet substates of Ir(ppy)$_3$, an even larger increase of the radiative rates is observed. This leads to almost 100% emission quantum yield at ambient temperature (compare Section 8).

A similar behavior is also obvious for the two couples Ir(thpy)$_2$(acac) (**33**)/Pt(thpy)(acac) (**12**) and Ir(s1-thpy)$_2$(acac) (**20**)/Pt(s1-thpy)(acac) (**6**) [107] as presented already in Table 1. In both cases, SOC with respect to the emitting states is more efficient for the Ir(III) than for the Pt(II) compounds. This results in higher radiative rates for the Ir(III) complexes. Moreover, being in line with the discussion of the present section, also the nonradiative rates are larger in the case of more efficient SOC. In particular, for the two couples mentioned, the k^{nr} values are by more than a factor of two larger for the triplet–singlet transitions of the Ir(III) than of the Pt(II) complexes [107]. As another example it is referred to Ir(biqa)$_3$ (**41**) (Table 3). However, this blue light emitter experiences an additional quenching in fluid solution at ambient temperature. Presumably this effect can be explained by thermal population of a relatively close-lying ligand field dd* state, being separated by $\approx 2350\ \mathrm{cm}^{-1}$ from the emitting triplet state [172].

Furthermore, also the derivative $\partial\phi_{\mathrm{T}}/\partial Q_k$ in Eq. (18) can be illustrated by a qualitative model. An interaction between the wavefunctions ϕ_{S} and ϕ_{T} can be promoted by a selective vibrational mode k, if the wavefunction ϕ_{T} changes along the corresponding vibrational coordinate Q_k. For example, in Section 8.5 it will be shown that the environment of an emitter (matrix cage) can alter d- and π-orbital mixing by variations of the cage geometry. These effects can distinctly alter SOC efficiencies. It is likely that corresponding effects will also occur with specific vibrations, which modify the molecular geometry of a complex. Obviously, such effects are not only restricted to low-energy complex-cage modes, but can also be induced (promoted) by other vibrations. Accordingly, the derivative $\partial\phi_{\mathrm{T}}/\partial Q_k$ and the matrix element in Eq. (18) seem to be of high importance.

6. Emission decay times, radiative rates, and zero-field splitting – A systematic approach

The radiative rate of a transition from a triplet state or from one of its substates to the electronic ground state is of crucial importance for many photo-physical properties and most applications that make use of light emission. Thus, a deeper understanding of the factors which control this rate is of extraordinary importance. As described in Section 4, only spin–orbit coupling (SOC) opens a radiative path from a triplet state, or more exactly from its substates, to the singlet ground state. In Eq. (13) it is displayed that the interaction of a triplet substate i (i = I, II, and III) with higher lying singlet states via SOC essentially determines the radiative rate $k^{r}(i)$. These effects of SOC between the states are expressed by the SOC matrix elements and energy denominators. On the other hand, similar and even the same matrix elements are responsible for the energy shifts of the individual triplet substates. The corresponding expression is displayed in Eq. (12). Mostly, each triplet substate experiences a specific SOC-induced energy stabilization. The resulting (small) energy differences between these relatively large shifts give the zero-field splitting parameters $\Delta E_{\mathrm{I,II}}$ and $\Delta E_{\mathrm{I,III}} = \Delta E(\mathrm{ZFS})$, respectively.

Since both photo-physical effects, the ZFS of the T$_1$ state and the radiative allowedness of the transitions from its substates to the singlet ground state, are traced back to the same type of matrix elements, as displayed in Eqs. (12) and (13), it should be possible to relate both expressions. An analytical approach does not seem to be easily achievable and has not yet been carried out. However, if the averaged ambient temperature decay times $\tau_{\mathrm{av}}(300\ \mathrm{K})$ (and for four compounds also the corresponding radiative decay times)

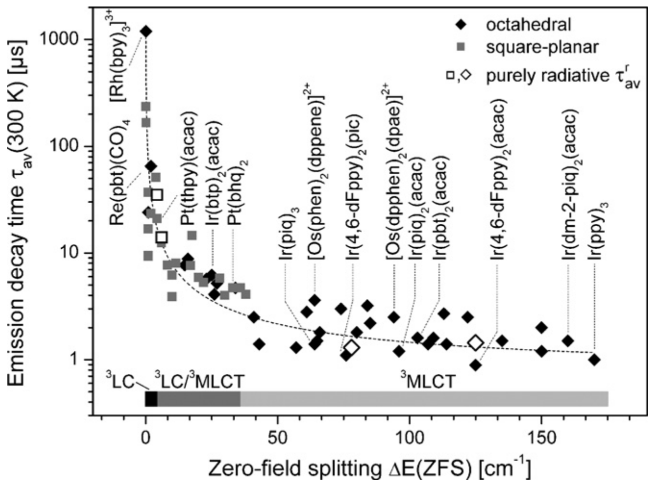

Fig. 8. Emission decay time τ_{av} (300 K) versus the total zero-field splitting ΔE(ZFS). The data points, taken from Table 2, are connected by an eye-guiding curve. τ_{av} (300 K) represents the averaged emission decay time of the three triplet substates at ambient temperature. (For further details see text.) The different symbols (squares and rhombs) label the complex geometries (square-planar and octahedral, respectively). For four compounds (open symbols), the purely radiative decay times have been determined (compare Table 3). The bar in the lower part of the diagram gives a classification of the emitting triplet as ^{3}LC ($^3\pi\pi^*$), ^{3}LC/^{3}MLCT (^{3}LC with significant ^{3}MLCT admixtures), and ^{3}MLCT (^{3}dπ^*), respectively. Compounds with ^{3}LC/^{3}MLCT or ^{3}MLCT character are potentially suited for OLED-applications. The chemical structures of the compounds are shown in Fig. 9.

are plotted versus ΔE(ZFS) as depicted in Fig. 8, it is seen that a functional description of the form

$$\tau_{av}(300\,\text{K}) = f(\Delta E(\text{ZFS})) \tag{19}$$

exists. τ_{av}(300 K) is given by the Boltzmann-weighted average of the individual decay times of the three triplet substates at 300 K. A justification for this approach is given below. The dashed curve shown in Fig. 8 represents simply an eye-guiding function. Empirically, this curve may be described by τ_{av} (300 K) = $a(\Delta E(\text{ZFS}) + b)^{-1} + 0.75\,\mu\text{s}$ with $a = 70\,\mu\text{s}\,\text{cm}^{-1}$ and $b = 0.02\,\text{cm}^{-1}$. τ_{av} (300 K) and ΔE(ZFS) are measured in µs and cm^{-1}, respectively. A qualitative interpretation is given below in this section.

The experimental data that lead to the diagram in Fig. 8 require some comments:

- ΔE(ZFS) represents the total ZFS, expressed by the energy separation $\Delta E_{\text{I,III}}$ between the highest and the lowest T_1 substate. These energies are obtained either from highly resolved spectra or from an analysis of the temperature dependence of the emission decay time. In the latter case, one takes advantage of the fact that, under the assumption of a fast thermalization, the averaged decay time τ_{av} for a system of three excited substates I, II, and III can be written as [173–176]

$$\tau_{av} = \frac{1}{k_{av}} = \frac{1 + e^{-(\Delta E_{\text{I,II}}/k_B T)} + e^{-(\Delta E_{\text{I,III}}/k_B T)}}{k_{\text{I}} + k_{\text{II}} e^{-(\Delta E_{\text{I,II}}/k_B T)} + k_{\text{III}} e^{-(\Delta E_{\text{I,III}}/k_B T)}} \tag{20}$$

  where $k_{\text{I}} = 1/\tau_{\text{I}}$, $k_{\text{II}} = 1/\tau_{\text{II}}$, and $k_{\text{III}} = 1/\tau_{\text{III}}$ represent the individual decay rates (or the reciprocal decay times) of the triplet substates I, II, and III, respectively. $\Delta E_{\text{I,II}}$ and $\Delta E_{\text{I,III}}$ are the energy separations between the T_1 substates.
- The decay time values to be used in this context should be the purely radiative ones. However, this information is not available apart from a few examples (see the open symbols in Fig. 8 and compare Table 3). Therefore, we used the average decay time τ_{av}(300 K), which is extrapolated to ambient temperature by use of Eq. (20) from the individual decay times of the three triplet substates (τ_{I}, τ_{II}, and τ_{III}) and the zero-field splitting values ($\Delta E_{\text{I,II}}$ and $\Delta E_{\text{I,III}}$). These data are summarized in Table 2. This procedure has the advantage that the individual decay times as determined in our studies are largely based on emission properties at cryogenic temperatures at which radiationless deactivation is usually less important (compare Ref. [177]) and therefore, though in a relatively crude approximation, are better suited for the present approach (that would require data for radiative processes) than the *measured* decay times at ambient temperature. In several cases, the emission at ambient temperature is even quenched totally and thus the respective data points would not be available at all. To summarize, the emission properties of the three substates of the emitting triplet can be studied successfully at cryogenic temperatures and by use of Eq. (20) the decay time τ_{av}(300 K) becomes available.

The relation depicted in Fig. 8 shows a series of interesting trends:

- The emission decay time decreases by more than three orders of magnitude with increasing ΔE(ZFS) (note the logarithmic scale). This is induced by an increasing effectivity of SOC between the emitting triplet state and higher lying singlet states (compare Eq. (13)).
- The observed trend is valid for a large number of organo-transition metal compounds even with various central metal ions, such as Ru(II), Rh(III), Pd(II), Re(I), Os(II), Pt(II), or Ir(III).
- According to extensive investigations by Yersin's group [33,34,78,79,86,87,178], it is possible to characterize the emitting triplet states on the basis of the magnitude of ΔE(ZFS). Thus, the compounds grouped on the left hand side of the diagram with ΔE(ZFS) values of less than a few wavenumbers represent states being largely of ^{3}LC ($^3\pi\pi^*$) character. For these emitters, SOC is not very effective and therefore ΔE(ZFS) is small. The radiative decay times can be as long as several milliseconds. According to the spin–orbit coupling routes introduced in Section 4, this situation can be described by weak indirect spin–orbit coupling via configuration interaction (compare Section 4.3 and Fig. 6). On the other hand, the triplet states of compounds with large zero-field splitting, for example being greater than 50 cm^{-1}, are assigned as being mainly of ^{3}MLCT (^{3}dπ^*) character. These states experience efficient direct SOC with other ^{1,3}MLCT states as described in Section 4.2 (compare also Fig. 5). Thus, the radiative rates become larger and the corresponding decay times shorter. For example, for Ir(ppy)$_3$ (**52**) in frozen CH_2Cl_2, a ΔE(ZFS) value of 170 cm^{-1} and a radiative decay time of only 1.6 µs are determined (Section 8, Ref. [40]). Finally, the triplet states of compounds that exhibit ΔE(ZFS) values in the intermediate range of several cm^{-1} up to several ten cm^{-1} may be classified as ^{3}LC ($^3\pi\pi^*$) states with significant ^{3}MLCT admixtures. Accordingly, the radiative decay times are longer than for emitting ^{3}MLCT states and mostly lie in the range of 5–10 µs (compare also Table 2).
- The differently shaded bars displayed in the lower part of Fig. 8 refer to the classification of the emitting triplet states as discussed above. Provided that further basic conditions, such as high ϕ_{PL} values, well suited redox potentials, no overall charge, good processability, etc. are fulfilled, compounds with emitting states of ^{3}LC/^{3}MLCT or ^{3}MLCT character are suited as emitters for OLED applications.
- As discussed in Section 2, the emission decay time should be as short as possible to reduce roll-off effects. This is especially important for lighting applications. Indeed, all OLED triplet emitters with acceptable performance studied so far exhibit zero-field splittings of the emitting triplet term larger than about 8–10 cm^{-1} [79,179]. Especially, the best suited triplet emitters are Ir(III) complexes with zero-field splittings greater than

Table 2
Photophysical data for a series of organo-transition metal compounds. The related chemical structures are summarized in Fig. 9. Detailed explanations are given in the text.

	1 Compound	2 (I → 0)$_{0-0}$ or high energy flank [cm^{-1}]	3 $\Delta E_{I,II}$ [cm^{-1}]	4 $\Delta E_{I,III}$ = ΔE(ZFS) [cm^{-1}]	5 τ_I [μs]	6 τ_{II} [μs]	7 τ_{III} [μs]	8 τ_{av} (300 K) [μs]	9 τ (300 K) [μs]	10 τ (77 K) [μs]	11 λ_{max} (300 K) [nm]	12 λ_{max} (77 K) [nm]	13 Φ_{PL} (300 K)	14 Refs.
1	$[Rh(bpy)_3]^{3+a}$	22,757	0.04^{b} 0.077^{b} **0.116**^{b}		4.5×10^3	1.35×10^3	650	**1.2 × 10³**		$2.2 \times 10^{3\ c}$		483^{c}		[178,190,199,201,203,204]
2	$Pd(qol)_2{}^{d}$	16,090	0.0785^{b} **0.175**^{b}		9.0×10^4	180	80	**166**						[198,205]
3	$Pd(thpy)_2{}^{d}$	18,418	**0.0962**^{b}		1.2×10^3	235	130	**235**		280^{e}		536^{e}		[78,206–208]
4	$Pt(qol)_2{}^{d}$	15,426	$<1^{i}$	**<1**^{i}	60	13	4.5	**9.5**	2.7^{r}	$14^{\ c}$	655^{r}	623^{c}	$< 0.01^{r}$	[205,209,210]
5	$Pt(s2\text{-}thpy)(acac)^{d}$	16,150	$<1^{i}$	**<1**^{i}	27	27	4	**9.3**	7.3	9.4	621	618	0.05	[108,109]
6	$Pt(s1\text{-}thpy)(acac)^{d}$	17,199	$<1^{i}$	**<1**^{i}	103	27	7.6	**16.8**	19^{d} 17^{l}	20	578	582	0.34^{d} 0.35^{l}	[108,109]
7	$Pt(bhq)(dpm)^{d}$	19,693	$<1^{i}$	**<1**^{i}	256	66	16	**37**		122^{g}		493^{g}		[106,143,211]
8	$Ir(ppy)_2(CO)(Cl)^{f}$	≈22,000	$<1^{i}$	**<1**^{i}	300	85	9	**24**		25	460	460		[212]
9	$Re(pbt)(CO)_4{}^{h}$	20,138	$<2^{i}$	**<2**^{i}	670	320	24	**65**	21	98	540	532		[213,214]
10	$[Pt(4,6\text{-}dFppy)(CN)_2]^{-\ f}$	≈21,900	$<2^{p}$	**<2**^{p}	100	31.5	11.5	**23.3**	0.3	21.5	466	459	<0.01	[215]
11	$Pt(thpy)(CO)(Cl)^{d}$	18,012.5	0.05437^{b}	**3.8**^{i}	120	45	35	**51**	12^{j}	$17^{\ j}$	565^{j}	559^{j}	0.30^{j}	[176,202,216]
12	$Pt(thpy)(acac)^{d}$	17,994	4.3^{i}	**4.3**^{i}	156	7.2^{k}		**21**	21^{d} 19^{l}	21	559	556	0.6^{d} 0.5^{l}	[107,109]
13	$Pt(4,6\text{-}dFpthiq)(dpm)^{d}$	21,814	6^{i}	**6**^{i}	95	4.3^{k}		**12.4**	9^{l}	11.3^{l}	460^{l}	460^{l}	0.5^{l}	[217,218]
14	$Pt(ppy)(CO)(Cl)^{d}$	20,916	$<1^{i}$	**6.4**^{i}						28^{m}		476^{m}		[176,219,220]
15	$Pt(4,6\text{-}dFppy)(acac)^{d}$	21,453	8.3^{i}	**8.3**^{i}	85	2.6^{k}		**7.7**	0.2^{g} 5.3^{l}	9.1^{g}	466^{g}	458^{g}	0.02^{g} 0.5^{l}	[86,87,104–106,221]
16	$Pt(dpyb)Cl^{d}$	20,248	6^{i}	**10**^{i}	51.4	1.9	4.5	**3.9**	7.2^{h}	5.8^{g}	491^{h}	486^{g}	0.60^{h}	[147,149,222]
17	$Pt(pbt)(acac)^{n}$	18,840	7^{i}	**10**^{i}	57	10	2.7	**6.2**	$6.0^{\ l}$	$7.0^{\ l}$	539^{l}	532^{l}	0.36^{l}	[106,113]
18	$Pt(ppy)(acac)^{d}$	20,635	8^{i}	**11.5**^{i}	94	17.1	3.2	**8.1**	2.7^{h}	8.0^{h}	485^{h}	481^{h}	0.2^{h}	[106,143,223]
19	$Pt(thpy)_2{}^{d}$	17,156	7^{i}	**16**^{i}	110	3.6			2.2^{e}	12^{e}	578^{e}	570^{e}	0.3^{e}	[78,176,207,224]
20	$Ir(s1\text{-}thpy)_2(acac)^{h}$	17,276	3^{i}	**16**^{i}	128	62	3	**8.8**	5.8^{h} 5.6^{l}	5.2	586	574	0.41^{h} 0.55^{l}	[107,109]
21	$Pt(ppy_2\text{-}tBu_2a)^{d}$	15,930	6^{i}	**17**^{i}	139	3.4	10.8	**7.6**	6.4^{g}	8.0^{g}	625^{g}	600^{g}	0.48^{g}	[172,225]
22	$Pt(dphpy)(CO)^{d}$	19,174.5	<1	**17.5**^{i}	450	15	7	**14.6**		11^{o}	536^{f}	521^{o}		[226,227]
23	$Pt(Me_4\text{-}salen)^{f}$	≈19,300	4^{p}	**20**^{p}	93	38	2	**5.9**	4.7	7.6	550	540	0.27	[180–182,223]
24	$Pt(3\text{-}thpy)_2{}^{d}$	18,020	13^{i}	**22**^{i}	105	2.7	5	**5.3**			553^{h}			[78,228,229]
25	$Ir(btp)2(acac)^{h,v}$	16,396	2.9^{i}	**14.8**^{i}	62	19	3	**7.7**			615			[79,177,179,230,231]
	$Ir(btp)2(acac)^{h,v}$	16,268	2.9^{i}	**25**^{i}	150	58	2	**6.2**	5.8^{g}	6.5^{g}	612^{g}		0.20^{g}	
26	$Ir(ppy)(ppy\text{-}NPH_2)_2{}^{f}$	$≈19,500^{o}$	6^{p}	**23**^{p}	163	20	2	**5.7**	3.3^{g}	8.3^{o}	526^{g}	519^{o}		[128]
27	$Ir(ppy\text{-}NPH_2)_3{}^{f}$	$≈19,500^{o}$	6^{p}	**26**^{p}	177	15	1.4	**4.1**	4.3^{g}	6.4^{o}	527^{g}	518^{o}		[128]
28	$Ir(ppy)_2(ppy\text{-}NPH_2)^{f}$	$≈19,600^{o}$	6^{p}	**27**^{p}	188	19	1.8	**5.2**	2.4^{g}	7^{o}	526^{g}	515^{o}		[128]
29	$Pt(ph\text{-}salen)^{f}$	≈16,900	3^{p}	**28**^{p}	54	28	2	**5.8**	4.6	7.0	625	615	0.26	[181,223]
30	$Pt(tBu_2\text{-}ppy_2\text{-}fluoren)^{d}$	19,560	9.5^{i}	**30**^{i}	80	2	3.9	**4**	6.6^{g}	5.7^{g}	521^{g}	507^{g}	0.90^{g}	[172,225]
31	$Pt(ppy)_2{}^{d}$	19,571	6.9^{i}	**32**^{i}	70	2.4				4.1^{g}		500^{g}	<0.01 0.01^{l}	[172,176,228,232]
32	$Pt(bhq)_2{}^{u}$	20,192	10^{i}	**33**^{i}	48	2.9	3.5	**4.7**		6.5^{e}		492^{e}		[211,224]
33	$Ir(thpy)_2(acac)^{h}$	17,538	3.5^{i}	**34**^{i}	113	35	1.5	**4.7**	6.4 5.8^{l}	6.1	567	560	0.38^{h} 0.67^{l}	[107,230]

34	Pt(ppy$_2$-C$_2$)[d]	19,474	6[i]	**36**[i]	47	2.4	5	**4.7**		5.7[g]		507[g]		[172,225]
35	Pt(ppy$_2$-fluoren)[d]	19,420	11[i]	**38**[i]	73	2	4.2	**4.1**	6.0[g]	5.1[g]	516[g]	506[g]	0.91[g]	[172,225]
36	Ir(4,6-dFppy)$_2$(pic)[f]	≈22,000	11–10[p,q]	**41–66**[p,q]	71–85[q]	11–27[q]	0.8–0.5[q]	**2.5–1.8**[q]	1.8		471		0.84	[102,233,234]
	Ir(4,6-dFppy)$_2$(pic)[h]	21,738	9[i]	**76**[i]	47	21	0.3	**1.1**	1.9		470		0.83	
37	Ir(piq)$_3$[h]	≈17,000	10–8[p,q]	**43–57**[p,q]	51–61[q]	3.2–7.8[q]	0.5–0.4[q]	**1.4–1.3**[q]	1.3	2.4	629	615	0.57	[235–237]
	Ir(piq)$_3$[l]	≈16,800	11[p]	**64**[p]	57	5.3	0.42	**1.4**	1.25[g]	2.1[r]	624[g]	603[r]	0.45[g]	
38	[Ru(bpy)$_3$]$^{2+}$[a]	17,684	8.7[i]	**61**[i]	230	8	0.9	**2.8**	0.93[r]	5.0[r]	628[o]	582[o]	0.062[s]	[190–195,238]
39	[Os(phen)$_2$(dppene)]$^{2+}$[c]	≈18,500	18[p]	**64**[p]	108	15	1.1	**3.6**	1.8[t]	5.7	614[t]	566	0.2[t]	[110,167,169,239,240]
40	Ir(piq)$_2$(ppy)[l]	≈16,800	9[p]	**65**[p]	60	6.4	0.44	**1.5**	1.39[g]		631[g]		0.37[g]	[236]
41	Ir(biqa)$_3$[g]	≈21,800	14[p]	**78**[p]	107	5.6	0.36	**1.25**	0.19	2.3	471	464	0.10[g] 0.50[l]	[172,225]
42	[Os(phen)$_2$(dppe)]$^{2+}$[c]	≈18,200	19[p]	**74**[p]	107	12	0.9	**3**	1.6[t]	6.1	618[t]	575	0.13[t]	[110,169]
43	[Os(phen)$_2$(DPEphos)]$^{2+}$[c]	≈17,800	16[q]	**84**[q]	104	14	0.9	**3.2**	1.4[h]	7.4	648[h]	590	0.10[h]	[110]
44	[Os(dpphen)$_2$(dpae)]$^{2+}$[c]	≈17,100	19[q]	**94**[q]	92	9	0.7	**2.5**	1.5[t]	5.3	648[t]	616	0.12[t]	[110,169]
45	Ir(piq)$_2$(acac)[f]	≈16,600	9[p]	**96**[p]	47	8	0.3	**1.2**	1.1	2.4	632	626	0.2[h]	[231,235,241]
46	Ir(pbt)$_2$(acac)[d]	≈18,200	6[p]	**103**[p]	82	25	0.4	**1.6**	1.8[g]	4.4[g]	557[g]	549[g]	0.26[g]	[110–112]
47	Ir(4,6-dFppy)$_2$(acac)[f]	≈21,500	15–10[p,q]	**80–125**[p,q]	68	9–19[q]	0.5–0.2[q]	**1.8–0.9**[q]	1.2		486		0.67	[87,102,103]
	Ir(4,6-dFppy)$_2$(acac)[h]	21,025	16[i]	**109**[i]	44	9	0.4	**1.6**	1.0		484		0.64	
48	Ir(piq)(ppy)$_2$[l]	≈17,000	16[p]	**107**[p]	64	10.5	0.36	**1.4**	1.38[g]		631[g]		0.40[g]	[236]
49	[Os(phen)$_2$(dpae)]$^{2+}$[c]	≈17,500	21[p]	**113**[p]	100	10	0.7	**2.7**	1.2[t]	7.9	631[t]	592	0.12[t]	[110,169]
50	[Os(phen)$_2$(dppm)]$^{2+}$[c]	≈18,000	16[p]	**122**[p]	95	13	0.6	**2.5**	1.1[t]	8.3	627[t]	584	0.15[t]	[110,169]
51	Ir(dm-2-piq)$_2$(acac)[h]	≈16,900	9.5–10[p,q]	**150–160**[p,q]	80–124[q]	6.5–8.6[q]	0.33–0.44[q]	**1.5–2.0**	1.7	8.0	624	602	0.80[l]	[242]
52	Ir(ppy)$_3$[f]	≈20,000	14–13[p,q]	**85–150**[p,q]	135–155[q]	10–14[q]	0.6 – 0.25[q]	**2.2–1.2**[q]	1.6[g]	4.0[g]	508[g]	491[g]	0.97[g]	[38,40,79,175]
	Ir(ppy)$_3$[l]	≈20,000	12.4–12[p,r]	**114–135**[p,q]	151–158[q]	13–18[q]	0.34–0.33[q]	**1.4–1.5**[q]	1.4	5	508	503	0.96	
	Ir(ppy)$_3$[h]	19,693	19[i]	**170**[i]	116	6.4	0.2	**1**	1.6		519	514	0.90	

---

[a] Measured in [Zn(bpy)$_3$](ClO$_4$)$_2$.

[b] From ODMR measurements.

[c] Measured in ethanol.

[d] Measured in *n*-octane.

[e] Measured in butyronitrile.

[f] Measured in THF.

[g] Measured in 2-MeTHF.

[h] Measured in CH$_2$Cl$_2$.

[i] From highly resolved spectra.

[j] Measured in DMF.

[k] Combined decay time for the substates II and III. Individual decay times cannot be given since the energy splitting between these states is less than 1 cm^{-1}.

[l] Measured in PMMA.

[m] Measured in toluene.

[n] Measured in *n*-hexane.

[o] Measured in ethanol/methanol.

[p] From a fitting procedure (compare Section 8.5).

[q] Inhomogeneous distribution.

[r] Measured in toluene/ethanol/methanol.

[s] Measured in acetonitrile.

[t] Measured in chloroform.

[u] Measured in n-decane.

[v] Different site.

about 50 cm^{-1}. Examples are: Ir(piq)$_3$ (**37**): 64 cm^{-1}; Ir(4,6-dFppy)$_2$(pic) (**36**): 76 cm^{-1}; Ir(dm-2-piq)$_2$(acac) (**51**): 100 cm^{-1}; Ir(ppy)$_3$ (**52**): 170 cm^{-1}. Recently it has been shown that Pt(II) complexes, lying in the intermediate range, also represent attractive OLED emitters [7,180–189].

- Interestingly, all compounds with ΔE(ZFS) values greater than about 50 cm^{-1} have (quasi-) octahedrally coordinated central metal ions. In contrast, the largest ΔE(ZFS) value observed so far for a Pt(II) complex with a (quasi-) square-planar coordination amounts only to 46 cm^{-1} [143]. As described in Section 4.5, this behavior is a consequence of relatively large energy separations between mixing MLCT states in square-planar compounds. This leads to less effective SOCs than in compounds with octahedral coordination. A further example is also very illustrative. The lowest triplet state of the quasi-octahedral [Ru(bpy)$_3$]$^{2+}$ (**38**) shows a value of ΔE(ZFS) = 61 cm^{-1} [190–195], which is significantly larger than found for any Pt(II) complex, although the SOC constant of Ru(II) is by more than a factor of 4 smaller than that of Pt(II) [196].
- One specific trend, which is clearly displayed in Fig. 8, merits special comments. With increasing ΔE(ZFS) and thus increasing impact of SOC, the emission decay time τ_{av} (300 K) does not seem to decrease to significantly lower values than about 1 μs. The plot appears to exhibit an asymptotic decrease. The reason for this behavior is easily explained, if one takes into account that τ_{av} (300 K), approximately representing the radiative emission decay time at ambient temperature (see above), is determined by a Boltzmann distribution as displayed in Eq. (20). At ambient temperature, all three triplet substates are responsible for the emission decay time. In particular, although the highest triplet substate III mostly exhibits by far the shortest (radiative) decay time, at least for Ir(III) complexes with large ΔE(ZFS) values, substate III contributes only according to its Boltzmann-governed population (compare also Section 8.6) This can be illustrated by a simple approximation. Let us assume that the individual emission decay time decreases in the order $\tau_{III} \ll \tau_{II}$, τ_I and that $\Delta E_{I,II} \ll \Delta E_{I,III}$, which is frequently found for MLCT emitters with large zero-field splittings (e.g. compare Table 2 or Figs. 13 and 16). Under these conditions and in a high-temperature limit, for example at T = 300 K, Eq. (20) simplifies to

$$\tau_{av} \approx 2 \cdot \tau_{III} \cdot \exp\left(\frac{\Delta E(\mathrm{ZFS})}{k_B T}\right) \tag{21}$$

This crude approximation allows us to describe qualitatively the behavior shown in Fig. 8. An increase of SOC, which usually leads to a shortening of the emission decay time τ_{III}, will normally also induce an increase of the splittings between the triplet substates. The resulting larger ΔE(ZFS) will prevent further significant reduction of a compound's (radiative) emission decay time.

For completeness, it is remarked that the systematics presented in Fig. 8 is only valid for the types of organometallic compounds as discussed in the context of this section or as summarized in Table 2. It is not excluded that much shorter radiative decay times, being a target for bright and efficient OLED lighting, might be attainable with other electronic structures. In this respect, we proposed to investigate compounds with low-lying and strongly emitting singlet states and introduced the singlet harvesting effect (compare Sections 2 and 9).

Table 2 summarizes data for a number of organo-transition metal compounds of the second and third period of transition metals. These compounds exhibit emitting triplet states of ^{3}LC, ^{3}MLCT, and mixed ^{3}LC/^{3}MLCT character, respectively. Most data given in the table have been determined by cooling the samples to cryogenic temperatures, since at ambient temperature the detailed

Table 3
Radiative and nonradiative rates of the three individual triplet substates of the emitting T$_1$ state, emission decay times, and emission quantum yields at T = 77 K and 300 K for selected organo-transition metal compounds. Further photophysical data are found in Table 2. The chemical structures of the compounds are summarized in Fig. 9.

	1 Compound	**2** $\Delta E_{I,II}$ [cm^{-1}]	**3** $\Delta E_{I,III} = \Delta E$(ZFS) [cm^{-1}]	**4** $k_I{}^r$ ($k_I{}^{nr}$) [s^{-1}]	**5** $k_{II}{}^r$ ($k_{II}{}^{nr}$) [s^{-1}]	**6** $k_{III}{}^r$ ($k_{III}{}^{nr}$) [s^{-1}]	**7** $k_{av}{}^r$ ($\tau_{av}{}^r$) (300 K)	**8** τ (77 K) [μs]	**9** τ (300 K) [μs]	**10** Φ_{PL} (77 K)	**11** Φ_{PL} (300 K)	**12** Refs.
12	Pt(thpy)(acac)^{a}	4.3^{b}	**4.3**^{b}	^{c}	^{c}	^{c}	2.9×10^4 s$^{-1\,d}$ (**35 μs**)	21	21	0.60^{g}	0.60	[107,109]
13	Pt(4,6-dFpthiq)(dpm)^{e}	6^{f}	**6**^{f}	^{c}	^{c}	^{c}	$7.1 \times 10^{4\ -1\ d}$ (**14 μs**)	11.3	≈9	0.80	0.50	[172,217,218]
41	Ir(biqa)$_3$^{g}	14^{f}	**78**^{f}	$8.8 \times 10^{3\,i}$ (5×10^2)	$1.75 \times 10^{5\,i}$ (5×10^3)	$2.6 \times 10^{6\,i}$ (1×10^5)	7.5×10^5 s^{-1}(**1.3 μs**)	2.3	0.19	0.97^{g}	0.10^{h}/0.50^{e}	[172,225]
52	Ir(ppy)$_3$^{e}	12.2^{f}	**125**^{f}	$5.7 \times 10^{3\,i}$ (8×10^2)	$5.8 \times 10^{4\,i}$ (7×10^3)	$2.9 \times 10^{6\,i}$ (1×10^5)	6.9×10^5 s^{-1}(**1.45 μs**)	5.2	1.4	0.97^{e}	0.96^{e}	[40,172]

[a] Measured in n-octane.

[b] From highly resolved spectra.

[c] The individual radiative and nonradiative rate constants of the triplet substates could not be determined.

[d] Determined from emission decay time and quantum yield measurements at ambient temperature, respectively.

[e] Measured in PMMA.

[f] From a fitting procedure (compare Section 8.5).

[g] Measured in 2-MeTHF.

[h] The low quantum yield at T = 300 K in 2-MeTHF is a consequence of emission quenching by a thermally populated dd* state with an activation energy of about 2350 cm^{-1}. In a PMMA host, the quenching state is destabilized and the quantum yield increases to 0.50.

[i] The decay rates for the individual triplet substates are determined as discussed in Section 8.6.

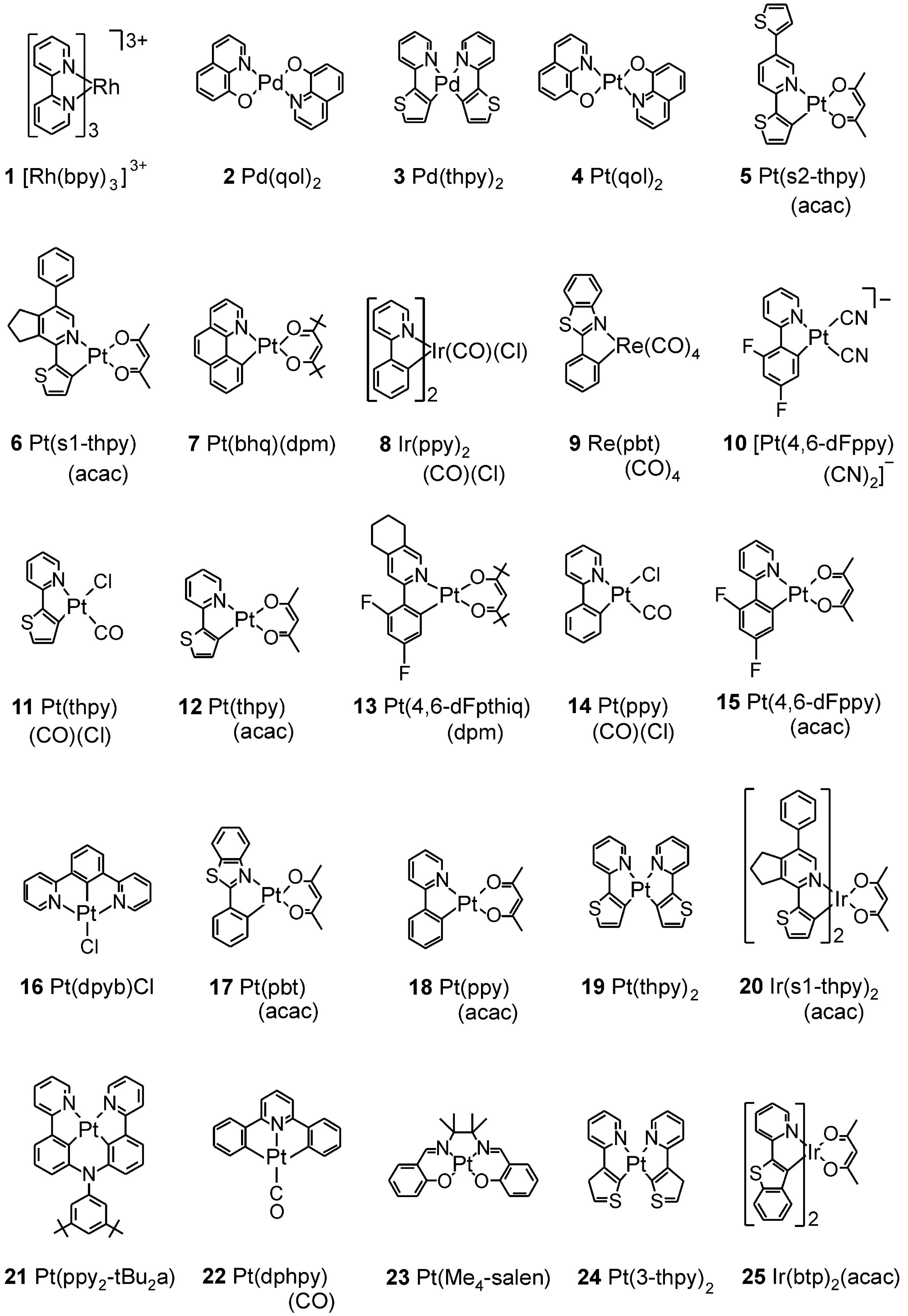

1 [Rh(bpy)$_3$]$^{3+}$

2 Pd(qol)$_2$

3 Pd(thpy)$_2$

4 Pt(qol)$_2$

5 Pt(s2-thpy)(acac)

6 Pt(s1-thpy)(acac)

7 Pt(bhq)(dpm)

8 Ir(ppy)$_2$(CO)(Cl)

9 Re(pbt)(CO)$_4$

10 [Pt(4,6-dFppy)(CN)$_2$]$^-$

11 Pt(thpy)(CO)(Cl)

12 Pt(thpy)(acac)

13 Pt(4,6-dFpthiq)(dpm)

14 Pt(ppy)(CO)(Cl)

15 Pt(4,6-dFppy)(acac)

16 Pt(dpyb)Cl

17 Pt(pbt)(acac)

18 Pt(ppy)(acac)

19 Pt(thpy)$_2$

20 Ir(s1-thpy)$_2$(acac)

21 Pt(ppy$_2$-tBu$_2$a)

22 Pt(dphpy)(CO)

23 Pt(Me$_4$-salen)

24 Pt(3-thpy)$_2$

25 Ir(btp)$_2$(acac)

Fig. 9. Chemical structures of compounds discussed. Photophysical data are summarized in Tables 2 and 3.

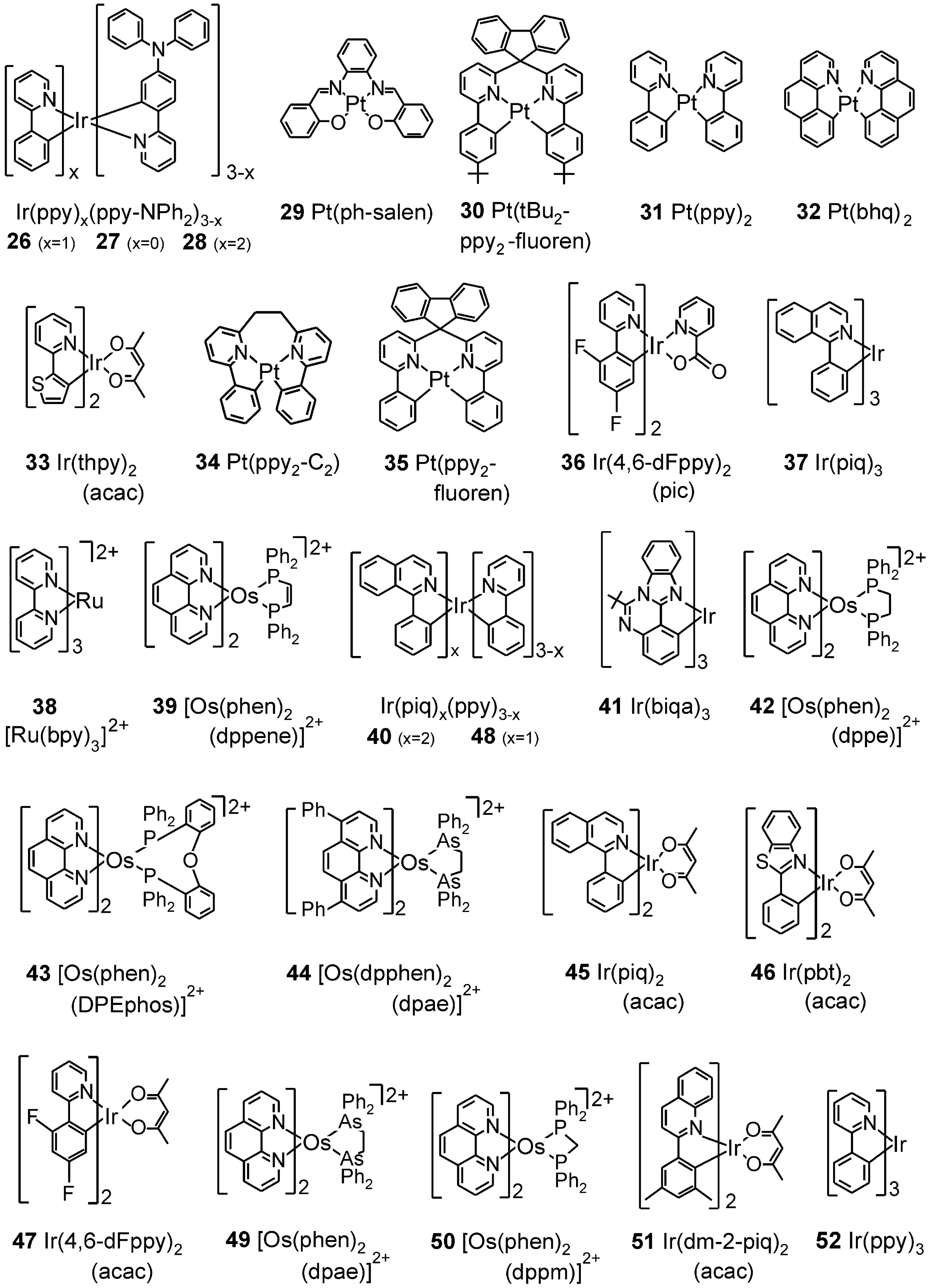

Fig. 9. (*Continued*).

information is smeared out mainly because of homogenous broadening effects [197]. Subsequently, some background information to Table 2 is given.

Column 1 displays the names (acronyms) of the compounds. The corresponding molecular structures are summarized in Fig. 9. The properties of most compounds show a certain dependence on the environment or matrix in which the complexes were studied. Therefore, the host is always mentioned and for several emitters, data are given for different host matrices. Compare, for example, the compounds $Ir(piq)_3$ (**37**) and $Ir(ppy)_3$ (**52**).

Column 2 reproduces the 0–0 energy position of the lowest triplet substate I. For many compounds given in Table 2, this transition is resolved at low temperatures, e.g. at $T = 1.2$ K. On the other hand, for compounds for which such a high resolution could not be obtained, the corresponding energy position is estimated from the high-energy flank of the low-temperature emission spectrum.

Columns 3 and 4 display the zero-field splitting (ZFS) values $\Delta E_{\mathrm{I,II}}$ and $\Delta E_{\mathrm{I,III}}$ of the lowest triplet state T_1. These data represent the energy separations between substate I and the higher lying substates II and III, respectively. In particular, the total zero-field splitting ΔE(ZFS) is given by $\Delta E_{\mathrm{I,III}}$. Only compounds are summarized in Table 2 for which the corresponding information is available. The data are determined either by direct observation of the splitting pattern or indirectly from an analysis of the temperature-dependent emission decay time by applying Eq. (20) (compare Sections 7 and 8 and the Figs. 12 and 17). In a few cases, in which the ZFS energies are smaller than 1 cm^{-1}, the information results from ODMR (optically detected magnetic resonance) measurements [198–202].

The emission decay times τ_{I}, τ_{II}, and τ_{III}, as shown in columns 5–7, are determined from temperature dependent plots of the thermalized emission decay time according to Eq. (20).

Column 8 gives the emission decay time τ_{av} (300 K) calculated by use of the three individual emission decay times of the T_1 substates (τ_{I}, τ_{II}, and τ_{III}) and of the zero-field splitting values $\Delta E_{\mathrm{I,II}}$ and $\Delta E_{\mathrm{I,III}}$ according to Eq. (20) for a temperature of 300 K. The measured emission decay time at 300 K, if obtainable, is displayed in column 9 and the decay time at 77 K in column 10. Several compounds do not emit at ambient temperature, such as $[\mathrm{Rh(bpy)_3}]^{3+}$ (**1**), $\mathrm{Pd(qol)_2}$ (**2**), and $\mathrm{Pd(thpy)_2}$ (**3**). Particularly in these situations the data given in column 8 are helpful. Data from the columns 4 and 8 (printed in bold style) are used for the plot shown in Fig. 8.

In columns 11 and 12, we summarize the emission maxima at 300 K and 77 K, respectively.

Column 13 gives values of emission quantum yields at ambient temperature. Only reliable values or data which have been remeasured recently by use of techniques as described in Ref. [40] are included in the table.

Finally, column 14 contains references in which data for the compounds are given.

Table 3 reproduces additional data for four selected compounds. Data for these are also summarized in Table 2. However, for these materials, additionally the emission decay times and emission quantum yields were measured over the extended temperature range of 1.2 K ≤ T ≤ 300 K. Thus, the individual radiative and nonradiative decay rates of the T_1 substates (columns 4–6) could be determined by the procedure as described in Section 8 and Refs. [40,172] for the example of $\mathrm{Ir(ppy)_3}$. The data in columns 3 ($\Delta E_{\mathrm{I,III}}$) and 7 ($\tau^r_{\mathrm{av}}$ (300 K)) (printed in bold style) are used for the plot shown in Fig. 8 (open symbols). These data are particularly valuable, since τ^r_{av} (300 K) represents the averaged *radiative* decay time of the three triplet substates at ambient temperature. Since these values fit perfectly to the plot of Fig. 8, the general validity of this trend is set on a firmer basis.

7. Case study $\mathrm{Ir(dm\text{-}2\text{-}piq)_2(acac)}$ – Red light emitter

Red light emitting organo-transition metal compounds with high emission quantum yields are relatively rare, since for materials with small energy gaps between the emitting state and the ground state nonradiative decay, governed by the "energy gap law" (Section 5.2.2), is frequently more effective than radiative decay (Section 4). In the present section, we want to discuss properties of the very efficient organo-metallic red light emitter $\mathrm{Ir(dm\text{-}2\text{-}piq)_2(acac)}$ (**51**).

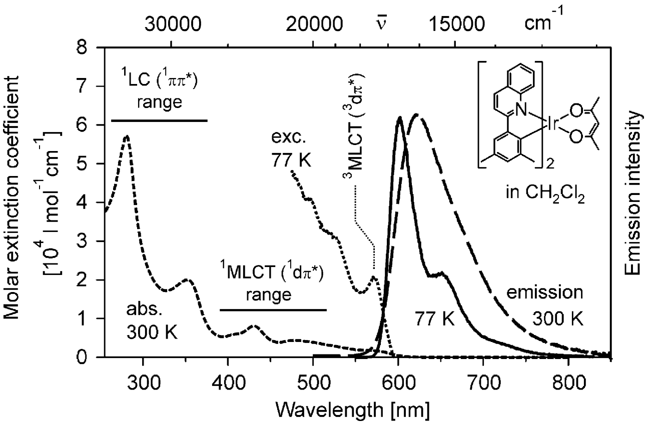

Fig. 10. Absorption, excitation and emission spectra of $\mathrm{Ir(dm\text{-}2\text{-}piq)_2(acac)}$ (**51**) in $\mathrm{CH_2Cl_2}$ measured at ambient temperature and at 77 K, respectively. The inset shows the structure of the compound.

7.1. Spectroscopic introduction

Fig. 10 shows the absorption, excitation, and emission spectra of $\mathrm{Ir(dm\text{-}2\text{-}piq)_2(acac)}$ measured in $\mathrm{CH_2Cl_2}$ at 300 K and 77 K. The observed transitions are assigned similarly as for related Ir(III) compounds like $\mathrm{Ir(ppy)_3}$ (**52**) (see Section 8.1) and $\mathrm{Ir(btp)_2(acac)}$ (**25**) [179] (compare also [243]). The strong absorptions in the wavelength region below ≈375 nm can be assigned to spin-allowed π–π^* transitions corresponding to ^{1}LC states centered at the cyclometallating (2-(dimethylphenyl)-isoquinoline) ligands. Maxima are observed at 280 nm and 352 nm. Absorption bands in the range between ≈390 nm and ≈515 nm are assigned to overlapping spin allowed d–π^* transitions (^{1}MLCT states) with maxima at 405 nm (shoulder), 430 nm and 479 nm. The weaker absorption tail at wavelengths above ≈520 nm involves mainly ^{3}MLCT states. These assignments should not be taken too strictly, since the LC and MLCT states are usually mixed. The broad and unstructured deep-red emission at $T = 300$ K has its maximum at 623 nm. Cooling the sample to $T = 77$ K leads to a slightly more structured emission. The dominating emission peak at that temperature is located at 602 nm. This band overlaps with the peak of lowest energy at 573 nm observed in the 77 K excitation spectrum. Thus, these bands are assigned to the electronic $S_0 \leftrightarrow T_1$ transitions which exhibit a Stokes shift of about 800 cm^{-1}. The weaker emission maximum at 652 nm, being separated by about 1270 cm^{-1} from the main maximum, is assigned to overlapping vibrational satellites of ground state modes.

At ambient temperature, $\mathrm{Ir(dm\text{-}2\text{-}piq)_2(acac)}$ (**51**) is highly emissive. The photoluminescence quantum yield in degassed $\mathrm{CH_2Cl_2}$ solution amounts to $\phi_{\mathrm{PL}} \approx 50\%$ and in PMMA under nitrogen atmosphere to $\phi_{\mathrm{PL}} \approx 80\%$. In $\mathrm{CH_2Cl_2}$ solution, the emission decays with $\tau = 1.7$ μs and in a PMMA film with $\tau = 1.6$ μs. Accordingly, for the compound doped into PMMA, the radiative and nonradiative decay rates are $k^r = 5 \times 10^5\ \mathrm{s}^{-1}$ and $k^{nr} = 1.3 \times 10^5\ \mathrm{s}^{-1}$.

7.2. Temperature dependence of the emission

Fig. 11 shows emission spectra of $\mathrm{Ir(dm\text{-}2\text{-}piq)_2(acac)}$ in frozen $\mathrm{CH_2Cl_2}$ at different temperatures. These spectra exhibit a similar temperature dependence as found for $\mathrm{Ir(ppy)_3}$ (see Section 8 and Refs. [40,175]). At 1.2 K, the emission results mainly from the lowest triplet substate I and has its maximum at 612 nm. Since the decay time at 1.2 K is very long ($\tau_{\mathrm{I}} = 124$ μs, see below), it can be concluded that the transition I → 0 is largely forbidden. Thus, the emission of substate I is mainly induced by processes of spin-vibronic coupling (Herzberg–Teller (HT) coupling) with higher lying sin-

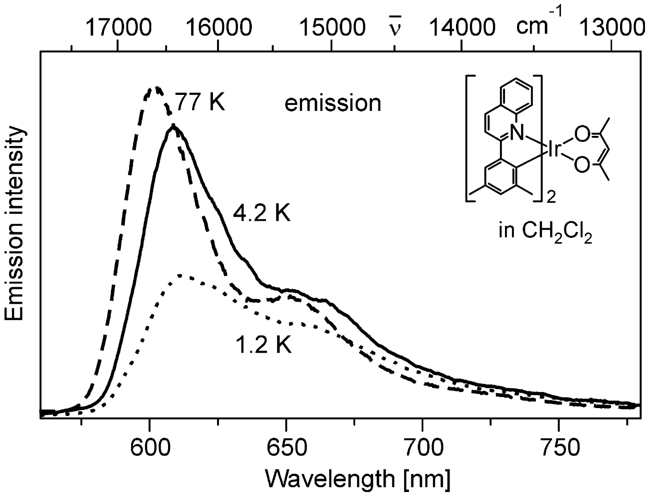

Fig. 11. Emission spectra of Ir(dm-2-piq)$_2$(acac) **(51)** in CH$_2$Cl$_2$ ($c \approx 10^{-5}$ mol/l) recorded at different temperatures. The spectra measured at 1.2 K and 4.2 K were excited at λ_{exc} = 355 nm, the one at 77 K at λ_{exc} = 475 nm.

glet states. These processes induce emission intensity to specific vibrational satellites, but not to the electronic 0–0 transition [78,79,175,244,245]. However, the individual vibrational satellite lines are smeared out because of the inhomogenous distribution of the emitter complex in the matrix and because of (homogeneous) electron–phonon coupling [79,197]. With increasing temperature, the higher lying T_1 substates II and III are thermally populated. Since the electronic transitions from these triplet substates to the ground state are significantly more allowed, the corresponding emission spectra are dominated by (homogeneously and imhomogenously broadened) electronic transitions and Franck–Condon activated vibrational satellites [78,175]. As a consequence, the emission is slightly blue shifted. At 77 K, for example, its maximum is found at 602 nm. It is remarked that a similar behavior has been observed for [Ru(bpy)$_3$]$^{2+}$ already a long time ago [190,192,246–248].

7.3. Emission decay times of the individual triplet substates and energy level diagram

The emission decay curve of Ir(dm-2-piq)$_2$(acac) in polycrystalline CH$_2$Cl$_2$ measured at T = 1.2 K is displayed in the inset of Fig. 12. At T = 1.2 K, two decay components are observed. The long component of 124 μs is ascribed to the deactivation time of the lowest triplet substate I to the singlet ground state (τ_I), while the short component of about 300 ns is assigned to a relaxation (spin-lattice relaxation, SLR) from substate II to substate I according to the direct process of SLR [78,176]. With temperature increase, the SLR processes become faster. For example, at T = 20 K the fast decay component is no longer observable.

As described in Sections 6 and 8.4, emission decay data determined in a larger temperature range allow us also to deduce the individual emission decay times τ_{II} and τ_{III} of the two higher lying triplet substates as well as the zero-field splitting parameters $\Delta E_{I,II}$ and $\Delta E_{I,III}$. This is possible by fitting Eq. (20) to the (thermalized) emission decay times measured at various temperatures. The resulting fit parameters are given in Fig. 12 and are summarized in the energy level diagram depicted in Fig. 13.

For completeness, it is remarked that the emission decay curves of Ir(dm-2-piq)$_2$(acac) in the temperature range 1.2 K ≤ T ≤ 116 K are not strictly monoexponential. Besides SLR features at low temperatures (see inset of Fig. 12), this behavior is caused by inhomogeneity effects. By applying a relatively coarse approximation, a short and a long decay component can be determined from each non-monoexponential decay curve. Using these data for the fitting procedure, one obtains ranges of zero-field splitting energies and of individual emission decay times. This approach has already successfully been carried out for other Ir(III) compounds [40,102,233] (compare also Section 8.5). For Ir(dm-2-piq)$_2$(acac) **(51)** in CH$_2$Cl$_2$, the following ranges are found: 80 μs ≤ τ_I ≤ 124 μs, 6.5 μs ≤ τ_{II} ≤ 8.6 μs, 330 ns ≤ τ_{III} ≤ 440 ns, 9.5 cm^{-1} ≤ $\Delta E_{I,II}$ ≤ 10 cm^{-1}, 150 cm^{-1} ≤ $\Delta E_{I,III}$ ≤ 160 cm^{-1}. Although this spread of parameters is not very distinct as compared to Ir(ppy)$_3$ **(52)** [40] and Ir(4,6-dFppy)$_2$(pic) **(36)** [233], the dependence of photophysical properties on the individual host–environment in the same matrix as well as in different matrices [102] seems to be specifically pronounced for Ir(III) compounds. For further discussions and explanations see Section 8.5 and Refs. [40,102,233].

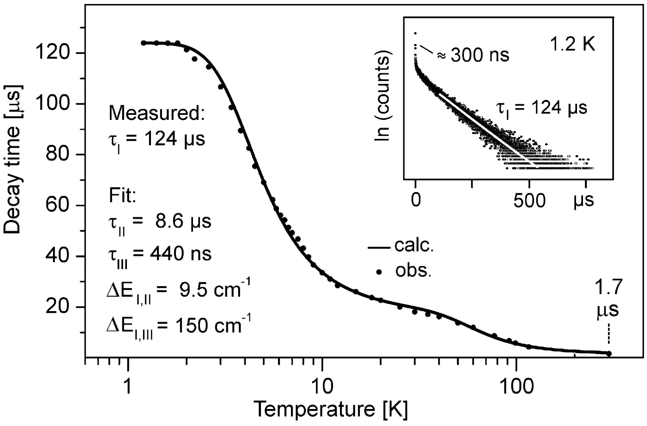

Fig. 12. Temperature dependence of the thermalized emission decay time of Ir(dm-2-piq)$_2$(acac) **(51)** in CH$_2$Cl$_2$ ($c \approx 10^{-5}$ mol/l) recorded after pulsed UV excitation at λ_{exc} = 355 nm and detection at λ_{det} = 608 nm. The inset shows the emission decay curve measured at T = 1.2 K. The decay time of 1.7 μs at 300 K was measured in deaerated CH$_2$Cl$_2$ solution. The individual decay times τ_{II} and τ_{III} for the T$_1$ substates II and III and the zero-field splitting energies $\Delta E_{I,II}$ and $\Delta E_{I,III}$ result from a fit of Eq. (20) to the measured data.

In conclusion, the emitting T$_1$ state of Ir(dm-2-piq)$_2$(acac) **(51)** can be assigned to be largely of ^{3}MLCT character. This is displayed in the large total zero-field splitting of ΔE(ZFS) = 150 cm^{-1} (compare Section 6). The amount of this splitting shows that spin–orbit coupling to higher lying ^{1,3}MLCT states is very effective. This manifests itself also in the relatively large value of the (averaged) radiative decay rate at ambient temperature of $k^r = 5 \times 10^5$ s^{-1}. This value

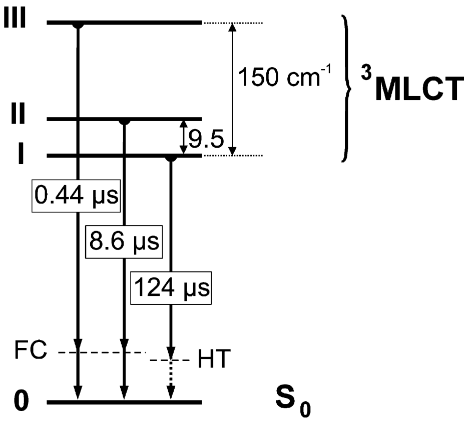

Fig. 13. Energy level diagram for the emitting triplet state of Ir(dm-2-piq)$_2$(acac) **(51)** in CH$_2$Cl$_2$ ($c \approx 10^{-5}$ mol/l). The decay time of substate I was determined directly at T = 1.2 K, while the other data result from a fit of Eq. (20) as displayed in Fig. 12. The levels depicted as HT and FC symbolize the involvements of Franck–Condon (FC) and Herzberg–Teller (HT) active vibrational modes, respectively.

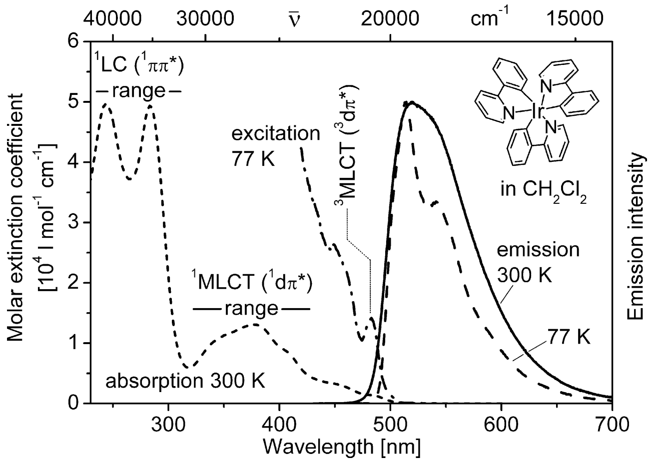

Fig. 14. Emission, absorption, and excitation spectra of Ir(ppy)$_3$ (**52**) in CH$_2$Cl$_2$ measured at ambient temperature and 77 K, respectively.
Adapted from Ref. [40].

compares to the one found for Ir(ppy)$_3$ with $k^r = 6.9 \times 10^5\ \text{s}^{-1}$ (see Section 8). Such large values combined with relatively low non-radiative rates and emission decay times at ambient temperature being distinctly below 2 μs make these complexes highly attractive for applications as emitters in OLEDs.

8. Case study Ir(ppy)$_3$ – Green light emitter

Ir(ppy)$_3$ **(52)** is one of the most famous emitters for OLED applications [39,67–69,74,75,249–251]. It represents the leading example for the success of the triplet harvesting effect (compare Section 2). In this section, we want to introduce to photo-physical properties of this emitter, in particular, focusing on the lowest triplet state and its emission features.

8.1. Spectroscopic introduction

Fig. 14 shows absorption, excitation, and emission spectra of Ir(ppy)$_3$ **(52)** in CH$_2$Cl$_2$ measured at ambient temperature and at 77 K. The absorption bands below 300 nm are related to spin-allowed π–π* transitions (corresponding to ^{1}LC states) of the cyclometallating ppy ligands. The broad and unresolved absorption band at lower energy, peaking at 376 nm, is assigned to overlapping spin allowed d–π* transitions (corresponding to ^{1}MLCT states), whereas absorptions between about 430 and 500 nm involve ^{3}MLCT states [40]. The classifications as ^{1}LC, ^{1}MLCT, or ^{3}MLCT states should only be taken as guidelines, since mixing between the different states by configuration interaction and/or spin–orbit coupling can be significant, in particular, due to the high density of states in the corresponding ranges (compare Section 3). The emission at ambient temperature is broad and unresolved and shows a maximum at 519 nm. The photoluminescence quantum yield of Ir(ppy)$_3$ in degassed CH$_2$Cl$_2$ solution amounts to $\phi_{PL} = 90\%$ and the emission decay time is $\tau = 1.6$ μs. In a PMMA host, values of $\phi_{PL} = 96\%$ and $\tau = 1.4$ μs are found. Thus, the radiative and the nonradiative rate at $T = 300$ K, referring to the combined emissions from the three triplet substates, amount to $k^r = 6.9 \times 10^5\ \text{s}^{-1}$ and $k^{nr} = 3 \times 10^4\ \text{s}^{-1}$, respectively. Cooling to 77 K results in a slightly structured spectrum with a dominating peak at 514 nm and a (vibrationally induced) satellite peak at 541 nm. The excitation spectrum at 77 K overlaps with the emission spectrum in the range of the transitions between the electronic singlet ground state S$_0$ and the emitting triplet state T$_1$, representing a ^{3}MLCT state. The Stokes shift at 77 K between the corresponding bands amounts to ≈600 cm^{-1}, which is ascribed to the involvement of low-energy vibrational/phonon modes [40].

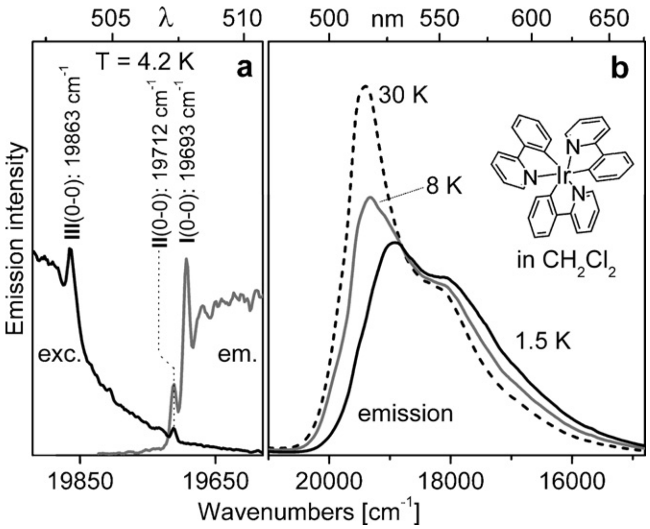

Fig. 15. Excitation and emission spectra of Ir(ppy)$_3$ (**52**) in CH$_2$Cl$_2$ ($c \approx 2 \times 10^{-5}$ mol/L). (b) The usually observed broad emission spectra at selected temperatures. (a) Highly resolved spectra in the range of the electronic 0–0 transitions on an enlarged scale (excitation spectrum: $\bar{\nu}_{\text{det}} = 19,000\ \text{cm}^{-1}$, emission spectrum: $\bar{\nu}_{\text{exc}} = 19,863\ \text{cm}^{-1}$). Three narrow lines can be observed. They represent the 0–0 transitions between the three triplet substates I, II, and III of the emitting ^{3}MLCT term and the ground state S$_0$.
Adapted from Ref. [40].

8.2. Highly resolved spectra and energy level diagram for the triplet state of Ir(ppy)$_3$ in CH$_2$Cl$_2$

Investigations at cryogenic temperatures of Ir(ppy)$_3$ dissolved (doped) in polycrystalline CH$_2$Cl$_2$ show weak, but well resolved electronic 0–0 transitions at the high energy side of the broad emission band (Fig. 15a). These spectra can be obtained under selective excitation (see below). Also the excitation spectrum reveals well resolved 0–0 transitions. Thus, the combined studies of emission and excitation spectra allow us to identify three sharp electronic origins, which are assigned to the three substates I, II, and III of the triplet T$_1$. At $T \leq 3$ K, only substate I emits. The electronic transition I → 0 lies at 19,693 cm^{-1} (507.79 nm). This transition is only very weakly allowed. For example, the decay time of substate I is as long as $\tau_I = 116$ μs (see below). Thus, the corresponding excitation peak could not be detected. With temperature increase, for example to $T = 4.2$ K, a further sharp line grows in at 19,712 cm^{-1} (507.31 nm) in the emission spectrum, lying 19 cm^{-1} higher in energy than the line corresponding to origin I (Fig. 15a). This line is assigned to the 0–0 transition between substate II and the singlet electronic ground state 0. It is significantly more allowed than the transition involving substate I. Hence, the line II → 0 appears already at relatively low temperature, although a thermal population via an activation energy of 19 cm^{-1} is required. Moreover, the corresponding absorption is high enough to allow us to register the excitation peak, too (Fig. 15a). As expected, it lies exactly (within limits of ±1 cm^{-1}) at the same energy as the corresponding emission line. The higher allowedness of the II → 0 transition also results in the much shorter emission decay time of $\tau_{II} = 6.4$ μs of substate II as compared to substate I (see below). A third 0–0 transition, corresponding to triplet substate III, is detected in the excitation spectrum at 19,863 cm^{-1} (503.45 nm). (This transition is used for excitation to obtain the selectively excited emission shown in Fig. 15a.) An identification of this transition in the emission spectrum would require application of a significantly higher temperature to provide sufficient

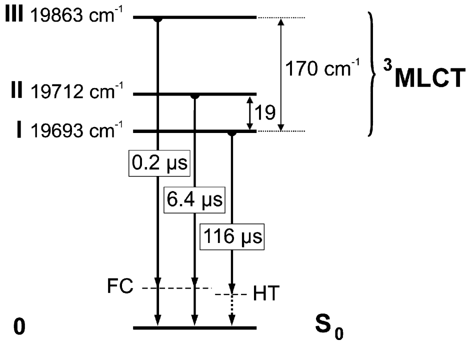

Fig. 16. Energy level diagram and emission decay times for Ir(ppy)$_3$ (**52**) in $\mathrm{CH_2Cl_2}$ ($c \approx 2 \times 10^{-5}$ mol/L). The individual decay times result from a fit according to Eq. (20) (Section 8.4). The levels depicted as FC and HT symbolize the involvement of Franck–Condon (FC) and Herzberg–Teller (HT) active vibrational modes, respectively (compare Refs. [40,175]).

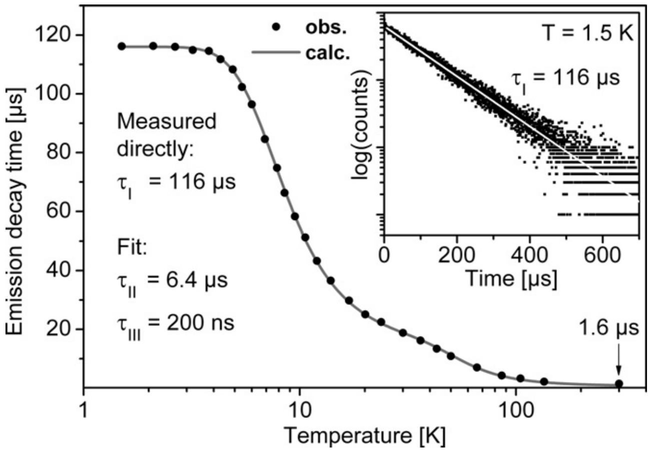

Fig. 17. Temperature dependence of the emission decay time of Ir(ppy)$_3$ (**52**) in $\mathrm{CH_2Cl_2}$ ($c \approx 2 \times 10^{-5}$ mol/L) recorded after pulsed and site-selective excitation at 19,863 cm^{-1} (0–0 transition 0 → III) and detection at 540 nm ($\approx$18,520 cm^{-1}). All decay curves are monoexponential over 5–6 decay times. The decay at 300 K was measured in a deaerated $\mathrm{CH_2Cl_2}$ solution. The decay times of $\tau_{\mathrm{II}} = 6.4$ µs and $\tau_{\mathrm{III}} = 0.2$ µs, given for the substates II and III of the ^{3}MLCT state, result from a fit of Eq. (20). The corresponding parameters are also summarized in Fig. 16.
Adapted from Ref. [40].

thermal population of this state, lying 170 cm^{-1} higher in energy. However, above about $T = 25$ K (corresponding to $k_{\mathrm{B}}T \approx 17$ cm^{-1}), all resolved spectra disappear because of temperature induced smearing-out effects, such as homogeneous electron–phonon coupling [40,79,197]. A still higher lying triplet substate could not be found up to an energy of about 500 cm^{-1} [40]. Thus, it is concluded that the three triplet substates identified represent the lowest triplet term.

Fig. 16 displays the resulting energy level diagram for the lowest triplet state of Ir(ppy)$_3$ in $\mathrm{CH_2Cl_2}$. The observed splitting, in particular, the large total ZFS of $\Delta E(\mathrm{ZFS}) = 170$ cm^{-1}, allow us to conclude that the emitting term is largely of MLCT character (compare Section 6) and that spin–orbit coupling to higher lying ^{1,3}MLCT states is very effective (Section 4). Especially, strong ^{1}MLCT admixtures are displayed in the short emission decay time of $\tau_{\mathrm{III}} = 200$ ns. This decay is almost purely radiative, since the emission quantum yield is as high as 90% in a $\mathrm{CH_2Cl_2}$ solution and almost 100% in PMMA (see also below). It is remarked that the conclusions concerning the high MLCT character are in line with the results obtained from theoretical investigations [83–85].

8.3. *Broad band emission*

The broad band emission spectra of Ir(ppy)$_3$ in $\mathrm{CH_2Cl_2}$, depicted in Fig. 15b, exhibit a similar temperature dependence as described above for the emission in the range of 0–0 transitions. The spectrum at 1.5 K, resulting from the lowest substate I, shows an emission band peaking at about 529 nm. Since the decay time is relatively long with $\tau_{\mathrm{I}} = 116$ µs, it is concluded that the transition I → 0 is largely forbidden. It has been proposed in Ref. [175] that the emission process from substate I is induced by vibronic coupling (Herzberg–Teller (HT) coupling), in particular, by spin-vibronic processes. These induce couplings to higher lying singlet states by the involvements of specific vibrational modes. This results in an occurrence of vibrational satellites, even when the purely electronic 0–0 transition is forbidden [78,79,175,244,245]. For Ir(ppy)$_3$, the vibrational satellite lines are smeared out by overlapping satellites, low-energy local phonon satellites, and strong (homogeneous) electron–phonon coupling to the matrix. Thus, the corresponding band maximum appears at 529 nm. With temperature increase, the substates II and III are thermally populated. They carry significantly more allowedness with respect to their 0–0 transitions to the electronic ground state than substate I. Thus, the corresponding emission spectra are dominated by the phonon sidebands of the electronic transitions and by Franck–Condon active vibrational satellites [78,79,175]. Since the electronic transitions grow in with temperature increase and since the vibrational energies of HT- and FC-active modes are usually different, an emission band with a blue shifted maximum appears near 514 nm (compare Fig. 15b).

8.4. *Emission decay times of the individual triplet substates*

Studies of the emission decay time and its temperature dependence provide valuable information on the individual triplet substates. At $T = 1.5$ K, only substate I is populated. Therefore, the corresponding decay time can be determined directly. With increasing temperature, the higher lying triplet substates are populated according to the Boltzmann distribution. This prevents a direct measurement of the individual decay times of the substates II and III. However, for a determination of the lifetimes of these substates, the indirect method as described in Section 6 can be applied, which makes use of the temperature dependence of the experimentally accessible thermalized (averaged) emission decay time.

Fig. 17 reproduces results of the emission decay measurements of Ir(ppy)$_3$ in $\mathrm{CH_2Cl_2}$ for the temperature range $1.5\,\mathrm{K} \le T \le 300\,\mathrm{K}$. By carrying out the fitting procedure according to Eq. (20) with fixed energy separations of $\Delta E_{\mathrm{I,II}} = 19$ cm^{-1} and $\Delta E_{\mathrm{I,III}} = 170$ cm^{-1} known from the high-resolution spectra, and with a fixed decay time of $\tau_{\mathrm{I}} = 116$ µs, recorded at 1.5 K, the two remaining free fit parameters are determined to $\tau_{\mathrm{II}} = 6.4$ µs and $\tau_{\mathrm{III}} = 0.2$ µs [40]. The resulting information is summarized in Figs. 16 and 17.

8.5. *Studies of Ir(ppy)$_3$ doped into PMMA*

Ir(ppy)$_3$ studied in a PMMA film shows only broad emission bands. However, investigations in an extended temperature range from 1.2 K up to about 370 K without any solid/liquid phase transition are possible in this matrix, in contrast to the situation using $\mathrm{CH_2Cl_2}$. Information on the individual substates can still be obtained by analyzing the temperature dependence of the thermalized emission decay time, as described in the preceding section. Again, it is required to measure the emission decay curves (at a low concentration of Ir(ppy)$_3$) over an extended temperature range. As expected and dissimilar to the situation found for the specific site of Ir(ppy)$_3$ in $\mathrm{CH_2Cl_2}$, these curves are not monoexponential because of inhomogeneity effects. Accordingly, a similar fit as described in Section 8.4, is not straightforward. However, in a

Table 4
Emission decay times and zero-field splittings of Ir(ppy)$_3$ in PMMA and CH$_2$Cl$_2$, respectively. The ranges given display inhomogeneous distributions (compare Ref. [40]).

Matrix	CH$_2$Cl$_2$[a]	PMMA[b]
τ_{I} [μs]	116	151–158
τ_{II} [μs]	6.4	13–18
τ_{III} [μs]	0.2	0.32–0.34
$\Delta E_{\text{I,II}}$ [cm^{-1}]	19	12–12.4
$\Delta E_{\text{I,III}}$ [cm^{-1}]	170	114–135

[a] Site-selective excitation at $\bar{\nu}_{exc} = 19,863\,\text{cm}^{-1}$ (503.45 nm).
[b] Non-selective excitation at $\bar{\nu}_{exc} = 28,170\,\text{cm}^{-1}$ (355 nm).

very rough approximation, one can estimate ranges of ZFS energies and of individual emission decay times simply by using a short and a long decay component, respectively, for every measured multi-exponential decay (compare also Section 7.3). With these data and applying Eq. (20) fits can be carried out. Thus, data sets are obtained, which represent approximate ranges of inhomogeneous distributions. Similar approaches have already been applied successfully in Refs. [40,102,233]. The resulting ranges of data are summarized in Table 4. For comparison, the values determined for Ir(ppy)$_3$ in CH$_2$Cl$_2$ are also given.

Interestingly, the photophysical properties of the ^{3}MLCT state of Ir(ppy)$_3$ in PMMA are somewhat different as compared to the situation found for CH$_2$Cl$_2$. In particular, the splitting of the triplet state is smaller and the individual decay times are longer in PMMA than in CH$_2$Cl$_2$. These differences can be explained by slight variations of metal d-orbital energies and changes of d- and π-orbital mixing, for example, because of matrix cage-induced geometry variations (compare Sections 3 and 4). These effects alter the SOC efficiencies and thus the ZFS and the emission decay times [79,87,102,233]. In other words, also the effects of mixing-in singlet character to the triplet substates via SOC are sensitive to the environment. It is remarked that especially triplet substate III determines the OLED performance crucially due to the high radiative rate of the transition from this substate to the electronic ground state (compare the values given in Table 4 for τ_{III}).

8.6. *Radiative and nonradiative decay rates and emission quantum yields of the individual triplet substates*

The emission quantum yield and the radiative and nonradiative decay rates of Ir(ppy)$_3$ have been investigated in PMMA for the temperature range of $1.5\,\text{K} \le T \le 370\,\text{K}$ [40]. Fig. 18 shows the temperature dependence of the emission quantum yield. In the range from 80 K up to 370 K, ϕ_{PL} is almost constant and lies between 96% and 97%. For the temperature range of $\approx 80\,\text{K} \le T \le 300\,\text{K}$, a similar value was reported in Ref. [39]. However, below 80 K our results differ from those of Ref. [39]. The quantum yield decreases from 96% to about 88% at 1.5 K. Between 12 K and 22 K a "plateau" with $\phi_{\text{PL}} \approx 90\%$ is observed. This behavior can be explained by the individual and different radiative and nonradiative rate constants of the three T$_1$ substates. At $T = 1.5$ K, only substate I is populated. Its quantum yield amounts to $\phi_{\text{PL}}(\text{I}) \approx 88\%$. Temperature increase leads to a population of substate II and at higher temperatures also of substate III. Between 12 K and 22 K, the emission stems dominantly from substate II which exhibits a quantum yield of about 90%, giving the first "plateau". At temperatures above 80 K, the emission from substate III dominates and a second and more extended plateau at a value of about 96% is found up to $T \approx 370$ K. The temperature dependence of the emission quantum yield $\phi_{\text{PL}}(T)$ (Fig. 18) can be used to determine the radiative and nonradiative rate constants for the transitions of the three individual triplet substates to the electronic ground state by applying the following expression (compare [40,173]):

$$\Phi_{\text{PL}}(T) = \frac{k_{\text{I}}^r + k_{\text{II}}^r e^{-(\Delta E_{\text{I,II}}/k_{\text{B}}T)} + k_{\text{III}}^r e^{-(\Delta E_{\text{I,III}}/k_{\text{B}}T)}}{k_{\text{I}} + k_{\text{II}} e^{-(\Delta E_{\text{I,II}}/k_{\text{B}}T)} + k_{\text{III}} e^{-(\Delta E_{\text{I,III}}/k_{\text{B}}T)}} \quad (22)$$

where k_{I}^r, k_{II}^r, and k_{III}^r are the radiative decay rates of the three triplet substates I, II, and III, respectively, while k_{I}, k_{II}, and k_{III} represent the total decay rates of these substates. These latter parameters are equal to the reciprocals of the experimentally determined individual decay times τ_{I}, τ_{II}, and τ_{III}, respectively.

Eq. (22) contains eight independent variables, of which the energies $\Delta E_{\text{I,II}}$ and $\Delta E_{\text{I,III}}$ as well as the rate constants k_{I}, k_{II}, and k_{III} can be extracted from Table 4, where ranges of ZFSs and emission decay times are given. We simply choose values lying in the center of these ranges. Thus, the number of independent variables in Eq. (22) is reduced from eight to three. With the mean values of $\Delta E_{\text{I,II}} = 12.2\,\text{cm}^{-1}$, $\Delta E_{\text{I,III}} = 125\,\text{cm}^{-1}$, $k_{\text{I}} = 1/(155\,\mu\text{s}) = 6.5 \times 10^3\,\text{s}^{-1}$, $k_{\text{II}} = 1/(15.5\,\mu\text{s}) = 6.5 \times 10^4\,\text{s}^{-1}$, and $k_{\text{III}} = 1/(0.33\,\mu\text{s}) = 3.0 \times 10^6\,\text{s}^{-1}$, the fit procedure, applying the data of Fig. 18 and using Eq. (22), gives the radiative decay rates of the individual triplet substates. By applying Eq. (3) and taking into account that $\tau_i = 1/k_i$ (with i = I, II, and III), the individual radiative and nonradiative rate constants as well as the quantum yields of the three substates can be calculated. These data are summarized in Table 5.

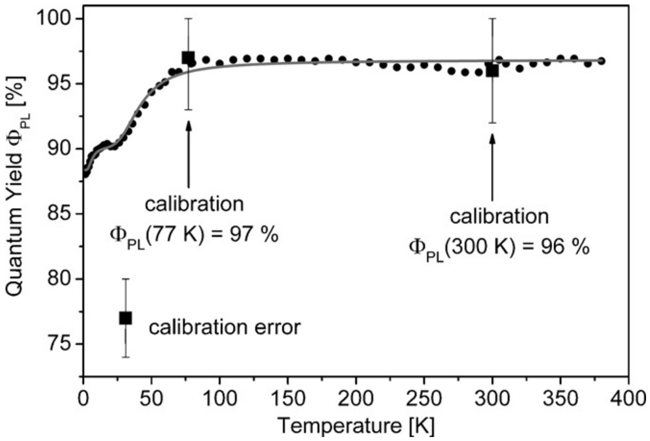

Fig. 18. Temperature dependence of the emission quantum yield of Ir(ppy)$_3$ in PMMA (≈0.01 wt%). The experimentally determined data are calibrated using the measured absolute photoluminescence quantum yield of (96 ± 4) % at T = 300 K and of (97 ± 3)% at T = 77 K. The solid line represents a fit according to Eq. (22). Adapted from Ref. [40].

The data displayed in Table 5 show that the radiative decay rates of the three substates of the T$_1$ state are strongly different. This is already known from the highly resolved excitation spectrum of Ir(ppy)$_3$ in CH$_2$Cl$_2$, since the corresponding intensities are proportional to the radiative rates (compare Fig. 15a). Here, we see again that the radiative rate for the transition from substate I to the singlet ground state is with $k_{\text{I}}^r = 5.7 \times 10^3\,\text{s}^{-1}$ very small. This displays the forbiddenness of this transition. It is remarked that this rate is given by the sum of all radiative transitions from substate I, including the 0–0 transition as well as all (smeared out) vibrational satellites. Since these are largely Herzberg–Teller induced, i.e. induced by spin-vibronic coupling (compare [78,79,175] and Section 8.3), the allowedness of the purely electronic 0–0 transition is extremely small. Therefore, substate I can be regarded as a relatively pure triplet substate with very little direct SOC to higher lying singlets. Interestingly, this is in line with conclusions from theoretical investigations of Nozaki [83].

On the other hand, the substates II and III exhibit radiative rates with respect to the transitions to the ground state, which are by a factor of about 10 and 500, respectively, greater than the rate of the

Table 5
Emission decay times, rate constants, and quantum yields of the ^{3}MLCT substates (with i = I, II, and III) of Ir(ppy)$_3$ in PMMA. The individual radiative (k_i^r) and nonradiative (k_i^{nr}) rate constants and emission quantum yields ($\phi_{\mathrm{PL}}(i)$) result from a fit of the measured emission quantum yield $\phi_{\mathrm{PL}}(T)$ according to Fig. 18 and Eq. (22) (compare Ref. [40]).

Triplet substate i	I	II	III
τ_i [µs]	155	15.5	0.33
k_i [s^{-1}]	6.5×10^3	6.5×10^4	3.0×10^6
k_i^r [s^{-1}]	$(5.7 \pm 0.3) \times 10^3$	$(5.8 \pm 0.3) \times 10^4$	$(2.9 \pm 0.1) \times 10^6$
k_i^{nr} [s^{-1}]	$(8 \pm 3) \times 10^2$	$(7 \pm 3) \times 10^3$	$(1 \pm 1) \times 10^5$
$\phi_{\mathrm{PL}}(i)$ [%]	88 ± 4	90 ± 4	97 ± 3

I → 0 transition. This is a consequence of distinctly stronger SOCs of the substates II and III to higher lying ^{1}MLCT states (compare Fig. 15, Section 4 and Refs. [79,83,86,87]).

Interestingly, the nonradiative rates of the three substates are also very different from each other. The nonradiative rate of substate I is almost one order of magnitude smaller than the nonradiative rate of substate II. This behavior is ascribed to the spin-forbiddenness of the radiationless relaxation process from substate I to the ground state. Such spin-dependent restrictions are also well known for intersystem crossing processes in purely organic molecules [30]. With increasing singlet admixture, these restrictions are less confining and thus, the nonradiative rates k_{II}^{nr} and k_{III}^{nr} become larger. A numerical comparison with the data given in Table 5 for k_{III}^{nr}, however, is not straightforward, since the given value strongly depends on the experimental error of the measured ϕ_{PL} value.

The individual quantum yields of the triplet substates display a behavior according to that of the individual radiative rates. Substate III exhibits the highest radiative rate and therefore, the highest quantum yield among the triplet substates, followed by substate II. Substate I shows the lowest individual quantum yield. It is stressed that the measured value of ϕ_{PL} at ambient temperature represents an averaged value that stems from the emissions of all three triplet substates according to their individual populations.

8.7. Concluding remarks

The large zero-field splitting of 170 cm^{-1} of the lowest triplet state of Ir(ppy)$_3$ allows us to assign this state as being largely of ^{3}MLCT character (compare Sections 4 and 6 and Refs. [33,78,79,86,87]). This assignment results also from theoretical investigations [83–85]. The large energy separation between the T$_1$ substates is a consequence of effective spin–orbit couplings (SOC) between these substates and higher lying triplet and singlet MLCT states involving d-orbitals other than the emitting triplet state. The zero-field splitting results from different interactions via SOC. Obviously, substate I experiences mainly an interaction with substates of other ^{3}MLCT states, while the substates II and especially III exhibit also significant SOCs with ^{1}MLCT states (compare Section 4). This leads to the very short emission decay time of $\tau_{\mathrm{III}} \approx 330$ ns of Ir(ppy)$_3$ in PMMA and of only $\tau_{\mathrm{III}} \approx 200$ ns in CH$_2$Cl$_2$. These values represent almost purely radiative decay times.

The result, showing that the nonradiative decay rates of the three substates of Ir(ppy)$_3$ differ by more than two orders of magnitude, is of particular interest and has not yet been recognized before. With respect to the discussions presented in Section 5.2.2, one can assume that all terms in Eq. (14) are largely equal for the three triplet substates except for the first term, representing the electronic coupling term ln(β). According to Eq. (18), this contribution to the nonradiative decay is small for weak SOC and can become significant for strong SOC. Indeed, this is displayed with respect to the three substates of Ir(ppy)$_3$. In particular, substate I represents an almost pure triplet and exhibits only a very small nonradiative decay rate of $k_{\mathrm{I}}^{nr} = 8 \times 10^2$ s^{-1}, while substate III with significant singlet admixtures exhibits a relatively large value of $k_{\mathrm{III}}^{nr} \approx 1 \times 10^5$ s^{-1}. Thus, it becomes obvious that the extent of SOC essentially determines also nonradiative rates.

The results further reveal that the emission properties of Ir(ppy)$_3$ depend on its environment. For example, for Ir(ppy)$_3$ in PMMA, the total ZFS is inhomogeneously distributed over a range of 115–135 cm^{-1} and becomes as large as 170 cm^{-1} in CH$_2$Cl$_2$. Accordingly, the emission decay time of substate III, representing the most important substate determining the radiative properties at ambient temperature, varies between 200 and 330 ns. Such effects were also observed for other Ir(III) compounds and could be rationalized by matrix cage-induced variations of the complex geometry which can alter energy separations between occupied d-orbitals and/or d- and π-orbitals (see Section 7 and Refs. [102,233]). Beside shifts of d-orbital energies, resulting in shifts of ^{1,3}MLCT states, also changes of d–π mixing occur. Thus, the SOC strengths are changed and therefore, modifications of crucial photophysical properties result. Consequently, an optimization of the OLED performance should take the immediate environment of the emitting complex, i.e. the matrix material, also into deeper consideration.

9. Case study Cu(POP)(pz$_2$BH$_2$) – A blue/white-blue emitter for singlet harvesting

The development of blue and white light emitting phosphorescent materials is still a challenge. Especially, the efficiency of blue light emission with Ir(III) or Pt(II) complexes (with suitably high T$_1$ energy) depends strongly on the energy separation between the emitting triplet state and higher lying metal centered states of dd* character. These strongly quench the emission, if they are thermally accessible at ambient temperature, i.e. if the energy separation to the T$_1$ state is less than about 3000 cm^{-1} (compare Section 5.2.1). Thus, it suggests itself to introduce other emitter materials which do not show these difficulties. In this respect, Cu(I) complexes with a d^{10} ground state configuration come into the focus of investigations, since low-lying unoccupied d* orbitals are not present. Therefore, emission quenching via population of dd* states is not a problem. However, the (radiative) emission decay times for the T$_1$ → S$_0$ transitions of Cu(I) compounds are usually extremely long and amount to many hundreds of µs up to ms [52–54,252,253]. Compounds with such long decay times would not be well suited as emitters in OLEDs since an extremely strong efficiency roll-off can be expected (compare Section 2).

However, specific Cu(I) complexes can exhibit a pronounced thermally activated delayed fluorescence of the lowest excited singlet state at ambient temperature [52–54,252–255]. Thus, the application of such materials, that make use of the singlet harvesting effect (see Section 2), as efficient emitters in OLEDs should be possible. Moreover, Cu(I) complexes are also attractive from another point of view. The material's costs are significantly lower than those of Pt(II) or Ir(III) based emitters.

Table 6
Emission properties of Cu(POP)(pz_2BH_2) in different matrices at ambient temperature [256].

	Powder[a]	PMMA[a]	CH_2Cl_2[b]
λ_{max} [nm]	436	462	535
τ [μs]	20	22	1.3
ϕ_{PL} [%]	45	35	9
CIE color coordinates [262]	0.15; 0.11	0.17; 0.21	0.35; 0.47

[a] Measured under N_2 atmosphere.
[b] Deaerated.

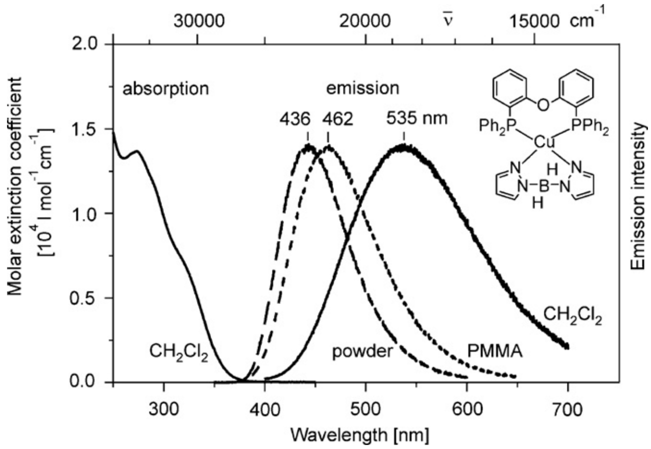

Fig. 19. Absorption (in CH_2Cl_2) and emission spectra of Cu(POP)(pz_2BH_2) measured in different matrices/environments at ambient temperature (CH_2Cl_2: $c = 5 \times 10^{-5}$ mol/L, PMMA: $c \approx 0.5$ wt%).

In this section, we present a new Cu(I) complex, Cu(POP)(pz_2BH_2) (see inset of Fig. 19), and discuss photophysical properties of this blue/white light emitting material.

9.1. Spectroscopic introduction

Fig. 19 shows the absorption spectrum of Cu(POP)(pz_2BH_2) in CH_2Cl_2 and the ambient temperature emission spectra of the compound as powder, doped into PMMA, and dissolved in CH_2Cl_2, respectively. The strong absorptions in the wavelength region below 280 nm can be assigned to spin allowed π–π* transitions (^{1}LC states) of the POP ligand. The lower energy absorptions between 310 and ≈370 nm are assigned to spin allowed d–π* transitions (^{1}MLCT states) involving the occupied 3d orbitals of Cu(I) and the π* orbitals mainly of the POP ligand (compare Refs. [256,257]).

Cu(POP)(pz_2BH_2) is strongly luminescent in the solid state and in PMMA, and moderately emissive in degassed liquid solutions. Table 6 summarizes the respective emission data. As it is seen, the emission properties of the material strongly depend on the environment. While the emission of neat Cu(POP)(pz_2BH_2) is blue ($\lambda_{max} = 436$ nm), it is blue/white in PMMA ($\lambda_{max} = 462$ nm) and green in fluid solution ($\lambda_{max} = 535$ nm), respectively. This latter red shift is accompanied by a considerable reduction of the emission quantum yield and a shortening of the emission decay time. These observations can be explained by changes of the molecular geometry of the Cu(I) compound taking place after MLCT excitation. In the electronic ground state, a pseudo-tetragonal orientation of the coordinating ligands is energetically favored, while in the excited MLCT state(s) a flattening distortion occurs [54,255,258–261]. Such a structural rearrangement leads to a smaller energy gap between the excited state and the electronic ground state. Connected with the geometry change, radiationless deactivation of the excited state becomes more efficient (compare also Section 5.2.2 and [54]). The geometry rearrangement in the excited state occurs most easily in fluid solution, it is partly hindered in PMMA, and minimized in a crystalline and thus rigid environment (powder).[6] It is of special interest that the emission of the Cu(I) complex in PMMA is with a halfwidth of about 4700 cm^{-1} relatively broad. Thus, the color purity is rather poor. However, an emission shift towards white light is obtained, though with a still not satisfactory color rendering index (CRI)). We relate the occurrence of this broad emission to the large Stokes shift and a distribution of local environments of the Cu(POP)(pz_2BH_2) molecules in the host polymer. This leads to a distribution of local hindrances and thus to a range of possible geometry changes. Obviously, this is a strategy for white light generation. The resulting effect is displayed by the CIE color coordinates [262] that are given in Table 6. However, in the context of the present investigation, we do not study this aspect further.

9.2. Triplet emission and thermally activated singlet emission

Fig. 20 shows emission spectra of Cu(POP)(pz_2BH_2) powder at temperatures ranging from 3 to 300 K. At all temperatures, the spectra are broad and unstructured. At 3 K, the emission is centered at 454 nm. Apart from a spectral broadening, no significant change of the emission profile is observed up to $T \approx 140$ K. However, with further temperature increase up to ambient temperature, the spectra become significantly broader, since a new emission band at higher energy grows in. This leads to a blue shift of the emission maximum by 18 nm.

The spectral blue shift with temperature increase is accompanied by a very pronounced change of the emission decay time. In Fig. 21, emission decay curves recorded at various temperatures are shown. At $T = 1.6$ K, the measured decay is clearly non-monoexponential. It can be fitted with a bi-exponential decay function, yielding time constants of 300 μs and 2.8 ms. With a slight temperature increase, the decay remains non-monoexponential, but above $T \approx 15$ K, a long decay component strongly prevails. At 30 K, the emission decays mono-exponentially with a time constant of 630 μs. Further temperature increase leads at first only to a minor reduction of the decay time. At $T = 115$ K, for example, it amounts to 590 μs. However, at temperatures of $T > 130$ K, the emission decay time decreases drastically to a value of 20 μs at 300 K.

The observations described above indicate the involvement of different energy states in dependence of temperature. Four different temperature ranges may be distinguished: (i) $1.6\,K \le T < 30$ K, (ii) $30\,K \le T < 120$ K, (iii) $120\,K \le T < 250$ K, and (iv) $T \ge 250$ K. At very low temperature, the emission originates from the substates of the lowest triplet state. As generally agreed in the literature [253,259,260,263–265], this state is largely of ^{3}MLCT character. It is expected that its total zero-field splitting ΔE(ZFS) is much smaller for Cu(I) complexes than for Ir(III) or Pt(II) compounds, since the

---

[6] For completeness, it is remarked that for the neat material, effects of energy transfer between the emitter complexes, as well as self-quenching and triplet–triplet-annihilation do not seem to be important. This can be rationalized by assuming at least a small geometry change in the excited state even for the neat material. Accordingly, the resonance condition required for the occurrence of radiationless energy transfer processes between excited and non-excited complexes is no longer fulfilled. Consequently, emission self-quenching and quenching by triplet-triplet annihilation become less probable.

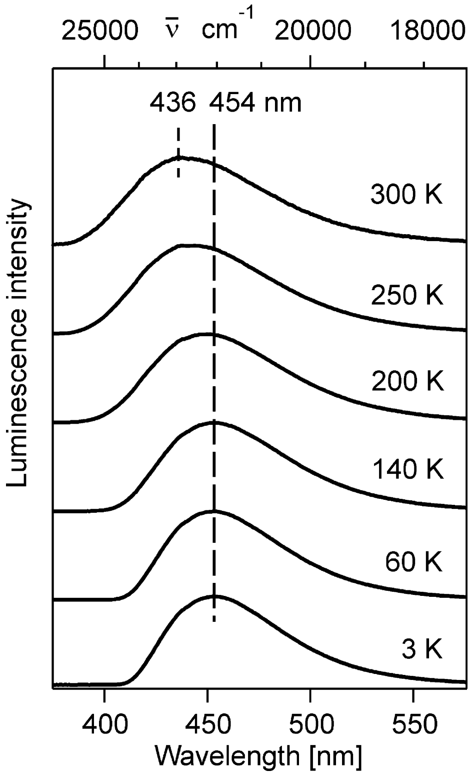

Fig. 20. Emission spectra of Cu(POP)(pz_2BH_2) powder measured after excitation at 355 nm (compare Ref. [256]).

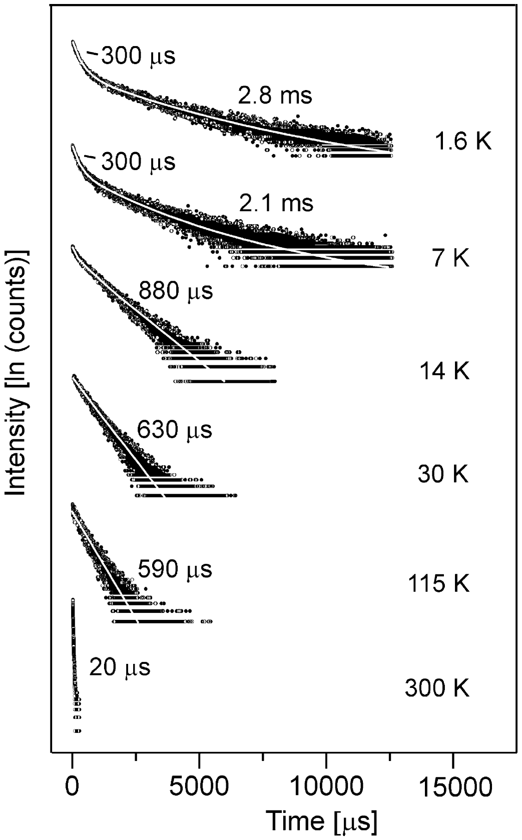

Fig. 21. Emission decay curves of Cu(POP)(pz_2BH_2) powder measured after pulsed excitation at λ_{exc} = 355 nm and detected at λ_{det} = 450 nm (compare Ref. [256]).

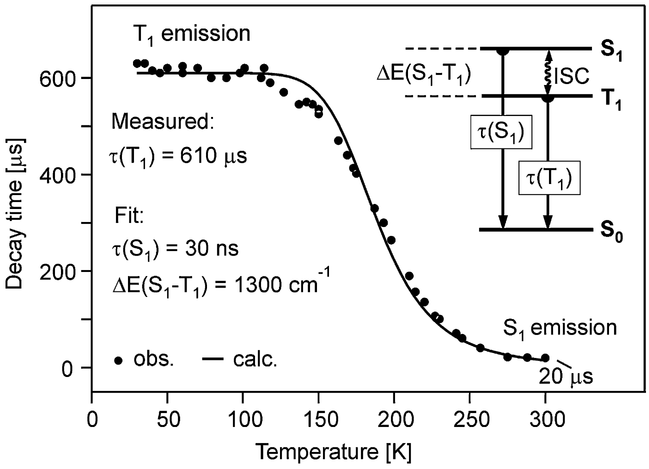

Fig. 22. Emission decay time of Cu(POP)(pz_2BH_2) powder versus temperature in the range of 30–300 K. The emission was excited with a pulsed UV laser (pulse width 12 ns) at λ_{exc} = 355 nm and detected at λ_{det} = 450 nm. The solid line is a fit of Eq. (24) to the experimental data. By use of the measured value of $\tau(T_1)$ = 610 μs, the fit parameters $\Delta E(S_1 - T_1)$ = 1300 cm^{-1} and $\tau(S_1)$ = 30 ns are obtained [256]. The inset displays the relevant energy states and shows schematically up and down intersystem crossings (ISC).

SOC constant of Cu(I) is by a factor of about five smaller than that of Ir(III) or Pt(II) [196]. Nevertheless, a splitting of the corresponding triplet of the order of 10 cm^{-1} is possible [263].

Presumably, such a splitting leads to the distinctly non-monoexponential decay curves in the temperature range (i). Under the assumption that intermolecular processes, such as energy transfer, may be disregarded, the decay curve at T = 1.6 K with components of 300 μs and 2.8 ms (Fig. 21) can be rationalized as follows: At this temperature and at a small energy separation of at least two triplet substates (possibly of 1 or 2 cm^{-1}), processes of spin-lattice relaxation are slow [176]. As a consequence, the states emit according to their individual decay times. With temperature increase, the SLR processes become faster and near T = 30 K the population of the T_1 substates is equilibrated. This leads to a monoexponential decay with an averaged decay time τ_{av} from about 30 K up to 120 K (range (ii)) [78,79,176,208,209,212,266]. The corresponding decay time can be expressed by Eq. (23), which is deduced from Eq. (20) for $\Delta E(ZFS) \ll k_BT$ [78,79,266].

$$\tau_{av} = 3\left(\frac{1}{\tau_I} + \frac{1}{\tau_{II}} + \frac{1}{\tau_{III}}\right)^{-1} \tag{23}$$

where τ_I, τ_{II}, and τ_{III} represent the emission decay times of the individual triplet substates I, II, and III, respectively. Very frequently, τ_{av} corresponds in a good approximation to the measured decay time of the three thermally equilibrated triplet substates. In the present case, the decay times of all three substates are not known. However, assuming in a relatively coarse approximation a value of the order of one ms for the third component and inserting it into Eq. (23) together with the experimentally determined time constants of 300 μs and 2.8 ms (Fig. 21), an averaged decay time of ≈640 μs would be obtained. This values would fit to the measured decay time at T = 30 K of τ = 630 μs.[7]

In the temperature range (ii), the emission decay time is characterized by a plateau with a time constant of about 610 μs. This value does not decrease significantly up to ≈120 K (Fig. 22). In this range, the emission of Cu(POP)(pz_2BH_2) stems from all three thermally equilibrated triplet substates.

---

[7] For completeness, it is remarked that the emission decay curve measured at T = 1.6 K (Fig. 21) could formally be well described by use of the three time constants discussed.

In the temperature range (iii) up to 250 K, the decay time becomes distinctly shorter (Fig. 22) and the emission maximum is blue shifted (Fig. 20). This indicates that a higher lying electronic state with a larger deactivation rate becomes involved (i.e. thermally populated). In analogy to other Cu(I) compounds [53,54,253,254,263], this state is assigned as the lowest excited singlet state S_1.

Finally, for temperatures higher than ≈250 K (range (iv)), the emission stemming from the S_1 state strongly dominates. It represents a delayed thermally activated fluorescence.

Under the assumption of a fast thermalization between the T_1 and the S_1 state, an average decay time can be expressed in analogy to Eq. (20), giving Eq. (24).

$$\tau_{av} = \frac{1+\exp(-(\Delta E(S_1-T_1)/k_BT))}{(1/\tau(T_1))+(1/\tau(S_1))\exp(-(\Delta E(S_1-T_1)/k_BT))} \quad (24)$$

$\tau(T_1)$ and $\tau(S_1)$ are the intrinsic decay times of the emitting triplet and singlet state, respectively, and $\Delta E(S_1-T_1)$ is the energy separation (activation energy) between the two states.

For a fit of Eq. (24) to the experimental data, the parameter $\tau(T_1)$ was kept constant at 610 μs, representing the averaged value of the plateau in the temperature range (ii) of $30\,K \le T < 120\,K$. The fit is depicted in Fig. 22 and reveals parameters of $\tau(S_1) = 30$ ns and $\Delta E(S_1-T_1) = 1300\,cm^{-1}$. This value of $\Delta E(S_1-T_1)$ corresponds to the energy difference between the T_1 state and the S_1 state. The obtained data are summarized in the energy level diagram as shown in Fig. 23.

9.3. Singlet harvesting with Cu(I) complexes

The analysis of the emission behavior of Cu(POP)(pz_2BH_2) has shown that this material may be well suited for singlet harvesting in an OLED device (compare Section 2). This is illustrated by use of Fig. 23.

A "pure" triplet emitter based on Cu(I) complexes exhibits a very long emission decay time. Thus, such materials would be expected to exhibit only a poor performance as OLED emitter, even if triplet harvesting (Section 2) is effective. However, for Cu(POP)(pz_2BH_2), the singlet state S_1 is easily thermally accessible at ambient temperature. This state carries a high deactivation rate with respect to the $S_1 \rightarrow S_0$ transition ($\tau(S_1) = 30$ ns). Thus, a thermally activated population of the S_1 state leads to a much faster (averaged) emission decay of the two states. Accordingly, the decay time drops by a factor of about 30 from 610 μs to 20 μs at $T = 300$ K. At this temperature, the thermally activated delayed fluorescence strongly prevails.

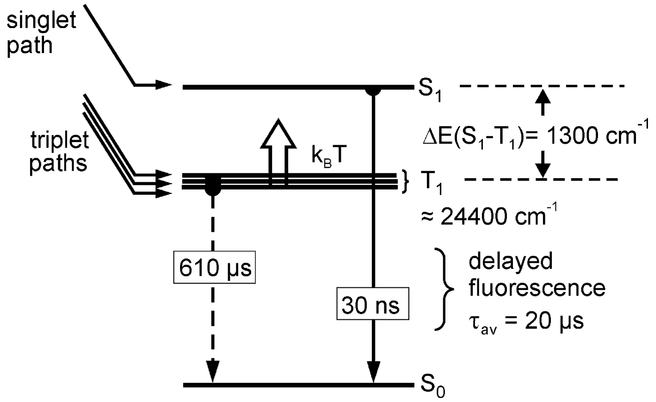

Fig. 23. Emission properties of Cu(POP)(pz_2BH_2) powder and singlet harvesting. At $T \le 120$ K, the emission stems only from the lowest triplet state T_1 with a decay time of its three thermalized substates of 610 μs. At $T = 300$ K, a thermally activated (delayed) fluorescence from the S_1 with a decay time of 20 μs is observed, while the decay time of the prompt fluorescence is estimated to about 30 ns by the fitting procedure as described in the text and displayed in Fig. 22. In an electroluminescence excitation, one singlet and three triplet paths populate the S_1 and the T_1 state. In principle, all excitons can be harvested, and because of efficient intersystem crossing from the T_1 state to the S_1 state the emission occurs as delayed S_1 fluorescence.

Inserting the rates of $k(S_1 \rightarrow S_0) = 1/(30\,ns)$ and $k(T_1 \rightarrow S_0) = 1/(610\,\mu s)$ as well as the activation energy of $\Delta E(S_1-T_1) = 1300\,cm^{-1}$ into Eq. (1) and ignoring nonradiative processes in this estimate, it is seen that at ambient temperature the fluorescence intensity predominates by a factor of about 40 over the phosphorescence. Interestingly, if blue light emission is aspired, the activation process is favorable, since the fluorescence is blue shifted by as much as 18 nm with respect to the phosphorescence maximum.

Applying electroluminescence excitation to this compound, one singlet path and three triplet paths populate the S_1 state and the T_1 state, respectively. SOC is large enough to induce fast intersystem crossing (ISC). At $T = 300$ K, both down and up ISC processes occur. Since the rate for a triplet emission is much smaller than the ISC rate, the excitation originally gathered in the T_1 state (three triplet paths) is radiatively deactivated via the S_1 state. Equivalently, the excitation energy that originally populates the S_1 state (one singlet path) is also deactivated as $S_1 \rightarrow S_0$ emission. In sum, the singlet state harvests and emits, at least predominantly, all generated excitons (apart from losses due to intrinsic non-radiative processes that are displayed by the photoluminescence quantum yield ϕ_{PL}). Interestingly, this new principle has also been applied recently in a green light emitting OLED [252]. Other realizations of OLEDs employing Cu(I) complexes as emitters [267–270] also support this strategy simply by demonstrating efficient devices.

In summary, it is remarked that Cu(POP)(pz_2BH_2) represents a very good example for the manifestation of the singlet harvesting effect. However, an emission decay time of 20 μs at $T = 300$ K is still too long for high brightness OLED applications. Developments of improved materials with smaller $\Delta E(S_1-T_1)$ values are currently in progress.

10. Conclusion

In this comprehensive study, we deepen the understanding of the triplet state of organo-transition metal emitters. A series of trends and relations between molecular structures and photophysical properties of the complexes is revealed.

In particular, spin-orbit coupling (SOC) determines crucially the emission behavior. For example, SOC is responsible for the emission decay times and quantum yields of the emitters. It is well known, that SOC determines the radiative rates of the transitions from the triplet substates to the electronic ground state. However, it is not so well known that also the nonradiative decay rates depend significantly on SOC. These rates increase with growing SOC. This behavior is exemplified by investigating the three triplet substates of Ir(ppy)$_3$ with respect to their individual radiative and nonradiative rates. A corresponding trend is also manifested by a comparison of a series of Pt(II) and Ir(III) complexes with the same ligands, such as the couples of Pt(4,6-dFppy)(acac)/Ir(4,6-dFppy)$_2$(acac) or Pt(thpy)(acac)/Ir(thpy)$_2$(acac).

SOC also regulates the amount of energy splitting (zero-field splitting, ΔE(ZFS)) of the triplet state into substates. Accordingly, very effective SOC induces large ΔE(ZFS) values and frequently also high radiative rates, in particular, to the transition from the highest triplet substate to the electronic singlet ground state. However, at large ΔE(ZFS) values, the average emission decay time of the three triplet substates at ambient temperature is not significantly reduced, even with high SOC efficiency. This is a consequence of the fact that emission properties are not only governed by the shortest lived triplet substate, but by all three substates weighted by a Boltzmann distribution. Thus, based on an extensive data set, an important trend becomes evident. It is indicated that the shortest (radiative) emission decay time of the type of materials investigated (and usually applied in OLEDs) cannot be significantly reduced to less than about 1 μs. This implicates problems concerning the development of emitter materials for high brightness OLED lighting.

It is also shown that the SOC efficiency distinctly depends on the geometry of a complex. This result is based on a series of experimental data and is explained in a comprehensible model. In particular, the effects of SOC can be significantly larger for quasi-octahedral Ir(III) or even Ru(II) complexes than for quasi-square-planar Pt(II) complexes. Moreover, the efficiency of SOC and thus its influence on the radiative properties depends also on the immediate environment of the emitter. This is demonstrated by case studies investigating $Ir(ppy)_3$ and also other emitters in various matrices in detail.

Currently, an extensive research is directed towards the development of efficient and stable blue light emitters that emit from ^{3}MLCT ($^3d\pi^*$) states. However, very frequently quenching dd* states are populated from these ^{3}MLCT states at ambient temperature and thus, only low photoluminescence quantum yields result. Therefore, it is aimed to energetically destabilize the lowest dd* states. Principally, this can be achieved by coordinating either chromophoric or ancillary ligands with very high ligand field strengths (high Dq values). On the other hand, these ligands do not only destabilize the d*-orbitals, but also stabilize the populated d-orbitals. Thus, also the ^{3}MLCT states shift to higher energies. As a consequence, the corresponding compound can become a $^3\pi\pi^*$ emitter, which exhibits an undesirably long emission decay time. Thus, this material would be less well suited for OLED applications. Obviously, only a detailed balance concerning the involvements of d-/π-orbitals in the lowest excited states might solve these problems.

Moreover, most compounds, when being excited, undergo certain geometry relaxations with respect to the ground state geometry, at least in a non-rigid environment. Such effects are particularly important for blue light ^{3}MLCT emitters, since geometry changes also stabilize the dd* states and thus, quenching can become more effective. This behavior is shortly addressed with respect to properties of the sky-blue light emitter $Ir(biqa)_3$. In a moderately rigid polymer (PMMA), the activation energy to the quenching state is already rather low and therefore, the emission quantum yield is reduced from almost 100% at 180 K to 50% at ambient temperature and drops further to 10% in a fluid solution (2-Me-THF). In this environment, the activation energy to the quenching state amounts to $2350\,cm^{-1}$.

The extensive discussions of triplet state properties are completed by presentations of case studies referring to highly efficient emitters. Thus, two Ir(III) compounds, the phosphorescent red light emitter $Ir(dm\text{-}2\text{-}piq)_2(acac)$ with $\phi_{PL} = 80\%$ and the phosphorescent green light emitter $Ir(ppy)_3$ with ϕ_{PL} of almost 100%, respectively, are characterized in detail. With respect to the emission properties, these materials are very well suited for OLED applications that are based on the triplet harvesting effect. In a third case study, the blue light emitting Cu(I) complex $Cu(POP)(pz_2BH_2)$ is characterized. Because of a d^{10} configuration of the electronic ground state, this material does not exhibit quenching by dd* states. Interestingly, at ambient temperature, this Cu(I) complex represents a singlet emitter. At least in principle, such emitters may be applied to harvest 100% of the generated singlet and triplet excitons according to the singlet harvesting effect. Potentially, this effect may successfully be applied in future not only to develop new and cheaper emitters, it may also be possible to reduce the average (radiative) emission decay time of the thermally activated fluorescence to below the limit that is found for typical triplet emitters. If successful, this strategy will help to reduce the roll-off of the OLED efficiency for lighting, even at high brightness applications.

Acknowledgements

The BMBF (German Federal Ministry of Education and Research) is acknowledged for the funding of our research. We are grateful to our cooperation partners and friends Prof. Dr. Mark E. Thompson and Dr. Peter Djurovich (University of Southern California), Dr. J.A. Gareth Williams (University of Durham), Prof. Dr. Chi-Ming Che, Prof. Dr. Wai-Kin Chan, and Dr. Chris S.-K. Mak (University of Hong Kong). These cooperations were supported by the DAAD (German Academic Exchange Service). Further, we thank Dr. Philipp Stössel and the Merck KGaA for enjoyable and fruitful cooperations. The COST project is acknowledged for financial support within the action D35 (WG 10). We further thank Priv.-Doz. Dr. Herbert H.H. Homeier for stimulating discussions.

References

[1] H. Yersin (Ed.), Highly Efficient OLEDs with Phosphorescent Materials, Wiley-VCH, Weinheim, 2008.
[2] Z.H. Kafafi (Ed.), Organic Electroluminescence, CRC Taylor & Francis, Boca Raton, 2005.
[3] J. Shinar (Ed.), Organic Light Emitting Devices, Springer, New York, 2004.
[4] P.T. Chou, Y. Chi, Chem. Eur. J 13 (2007) 380.
[5] C. Borek, K. Hanson, P.I. Djurovich, M.E. Thompson, K. Aznavour, R. Bau, Y. Sun, S.R. Forrest, J. Brooks, L. Michalski, J. Brown, Angew. Chem. Int. Ed. 46 (2007) 1109.
[6] R.C. Evans, P. Douglas, C.J. Winscom, Coord. Chem. Rev. 250 (2006) 2093.
[7] J.A.G. Williams, S. Develay, D.L. Rochester, L. Murphy, Coord. Chem. Rev. 252 (2008) 2596.
[8] L. Xiao, Z. Chen, B. Qu, J. Luo, S. Kong, Q. Gong, J. Kido, Adv. Mater 23 (2011) 926.
[9] H.-C. Su, H.-F. Chen, F.-C. Fang, C.-C. Liu, C.-C. Wu, K.-T. Wong, Y.-H. Liu, S.-M. Peng, J. Am. Chem. Soc. 130 (2008) 3413.
[10] H.J. Bolink, E. Coronado, R.D. Costa, N. Lardiés, E. Ortí, Inorg. Chem. 47 (2008) 9149.
[11] J. Slinker, D. Bernards, P.L. Houston, H.D. Abruña, S. Bernhard, G.G. Malliaras, Chem. Commun. (2003) 2392.
[12] A. Kapturkiewicz, in: P. Ceroni, A. Credi, M. Venturi (Eds.), Electrochemistry of Functional Supramolecular Systems, John Wiley & Sons, Hoboken, 2010, p. 477.
[13] A.S.P. Polo, M.K. Itokazu, N.Y.M. Iha, Coord. Chem. Rev. 248 (2004) 1343.
[14] N. Robertson, Angew. Chem. Int. Ed. 45 (2006) 2338.
[15] W.-Y. Wong, X.-Z. Wang, Z. He, A.B. Djurišić, C.-T. Yip, K.-Y. Cheung, H. Wang, C.S.K. Mak, W.-K. Chan, Nat. Mater. 6 (2007) 521.
[16] M. Grätzel, Inorg. Chem. 44 (2005) 6841.
[17] K.K.-W. Lo, M.-W. Louie, K.Y. Zhang, Coord. Chem. Rev. 254 (2010) 2603.
[18] E.J. O'Neil, B.D. Smith, Coord. Chem. Rev. 250 (2006) 3068.
[19] M.H. Keefe, K.D. Benkstein, J.T. Hupp, Coord. Chem. Rev. 205 (2000) 201.
[20] Q. Zhao, F. Li, C. Huang, Chem. Soc. Rev. 39 (2010) 3007.
[21] V. Fernández-Moreira, F.L. Thorp-Greenwood, M.P. Coogan, Chem. Commun. 46 (2010) 186.
[22] S.W. Botchway, M. Charnley, J.W. Haycock, A.W. Parker, D.L. Rochester, J.A. Weinstein, J.A.G. Williams, Proc. Natl. Acad. Sci. U.S.A. 105 (2008) 16071.
[23] K.A. Stephenson, S.R. Banerjee, T. Besanger, O.O. Sogbein, M.K. Levadala, N. McFarlane, J.A. Lemon, D.R. Boreham, K.P. Maresca, J.D. Brennan, J.W. Babich, J. Zubieta, J.F. Valliant, J. Am. Chem. Soc. 126 (2004) 8598.
[24] M. Yu, Q. Zhao, L. Shi, F. Li, Z. Zhou, H. Yang, T. Yi, C. Huang, Chem. Commun. (2008) 2115.
[25] K. Kalyanasundaram, Coord. Chem. Rev. 46 (1982) 159.
[26] K. Zeitler, Angew. Chem. Int. Ed. 48 (2009) 9785.
[27] N. Hoffmann, Chem. Rev. 108 (2008) 1052.
[28] S. Losse, J.G. Vos, S. Rau, Coord. Chem. Rev. 254 (2010) 2492.
[29] S.P. McGlynn, T. Azumi, M. Kinoshita, Molecular Spectroscopy of the Triplet State, Prentice-Hall, Eaglewood Cliff, 1969.
[30] N.J. Turro, Modern Molecular Photochemistry, Benjamin Inc., Menlo Park, 1978.
[31] M. Klessinger, J. Michl, Excited States and Photochemistry of Organic Molecules, VCH, New York, 1995.
[32] S. Lamansky, R.C. Kwong, M. Nugent, P.I. Djurovich, M.E. Thompson, Org. Electron. 2 (2001) 53.
[33] H. Yersin, Top. Curr. Chem. 241 (2004) 1.
[34] H. Yersin, Proc. SPIE 5214 (2004) 124.
[35] S Kalinin, M. Speckbacher, H. Langhals, L. B.-Å. Johansson, Phys. Chem. Chem. Phys. 3 (2001) 172.
[36] H. Langhals, J. Karolin, L.B.-Å. Johansson, J. Chem. Soc., Faraday Trans. 94 (1998) 2919.
[37] M. Montalti, A. Credi, L. Prodi, M.T. Gandolfi, Handbook of Photochemistry, 3rd ed., CRC Tayler & Francis, Boca Raton, 2006.
[38] T. Sajoto, P.I. Djurovich, A.B. Tamayo, J. Oxgaard, W.A. Goddard III, M.E. Thompson, J. Am. Chem. Soc. 131 (2009) 9813.

[39] K. Goushi, Y. Kawamura, H. Sasabe, C. Adachi, Jpn. J. Appl. Phys. 43 (2004) L937.
[40] T. Hofbeck, H. Yersin, Inorg. Chem. 49 (2010) 9290.
[41] H. Yersin, U. Monkowius, DE 10 2008 033 563 A1.
[42] H. Yersin, U. Monkowius, WO 2010/006681 A1.
[43] H. Yersin, R. Czerwieniec, T. Fischer, DE 10 2010 005 463.1.
[44] H. Yersin, R. Czerwieniec, U. Monkowius, DE 10 2010 031 8031.
[45] H. Yersin, Controlling Photophysical Properties of Metal Complexes: Toward Molecular Photonics, COST D35 Workshop, Prague (Czech Republic), May 2010, Book of Abstracts, p. 6.
[46] H. Yersin, Proceedings of the 4th International Conference on Molecular Materials, MOLMAT 2010, Montpellier (France), 2010, Book of Abstracts, p. 026.
[47] R.E. Brown, L.A. Singer, J.H. Parks, Chem. Phys. Lett. 14 (1972) 193.
[48] C.A. Parker, C.G. Hatchard, Trans. Faraday Soc. 57 (1961) 1894.
[49] J. Saltiel, H.C. Curtis, L. Metts, J.W. Miley, J. Winterle, M. Wrighton, J. Am. Chem. Soc. 92 (1970) 410.
[50] A. Maciejewski, M. Szymanski, R.P. Steer, J. Phys. Chem. 90 (1986) 6314.
[51] H. Yersin, H. Otto, G. Gliemann, Theor. Chim. Acta (Berlin) 33 (1974) 63.
[52] G. Blasse, D.R. McMillin, Chem. Phys. Lett. 70 (1980) 1.
[53] J.R. Kirchhoff, R.E. Gamache Jr., M.W. Blaskie, A.A. Del Paggio, R.K. Lengel, D.R. McMillin, Inorg. Chem. 22 (1983) 2380.
[54] A. Tsuboyama, K. Kuge, M. Furugori, S. Okada, M. Hoshino, K. Ueno, Inorg. Chem. 46 (2007) 1992.
[55] K. Walzer, B. Maennig, M. Pfeiffer, K. Leo, Chem. Rev. 107 (2007) 1233.
[56] M.A. Baldo, S.R. Forrest, M.E. Thompson, in: Z.H. Kafafi (Ed.), Organic Electroluminescence, Taylor & Francis, Boca Raton, 2005, p. 267.
[57] W. Brütting (Ed.), Physics of Organic Semiconductors, Wiley-VCH, Weinheim, 2005.
[58] S. Nowy, B.C. Krummacher, J. Frischeisen, N.A. Reinke, W. Brütting, J. Appl. Phys. 104 (2008) 123109.
[59] N.C. Greenham, R.H. Friend, D.D.C. Bradley, Adv. Mater. 6 (1994) 491.
[60] J.-S. Kim, P.K.H. Ho, N.C. Greenham, R.H. Friend, J. Appl. Phys. 88 (2000) 1073.
[61] K. Saxena, V.K. Jain, D.S. Mehta, Opt. Mater. 32 (2009) 221.
[62] M.A. Baldo, D.F. O'Brien, Y. You, A. Shoustikov, S. Sibley, M.E. Thompson, S.R. Forrest, Nature 395 (1998) 151.
[63] T. Tsutsui, in: Z.H. Kafafi (Ed.), Organic Electroluminescence, Taylor & Francis, Boca Raton, 2005, p. 1.
[64] B. Geffroy, P. le Roy, C. Prat, Polym. Int. 55 (2006) 572.
[65] C. Adachi, M.A. Baldo, M.E. Thompson, S.R. Forrest, J. Appl. Phys. 90 (2001) 5048.
[66] J. Kalinowski, Organic Light Emitting Diodes: Principles Characteristics and Processes, Marcel Dekker Inc., New York, 2004.
[67] S. Reineke, K. Walzer, K. Leo, Phys. Rev. B 75 (2007) 125328.
[68] N.C. Giebink, S.R. Forrest, Phys. Rev. B 77 (2008) 235215.
[69] D. Tanaka, H. Sasabe, Y.-J. Li, S.-J. Su, T. Takeda, J. Kido, Jpn. J. Appl. Phys. 46 (2007) L10.
[70] S. Reineke, G. Schwartz, K. Walzer, K. Leo, Appl. Phys. Lett. 91 (2007) 123508.
[71] J. Kalinowski, W. Stampor, J. Szmytkowski, D. Virgili, M. Cocchi, V. Fattori, C. Sabatini, Phys. Rev. B 74 (2006) 085316.
[72] D. Hertel, K. Meerholz, J. Phys. Chem. B 111 (2007) 12075.
[73] A. Köhler, H. Bässler, Mat. Sci. Eng. R 66 (2009) 71.
[74] M.A. Baldo, S. Lamansky, P.E. Burrows, M.E. Thompson, S.R. Forrest, Appl. Phys. Lett. 75 (1999) 4.
[75] C. Adachi, M.A. Baldo, S.R. Forrest, M.E. Thompson, Appl. Phys. Lett. 77 (2000) 904.
[76] G. Schwartz, S. Reineke, K. Walzer, K. Leo, Appl. Phys. Lett. 92 (2008) 053311.
[77] S.-J. Su, H. Sasabe, T. Takeda, J. Kido, Chem. Mater. 20 (2008) 1691.
[78] H. Yersin, D. Donges, Top. Curr. Chem. 214 (2001) 81.
[79] H. Yersin, W.J. Finkenzeller, in: H. Yersin (Ed.), Highly Efficient OLEDs with Phosphorescent Materials, Wiley-VCH, Weinheim, 2008, p. 1.
[80] M. Yagi, B.D. Schlyer, A.H. Maki, Chem. Phys. 157 (1991) 209.
[81] H. Miki, T. Azumi, J. Phys. Chem. 98 (1994) 6059.
[82] T. Azumi, H. Miki, Top. Curr. Chem. 191 (1997) 1.
[83] K. Nozaki, J. Chin. Chem. Soc. 53 (2006) 101.
[84] E. Jansson, B. Minaev, S. Schrader, H. Ågren, Chem. Phys. 333 (2007) 157.
[85] P.J. Hay, J. Phys. Chem. A 106 (2002) 1634.
[86] A.F. Rausch, H.H.H. Homeier, P.I. Djurovich, M.E. Thompson, H. Yersin, Proc. SPIE 6655 (2007) 66550F.
[87] A.F Rausch, H.H.H. Homeier, H. Yersin, Top. Organomet. Chem. 29 (2010) 193.
[88] A. Szabo, N.S. Ostlund, Modern Quantum Chemistry: Introduction to Advanced Electronic Structure Theory, McGraw-Hill, New York, 1989.
[89] S. Obara, M. Itabashi, F. Okuda, S. Tamaki, Y. Tanabe, Y. Ishii, K. Nozaki, M.-A. Haga, Inorg. Chem. 45 (2006) 8907.
[90] Z.A. Siddique, T. Ohno, K. Nozaki, T. Tsubomura, Inorg. Chem. 43 (2004) 663.
[91] H. Miki, M. Shimada, T. Azumi, J.A. Brozik, G.A. Crosby, J. Phys. Chem. 97 (1993) 11175.
[92] S. Kimachi, R. Satomi, H. Miki, K. Maeda, T. Azumi, J. Phys. Chem. A 101 (1997) 345.
[93] C. Giesbergen, M. Glasbeek, J. Phys. Chem. 97 (1993) 9942.
[94] S. Ikeda, S. Yamamoto, K. Nozaki, T. Ikeyama, T. Azumi, J.A. Burt, G.A. Crosby, J. Phys. Chem. 95 (1991) 8538.
[95] H.L. Schläfer, G. Gliemann, Basic Principles of Ligand Field Theory, Wiley-Interscience, London, 1969.
[96] B.N. Figgis, Comprehensive Coord. Chem., Pergamon, Oxford, 1987.
[97] A. Ceulemans, L.G. Vanquickenborne, J. Am. Chem. Soc. 103 (1981) 2238.
[98] E.M. Kober, T.J. Meyer, Inorg. Chem. 21 (1982) 3967.
[99] C. Daul, E.J. Baerends, P. Vernooijs, Inorg. Chem. 33 (1994) 3538.
[100] T. Ziegler, J.K. Nagle, J.G. Snijders, E.J. Baerends, J. Am. Chem. Soc. 111 (1989) 5631.
[101] M.H. Wilson, L.P. Ledwaba, J.S. Field, D.R. McMillin, Dalton Trans. (2005) 2754.
[102] A.F. Rausch, M.E. Thompson, H. Yersin, J. Phys. Chem. A 113 (2009) 5927.
[103] J. Li, P.I. Djurovich, B.D. Alleyne, M. Yousufuddin, N.N. Ho, J.C. Thomas, J.C. Peters, R. Bau, M.E. Thompson, Inorg. Chem. 44 (2005) 1713.
[104] A.F. Rausch, M.E. Thompson, H. Yersin, Chem. Phys. Lett. 468 (2009) 46.
[105] A.F. Rausch, H. Yersin, Chem. Phys. Lett. 484 (2010) 261.
[106] J. Brooks, Y. Babayan, S. Lamansky, P.I. Djurovich, I. Tsyba, R. Bau, M.E. Thompson, Inorg. Chem. 41 (2002) 3055–3066.
[107] T. Fischer, Ph.D. Thesis, Universität Regensburg (2010).
[108] D.N. Kozhevnikov, V.N. Kozhevnikov, M.M. Ustinova, A. Santoro, D.W. Bruce, B. Koenig, R. Czerwieniec, T. Fischer, M. Zabel, H. Yersin, Inorg. Chem. 48 (2009) 4179.
[109] T. Fischer, R. Czerwieniec, T. Hofbeck, M.M. Osminina, H. Yersin, Chem. Phys. Lett. 486 (2010) 53.
[110] D. Pentlehner, Diplomarbeit, Universität Regensburg (2006).
[111] S. Lamansky, P.I. Djurovich, D. Murphy, F. Abdel-Razzaq, R. Kwong, I. Tsyba, M. Bortz, B. Mui, R. Bau, M.E. Thompson, Inorg. Chem. 40 (2001) 1704.
[112] D. Pentlehner, T. Hofbeck, M.E. Thompson, H. Yersin, unpublished data.
[113] T. Hofbeck, R. Czerwieniec, H. Yersin, unpublished data.
[114] M.A. Baldo, C. Adachi, S.R. Forrest, Phys. Rev. B 62 (2000) 10967.
[115] W.L. Fleeman, W.B. Connick, Comments Inorg. Chem. 23 (2002) 205.
[116] S.-W. Lai, M.C.-W. Chan, T.-C. Cheung, S.-M. Peng, C.-M. Che, Inorg. Chem. 38 (1999) 4046.
[117] W.B. Connick, H.B. Gray, J. Am. Chem. Soc. 119 (1997) 11620.
[118] W.B. Connick, D. Geiger, R. Eisenberg, Inorg. Chem. 38 (1999) 3264.
[119] C.S.K. Mak, W.K. Chan, T. Fischer, H. Yersin, US Patent Application 61/264,731.
[120] S.-C. Lo, R.E. Harding, C.P. Shipley, S.G. Stevenson, P.L. Burn, I.D.W. Samuel, J. Am. Chem. Soc. 131 (2009) 16681.
[121] S.-C. Lo, R.N. Bera, R.E. Harding, P.L. Burn, I.D.W. Samuel, Adv. Funct. Mater. 18 (2008) 3080.
[122] J.M. Lupton, I.D.W. Samuel, R. Beavington, P.L. Burn, H. Bässler, Adv. Mater. 13 (2001) 258.
[123] J.N. Demas, E.W. Harris, R.P. McBride, J. Am. Chem. Soc. 99 (1977) 3547.
[124] P.I. Djurovich, D. Murphy, M.E. Thompson, B. Hernandez, R. Gao, P.L. Hunt, M. Selke, Dalton Trans. (2007) 3763.
[125] C. Schweitzer, R. Schmidt, Chem. Rev. 103 (2003) 1685.
[126] C. Schaffner-Hamann, A. von Zelewsky, A. Barbieri, F. Barigelletti, G. Muller, J.P. Riehl, A. Neels, J. Am. Chem. Soc. 126 (2004) 9339.
[127] V.V. Korolev, A.L. Mamaev, B.V. Bol'shakov, N.M. Bazhin, J. Polym. Sci. B: Polymer Phys. 36 (1998) 127.
[128] C.S.K. Mak, D. Pentlehner, M. Stich, O.S. Wolfbeis, W.K. Chan, H. Yersin, Chem. Mater. 21 (2009) 2173.
[129] D.B. Papkovsky, G.V. Ponomarev, W. Trettnak, P. O'Leary, Anal. Chem. 67 (1995) 4112.
[130] S. Ji, W. Wu, Y. Wu, T. Zhao, F. Zhuo, Y. Yang, X. Zhang, X. Liang, W. Wu, L. Chi, Z. Wang, J. Zhao, Analyst 134 (2009) 958.
[131] D.K. Crites Tears, D.R. McMillin, Coord. Chem. Rev. 211 (2001) 195.
[132] E.M. Stacy, D.R. McMillin, Inorg. Chem. 29 (1990) 393.
[133] C.-W. Chan, L.-K. Cheng, C.-M. Che, Coord. Chem. Rev. 132 (1994) 87.
[134] M.D. Perez, P.I. Djurovich, A. Hassan, G.Y. Cheng, T.J. Stewart, K. Aznavour, R. Bau, M.E. Thompson, Chem. Commun. (2009) 4215.
[135] A. Islam, N. Ikeda, K. Nozaki, Y. Okamoto, B. Gholamkhass, A. Yoshimura, T. Ohno, Coord. Chem. Rev. 171 (1998) 355.
[136] F. Barigelletti, D. Sandrini, M. Maestri, V. Balzani, A. von Zelewsky, L. Chassot, P. Jolliet, U. Maeder, Inorg. Chem. 27 (1988) 3644.
[137] T.J. Meyer, Pure Appl. Chem. 58 (1986) 1193.
[138] J. van Houten, R.J. Watts, Inorg. Chem. 17 (1978) 3381.
[139] J.V. Caspar, T.J. Meyer, J. Am. Chem. Soc. 105 (1983) 5583.
[140] J.A.G. Williams, Top. Curr. Chem. 281 (2007) 205.
[141] L. Yang, F. Okuda, K. Kobayashi, K. Nozaki, Y. Tanabe, Y. Ishii, M.-a. Haga, Inorg. Chem. 47 (2008) 7154.
[142] G. Treboux, J. Mizukami, M. Yabe, S. Nakamura, Chem. Lett. 36 (2007) 1344.
[143] A. Bossi, T. Steward, P.I. Djurovich, M.E. Thompson, M.J. Leitl, A.F. Rausch, R. Huber, H. Yersin, in preparation.
[144] T. Sajoto, P.I. Djurovich, A. Tamayo, M. Yousufuddin, R. Bau, M.E. Thompson, R.J. Holmes, S.R. Forrest, Inorg. Chem. 44 (2005) 7992.
[145] S. Haneder, E. Da Como, J. Feldmann, J.M. Lupton, C. Lennartz, P. Erk, E. Fuchs, O. Molt, I. Münster, C. Schildknecht, G. Wagenblast, Adv. Mater. 20 (2008) 3325.
[146] C.-F. Chang, Y.-M. Cheng, Y. Chi, Y.-C. Chiu, C.-C. Lin, G.-H. Lee, P.-T. Chou, C.-C. Chen, C.-H. Chang, C.-C. Wu, Angew. Chem. Int. Ed. 47 (2008) 4542.
[147] J.A.G. Williams, A. Beeby, E.S. Davies, J.A. Weinstein, C. Wilson, Inorg. Chem. 42 (2003) 8609.
[148] S.J. Farley, D.L. Rochester, A.L. Thompson, J.A.K. Howard, J.A.G. Williams, Inorg. Chem. 44 (2005) 9690.
[149] A.F. Rausch, L. Murphy, J.A.G. Williams, H. Yersin, Inorg. Chem. 48 (2009) 11407.
[150] C.S. Chin, M.-S. Eum, S.Y. Kim, C. Kim, S.K. Kang, Eur. J. Inorg. Chem. (2007) 372.
[151] M.-S. Eum, C.S. Chin, S.Y. Kim, C. Kim, S.K. Kang, N.H. Hat, J.H. Seo, G.Y. Kim, Y.K. Kim, Inorg. Chem. 47 (2008) 6289.
[152] D. Di Censeo, S. Fantacci, F. De Angelis, C. Klein, N. Evans, K. Kalyanasundaram, H.J. Bolink, M. Grätzel, M.K. Nazeeruddin, Inorg. Chem. 47 (2008) 980.

[153] K. Maruszewski, D.P. Strommen, J.R. Kincaid, J. Am. Chem. Soc. 115 (1993) 8345.
[154] M.E. von Arx, E. Burattini, A. Hauser, L. van Pieterson, R. Pellaux, S. Decurtins, J. Phys. Chem. A 104 (2000) 883.
[155] E. Danielsson, R.S. Lumpkin, T.J. Meyer, J. Phys. Chem. 91 (1987) 1305.
[156] D.W. Thompson, C.N. Fleming, B.D. Myron, T.J. Meyer, J. Phys. Chem. B 111 (2007) 6930.
[157] G.W. Robinson, R.P. Frosch, J. Chem. Phys. 38 (1963) 1187.
[158] R. Englman, J. Jortner, Mol. Phys. 18 (1970) 145.
[159] W. Siebrand, J. Chem. Phys. 46 (1967) 440.
[160] K.F. Freed, J. Jortner, J. Chem. Phys. 52 (1970) 6272.
[161] W. Siebrand, J. Chem. Phys. 47 (1967) 2411.
[162] H.J. Griesser, U.P. Wild, Chem. Phys. 52 (1980) 117.
[163] A. Maciejewski, A. Safarzadeh-Amiri, R.E. Verrall, R.P. Steer, Chem. Phys. 87 (1984) 295.
[164] J.S. Wilson, N. Chawdhury, M.R.A. Al-Mandhary, M. Younus, M.S. Khan, P.R. Raithby, A. Köhler, R.H. Friend, J. Am. Chem. Soc. 123 (2001) 9412.
[165] D.J. Stufkens, A. Vlček Jr., Coord. Chem. Rev. 177 (1998) 127.
[166] C.E. Whittle, J.A. Weinstein, M.W. George, K.S. Schanze, Inorg. Chem. 40 (2001) 4053.
[167] J.V. Caspar, E.M. Kober, B.P. Sullivan, T.J. Meyer, J. Am. Chem. Soc. 104 (1982) 630.
[168] L.A. Worl, R. Duesing, P. Chen, L. Della Ciana, T.J. Meyer, J. Chem. Soc., Dalton Trans. (1991) 849.
[169] E.M. Kober, J.V. Caspar, R.S. Lumpkin, T.J. Meyer, J. Phys. Chem. 90 (1986) 3722.
[170] J.A. Treadway, B. Loeb, R. Lopez, P.A. Anderson, F.R. Keene, T.J. Meyer, Inorg. Chem. 35 (1996) 2242.
[171] D.A.K. Vezzu, J.C. Deaton, J.S. Jones, L. Bartolotti, C.F. Harris, A.P. Marchetti, M. Kondakova, R.D. Pike, S. Huo, Inorg. Chem. 49 (2010) 5107.
[172] T. Hofbeck, Ph.D. Thesis, Universität Regensburg, in preparation.
[173] G.D. Hager, G.A. Crosby, J. Am. Chem. Soc. 97 (1975) 7031.
[174] T. Azumi, C.M. O'Donnell, S.P. McGlynn, J. Chem. Phys. 45 (1966) 2735.
[175] W.J. Finkenzeller, H. Yersin, Chem. Phys. Lett. 377 (2003) 299.
[176] H. Yersin, J. Strasser, Coord. Chem. Rev. 208 (2000) 331.
[177] W.J. Finkenzeller, M.E. Thompson, H. Yersin, Chem. Phys. Lett. 444 (2007) 273.
[178] W. Humbs, H. Yersin, Inorg. Chem. 35 (1996) 2220.
[179] W.J. Finkenzeller, T. Hofbeck, M.E. Thompson, H. Yersin, Inorg. Chem. 46 (2007) 5076.
[180] H.-F. Xiang, S.-W. Lai, P.T. Lai, C.-M. Che, in: H. Yersin (Ed.), Highly Efficient OLEDs with Phosphorescent Materials, Wiley-VCH, Weinheim, 2008.
[181] C.-M. Che, C.-C. Kwok, S.-W. Lai, A.F. Rausch, W.J. Finkenzeller, N. Zhu, H. Yersin, Chem. Eur. J. 16 (2010) 233.
[182] C.-M. Che, S.-C. Chan, H.-F. Xiang, M.C.W. Chan, Y. Liu, Y. Wang, Chem. Commun. (2004) 1484.
[183] J. Kalinowski, M. Cocchi, D. Virgili, V. Fattori, J.A.G. Williams, Adv. Mater. 19 (2007) 4000.
[184] M. Cocchi, J. Kalinowski, V. Fattori, J.A.G. Williams, L. Murphy, Appl. Phys. Lett. 94 (2009) 073309.
[185] S.-Y. Chang, J. Kavitha, S.-W. Li, C.-S. Hsu, Y. Chi, Y.-S. Yeh, P.-T. Chou, G.-H. Lee, A.J. Carty, Y.-T. Tao, C.-H. Chien, Inorg. Chem. 45 (2006) 137.
[186] X. Yang, Z. Wang, S. Makaduni, J. Li, G.E. Jabbour, Adv. Mater. 20 (2008) 2405.
[187] V. Adamovich, J. Brooks, A. Tamayo, A.M. Alexander, P.I. Djurovich, B.W. D'Andrade, C. Adachi, S.R. Forrest, M.E. Thompson, New. J. Chem. 26 (2002) 1171.
[188] B. Ma, P.I. Djurovich, S. Garon, B. Alleyne, M.E. Thompson, Adv. Funct. Mater. 16 (2006) 2438.
[189] L. Murphy, J.A.G. Williams, Top. Organomet. Chem. 28 (2010) 75.
[190] H. Yersin, W. Humbs, J. Strasser, Coord. Chem. Rev. 159 (1997) 325.
[191] W.H. Elfring, G.A. Crosby, J. Am. Chem. Soc. 103 (1981) 7061.
[192] D.C. Baker, K.W. Hipps, G.A. Crosby, Chem. Phys. Lett. 53 (1978) 333.
[193] M. Kato, S. Yamauchi, N. Hirota, Chem. Phys. Lett. 157 (1989) 543.
[194] H. Yersin, D. Braun, Chem. Phys. Lett. 179 (1991) 85.
[195] H. Riesen, E. Krausz, Chem. Phys. Lett. 212 (1993) 347.
[196] S.L. Murov, J. Carmichael, G.L. Hug, Handbook of Photochemistry, 2nd ed., Marcel Dekker, New York, 1993, p. 340.
[197] R. Bauer, W.J. Finkenzeller, U. Bogner, M.E. Thompson, H. Yersin, Org. Electron 9 (2008) 641.
[198] H. Yersin, D. Donges, J.K. Nagle, R. Sitters, M. Glasbeek, Inorg. Chem. 39 (2000) 770.
[199] M. Glasbeek, Top. Curr. Chem. 213 (2001) 95.
[200] M. Glasbeek, R. Sitters, E. van Veldhoven, A. von Zelewsky, W. Humbs, H. Yersin, Inorg. Chem. 37 (1998) 5159.
[201] J. Westra, M. Glasbeek, Chem. Phys. Lett. 166 (1990) 535.
[202] H. Yersin, D. Donges, W. Humbs, J. Strasser, R. Sitters, M. Glasbeek, Inorg. Chem. 41 (2002) 4915.
[203] W. Halper, M.K. DeArmond, J. Lumin. 5 (1972) 225.
[204] Y. Komada, S. Yamauchi, N. Hirota, J. Phys. Chem. 90 (1986) 6425.
[205] D. Donges, J.K. Nagle, H. Yersin, J. Lumin. 72–74 (1997) 658.
[206] M. Maestri, D. Sandrini, V. Balzani, A. von Zelewsky, P. Jolliet, Helv. Chim. Acta 71 (1988) 134.
[207] H. Yersin, S. Schützenmeier, H. Wiedenhofer, A. von Zelewsky, J. Phys. Chem. 97 (1993) 13496.
[208] J. Schmidt, H. Wiedenhofer, A. von Zelewsky, H. Yersin, J. Phys. Chem. 99 (1995) 226.
[209] D. Donges, J.K. Nagle, H. Yersin, Inorg. Chem. 36 (1997) 3040.
[210] R. Ballardini, G. Varani, M.T. Indelli, F. Scandola, Inorg. Chem. 25 (1986) 3858.
[211] R. Huber, Diplomarbeit, Universität Regensburg (2008).
[212] W.J. Finkenzeller, P. Stößel, H. Yersin, Chem. Phys. Lett. 397 (2004) 289.
[213] R. Czerwieniec, W.J. Finkenzeller, T. Hofbeck, A. Starukhin, A. Wedel, H. Yersin, Chem. Phys. Lett. 468 (2009) 205.
[214] R. Czerwieniec, A. Kapturkiewicz, J. Nowacki, Inorg. Chem. Commun. 8 (2005) 1101.
[215] A.F. Rausch, U. Monkowius, M. Zabel, H. Yersin, Inorg. Chem. 49 (2010) 7818.
[216] K.P. Balashev, M.V. Puzyk, V.S. Kotlyar, M.V. Kulikova, Coord. Chem. Rev. 159 (1997) 109.
[217] T. Hofbeck, Diplomarbeit, Universität Regensburg (2007).
[218] T. Hofbeck, M.E. Thompson, H. Yersin, unpublished results.
[219] M.M. Mdleleni, J.S. Bridgewater, R.J. Watts, P.C. Ford, Inorg. Chem. 34 (1995) 2334.
[220] D. Donges, Ph.D. Thesis, Universität Regensburg (1997).
[221] B. Ma, P.I. Djurovich, M.E. Thompson, Coord. Chem. Rev. 249 (2005) 1501.
[222] Z. Wang, E. Turner, V. Mahoney, S. Madakuni, T. Groy, J. Li, Inorg. Chem. 49 (2010) 11276.
[223] A.F. Rausch, Ph.D. Thesis, Universität Regensburg (2011).
[224] M. Maestri, D. Sandrini, V. Balzani, L. Chassot, P. Jolliet, A. von Zelewsky, Chem. Phys. Lett. 122 (1985) 375.
[225] T. Hofbeck, P. Stößel, H. Yersin, unpublished results.
[226] C. Kratzer, Ph.D. Thesis, Universität Regensburg (2004).
[227] M.V. Kulikova, K.P. Balashev, H. Yersin, Russ. J. Gen. Chem. 73 (2003) 1839.
[228] H. Wiedenhofer, Ph.D. Thesis, Universität Regensburg (1994).
[229] L. Chassot, Ph.D. Thesis, University of Fribourg (1996).
[230] S. Lamansky, P.I. Djurovich, D. Murphy, F. Abdel-Razzaq, H.-E. Lee, C. Adachi, P.E. Burrows, S.R. Forrest, M.E. Thompson, J. Am. Chem. Soc. 123 (2001) 4304.
[231] A.P. Marchetti, J.C. Deaton, R.H. Young, J. Phys. Chem. A 110 (2006) 9828.
[232] L. Chassot, E. Müller, A. von Zelewsky, Inorg. Chem. 23 (1984) 4249.
[233] A.F. Rausch, M.E. Thompson, H. Yersin, Inorg. Chem. 48 (2009) 1928.
[234] C. Adachi, R.C. Kwong, P.I. Djurovich, V. Adamovich, M.A. Baldo, M.E. Thompson, S.R. Forrest, Appl. Phys. Lett. 79 (2001) 2082.
[235] T. Fischer, R. Bauer, R. Fortte, J. Schwaiger, J. Kroeber, M. Holbach, H. Vestweber, H. Yersin; unpublished results.
[236] J.C. Deaton, R.H. Young, J.R. Lenhard, M. Rajeswaran, S. Huo, Inorg. Chem. 49 (2010) 9151.
[237] A. Tsuboyama, H. Iwawaki, M. Furugori, T. Mukaide, J. Kamatani, S. Igawa, T. Moriyama, S. Miura, T. Takiguchi, S. Okada, M. Hoshino, K. Ueno, J. Am. Chem. Soc. 125 (2003) 12971.
[238] H. Ishida, S. Tobita, Y. Hasagawa, R. Katoh, K. Nozaki, Coord. Chem. Rev. 254 (2010) 2449.
[239] D.T.V. Pentlehner, I. Grau, H. Yersin, Chem. Phys. Lett. 455 (2008) 72.
[240] D. Bruce, M.M. Richter, K.J. Brewer, Anal. Chem. 74 (2002) 3157.
[241] Y.-J. Su, H.-L. Huang, C.-L. Li, C.-H. Chien, Y.-T. Tao, P.-T. Chou, S. Datta, R.-S. Liu, Adv. Mater. 15 (2003) 884.
[242] T. Fischer, H. Yersin, unpublished results.
[243] Q. Zhao, C.-Y. Jiang, M. Shi, F.-Y. Li, T. Yi, Y. Cao, C.-H. Huang, Organometallics 25 (2006) 3631.
[244] A.C. Albrecht, J. Chem. Phys. 38 (1963) 354.
[245] G. Fischer, Vibronic Coupling, Academic Press, London, 1963.
[246] E. Gallhuber, G. Hensler, H. Yersin, J. Am. Chem. Soc. 109 (1987) 4818.
[247] H. Yersin, D. Braun, E. Gallhuber, G. Hensler, Ber. Bunsenges. Phys. Chem. 91 (1987) 1228.
[248] D.C. Baker, G.A. Crosby, Chem. Phys. 4 (1974) 428.
[249] G. He, M. Pfeiffer, K. Leo, M. Hofmann, J. Birnstock, R. Pudzich, J. Salbeck, Appl. Phys. Lett. 85 (2004) 3911.
[250] Y. Divayana, X.W. Sun, Org. Electron 11 (2010) 67.
[251] G. Schwartz, M. Pfeiffer, S. Reineke, K. Walzer, K. Leo, Adv. Mater. 19 (2007) 3672.
[252] J.C. Deaton, S.C. Switalski, D.Y. Kondakov, R.H. Young, T.D. Pawlik, D.J. Giesen, S.B. Harkins, A.J.M. Miller, S.F. Mickenberg, J.C. Peters, J. Am. Chem. Soc. 132 (2010) 9499.
[253] P.A. Breddels, P.A.M. Berdowski, G. Blasse, D.R. McMillin, J. Chem. Soc., Faraday Trans. 2 (78) (1982) 595.
[254] C.E.A. Palmer, D.R. McMillin, Inorg. Chem. 26 (1987) 3837.
[255] D. Felder, J.-F. Nierengarten, F. Barigelletti, B. Ventura, N. Amaroli, J. Am. Chem. Soc. 123 (2001) 6291.
[256] R. Czerwieniec, J. Yu, H. Yersin, in preparation.
[257] H. Yersin, U. Monkowius, R. Czerwieniec, J. Yu, WO 2010/031485 A1.
[258] I.I. Vorontsov, T. Graber, A.Y. Kovalevsky, I.V. Novozhilova, M. Gembicky, Y.-S. Chen, P. Coppens, J. Am. Chem. Soc. 131 (2009) 6566.
[259] G.B. Shaw, C.D. Grant, H. Shorota, E.W. Castner Jr., G.J. Meyer, L.X. Chen, J. Am. Chem. Soc. 129 (2007) 2147.
[260] S. Sakaki, H. Mizutani, Y. Kase, Inorg. Chem. 31 (1992) 4575.
[261] C.T. Cunningham, J.J. Moore, K.L.H. Cunningham, P.E. Fanwick, D.R. McMillin, Inorg. Chem. 39 (2000) 3638.
[262] T. Smith, J. Guild, Trans. Opt. Soc. 33 (1931/32) 73.
[263] Z.A. Siddique, Y. Yamamoto, T. Ohno, K. Nozaki, Inorg. Chem. 42 (2003) 6366.
[264] N. Armaroli, G. Accorsi, F. Cardinali, A. Listorti, Top. Curr. Chem. 280 (2007) 69.
[265] A.K. Ichinaga, J.R. Kirchhoff, D.R. McMillin, C.O. Dietrich-Buchecker, P.A. Marnot, J.-P. Sauvage, Inorg. Chem. 26 (1987) 4290.
[266] D.S. Tinti, M.A. El-Sayed, J. Chem. Phys. 54 (1971) 2529.

[267] Q. Zhang, Q. Zhou, Y. Cheng, L. Wang, D. Ma, X. Jing, F. Wang, Adv. Mater. 16 (2004) 432.
[268] G. Che, Z. Su, W. Li, B. Chu, M. Li, Z. Hu, Z. Zhang, Appl. Phys. Lett. 89 (2006) 103511.
[269] Z. Su, W. Li, B. Chu, M. Xu, G. Che, D. Wang, L. Han, X. Li, D. Zhang, D. Bi, Y. Chen, J. Phys. D: Appl. Phys. 41 (2008) 85103.
[270] Q. Zhang, J. Ding, Y. Cheng, L. Wang, Z. Xie, X. Jing, F. Wang, Adv. Funct. Mater. 17 (2007) 2983.